

UC Santa Cruz

UC Santa Cruz Electronic Theses and Dissertations

Title

PbS and Ge Nanocrystals: A Pathway Towards Third Generation Photovoltaics

Permalink

<https://escholarship.org/uc/item/6737z26v>

Author

Church, Carena

Publication Date

2014

Peer reviewed|Thesis/dissertation

UNIVERSITY OF CALIFORNIA
SANTA CRUZ

**PBS AND GE NANOCRYSTALS: A PATHWAY TOWARDS
THIRD GENERATION PHOTOVOLTAICS**

A dissertation submitted in partial satisfaction of the
requirements for the degree of

DOCTOR OF PHILOSOPHY

in

PHYSICS

by

Carena Puameli Church

June 2014

The Dissertation of Carena Puameli
Church
is approved:

Professor Sue A. Carter, Chair

Professor Glenn B. Alers

Professor Gergely T. Zimanyi

Tyrus Miller
Vice Provost and Dean of Graduate Studies

Copyright © by
Carena Puameli Church
2014

Table of Contents

List of Figures	vi
List of Tables	ix
Abstract	x
Acknowledgments	xii
I First Part	1
1 Introduction and Motivation	2
1.1 Scope of this Thesis	7
2 Basic Semiconductor Physics	9
2.1 General Background	10
2.1.1 Density of States	13
2.2 Requirements for Good Photovoltaic Action	15
2.2.1 Carrier Generation	15
2.2.2 Carrier Separation	17
2.2.3 Extraction	20
2.3 The Shockley-Queissar Limit	20
3 Nanostructured Materials – Why quantum dots?	23
3.1 Quantum Confinement	24
3.2 Synthesis	28
3.3 Generation and Recombination in QDs	29
3.3.1 Generation	29
3.3.2 Recombination	32
3.4 Current State of QDSC Research	33

4	Practical Solar Cells	36
4.1	Optoelectronic Device Fabrication	36
4.1.1	Ligand Exchange	40
4.2	Solar Cell Device Characterization	41
4.2.1	Current-Voltage Analysis	42
4.2.2	Fill Factor and Power Conversion Efficiency	45
4.2.3	Incident Photon to Carrier Efficiency	46
II	Pb-Chalcogenide Quantum Dot Solar Cells	48
5	Introduction	49
6	PbS_{1-x}Se_x-TiO₂ Solar Cells	51
6.1	Introduction	51
6.2	Experimental Methods	54
6.3	Results	57
6.3.1	Monochromatic Device Performance	63
6.4	Conclusion	66
6.4.1	Acknowledgements	67
7	PbS Graded Bandgap Solar Cells	68
7.1	Introduction	68
7.2	Experimental Methods	70
7.3	Results	72
7.3.1	Two-sized Studies: Normal Gradation	73
7.3.2	Three-sized Studies: Gradation-specific Enhancements	75
7.4	Conclusion	77
III	Group IV QDSC	79
8	Introduction	80
8.1	Ge NC synthesis	84
9	Ge QD Photoconductors	87
9.1	Introduction	88
9.2	Experimental Methods	89
9.2.1	Device Fabrication	91
9.3	Results	95
9.3.1	Effect of Absorber Layer Thickness on Device Performance	97
9.3.2	Effect of Quantum Dot Size on Device Performance	101
9.3.3	Device Optimization – Back Contact Studies	101
9.4	Conclusion	103

9.4.1 Acknowledgments	104
10 Ge QD Solar Cells	105
10.1 Introduction	106
10.2 Experimental Methods	107
10.2.1 Device Fabrication	110
10.3 Results	112
10.3.1 Effect of Absorber Layer Thickness and QD Size on Device Per- formance	112
10.3.2 Intensity-dependent Current-Voltage Experiments	118
10.4 Conclusion	123
10.4.1 Acknowledgments	124
 IV Conclusion	 125
Bibliography	128

List of Figures

1.1	World energy consumption from 1971 to 2011.	3
1.2	World map of solar insolation.	5
1.3	Cost-efficiency matrix for the three PV generations.	6
2.1	Energy-distance band diagrams for three classes of solids used in solar cells.	10
2.2	Fermi-Dirac distribution and density of states.	12
2.3	Energy-band schematic for a p- and n-region before and after contact. .	18
2.4	Maximum theoretical short-circuit current densities and open-circuit voltages as a function of absorber bandgap energy for single-junction photovoltaics.	21
2.5	The famous Shockley-Queisser limit, as calculated by Shockley and Queisser in 1964	21
3.1	Size-dependence of the bandgap in a confined crystal.	26
3.2	Representation of the MEG process.	31
3.3	Current NREL champion cell efficiency chart (2014)	35
4.1	Photo of device being hand dipped in air.	38
4.2	Left: Top-down flat schematic of device showing ITO pattern (light blue), Ge NP layer (brown), and Ag back contact pattern for 1”x1” substrates, with 6 devices on each substrate. The area of each device formed is 0.03 cm ² . Right: Side view of device stack.	39
4.3	Schematic showing what happens during ligand exchange. Initially, particles are capped with long, insulating ligands. After exchanging them with shorter ligands, the potential barrier between dots decreases, increasing the conductivity of the NC film. The black arrow represents the barrier height, while the red arrow represents the barrier width.	41
4.4	NREL calibrated solar spectrums AM0, AM1.5D and AM1.5G.	42
4.5	Figures of merit from the current-voltage curves of a photovoltaic device	44
4.6	Equivalent circuit for a photovoltaic device	45

6.1	TEM image of ternary $\text{PbS}_x\text{Se}_{1-x}$ QDs; AFM image of QD film; and absorption characteristics of QD ink before and after ligand exchange and film formation	56
6.2	(Color online.) EDX data for a film of $\text{PbS}_x\text{Se}_{1-x}$ ternary QD on quartz glass.	58
6.3	Device structure used in $\text{PbS}_x\text{Se}_{1-x}$ ternary QD solar work can be seen in a cartoon schematic and cross sectional HRSEM image.	60
6.4	(Color online.) JV curve as a function of absorber layer thickness for a film of $\text{PbS}_x\text{Se}_{1-x}$ ternary QD on quartz glass.	61
6.5	Device performance (JV and EQE) of $\text{PbS}_x\text{Se}_{1-x}$ QD solar cells.	62
6.6	Optical data for ITO and Titanium Dioxide (TiO_2) films showing increasing absorption in the UV.	64
6.7	EQE dependence on $\text{PbS}_x\text{Se}_{1-x}$ QD film thickness.	65
6.8	Monochromatic JV and EQE of alloyed ternary $\text{PbS}_x\text{Se}_{1-x}$ QD solar cells.	65
7.1	bandgap gradations used in grading studies.	71
7.2	Cartoon schematic of device structure used in PbS graded bandgap studies.	72
7.3	Size dependence studies	73
7.4	JV curves for 2-and 3-gap grading experiments.	74
7.5	Three-sized gradation JV characteristic curves and EQE spectra	76
8.1	Experimentally determined CB edge shifts along with theoretical predicted HOMO-LUMO levels for Ge NCs, a function of decreasing radii.	82
8.2	Energy-band diagram of bulk Ge.	83
8.3	A sample of the Ge QD ink used in these studies. Left: stable dispersion. Right: Precipitated QDs.	86
9.1	TEM image of 4.3 ± 1.0 nm Ge QDs, HRSEM cross sectional image of Ge QD device stack, and band diagrams of the heterojunction device studied in this paper	90
9.2	TEM images of the two larger QDs used in this study: 6.3 ± 1.0 nm and 8.9 ± 1.7 nm	91
9.3	FTIR spectra of Ge NPs before and after hydrazine exchange.	92
9.4	AFM images showing TiO_2 sol-gel and NP film topology, along with topology of the Ge QD layer.	94
9.5	UV-Vis spectra of colloidal Ge CQDs capped with oleylamine and dispersed in hexane. Inset: UV-Vis of QD films made after hydrazine exchange.	95
9.6	Absorbance spectra of films fabricated with hydrazine and pyridine exchange; inset shows photographs of each respective film.	96
9.7	(a) JV curves versus absorber layer thickness.(b) Average biased photocurrents compared to percentage of total solar photon absorption.	99
9.8	UV-Vis spectra of constituent layers in our devices.	100

9.9	JV characteristics as a function of QD size. Inset: JV characteristics as a function of back contact.	102
9.10	JV characteristics of devices made with sequential hydrazine/EDT treatments.	103
10.1	PXRD of 3 sizes of Ge QDs synthesized for this experiment show cubic-Ge, while FTIR confirms presence of OAm on the surface of the QD. . .	109
10.2	TEM image of 7.6 ± 1.3 nm Ge QDs, HRSEM image of the device stack, and UV-Vis of the Ge QD ink solution and film.	111
10.3	A comparison of photoconducting devices studied in Chapter 9, which needed to be quite thick for good absorption, to the current, much thinner, more transparent devices.	113
10.4	JV response for the (a) absorber layer thickness and (b) QD size studies. (c) EQE spectra serve as confirmation of photo generative properties of Ge QD layer.	116
10.5	Log and linear JV characteristics of identical devices fabricated on FTO and ITO show no difference in performance.	117
10.6	Transmission spectra for each constituent layer in our Ge QDSC device stack.	118
10.7	Intensity-dependent JV characteristics for 7.6 ± 1.3 nm and 3.6 ± 0.3 nm QDs	120
10.8	PV performance metrics versus incident illumination intensity for 3.6 ± 0.6 nm and 7.6 ± 1.3 nm QDs.	121
10.9	Short-Circuit Current (J_{sc}) vs intensity model fitting.	122
10.10	Shunt conductance.	123

List of Tables

4.1	Transparent Conducting Oxide materials parameters provided by TFD Inc.	37
4.2	Chemical structures of ligands used in PbS and Ge device fabrication. . .	39
7.1	First excitonic peaks and resultant bandgaps of PbS QDs used in graduation experiments.	70
8.1	Abundance of elements relevant to solar cell manufacturing, by percent weight found in Earth's crust.	81
8.2	Diatomic Bond Energies for Ge- x compounds.	85
10.1	Ge-TiO ₂ QDSCs device response as a function of absorber layer thickness. Sample devices are the best of 6 on a chip, fabricated on the same day and illustrative of general trends seen across many devices.	114
10.2	Ge-TiO ₂ QDSCs device response as a function of QD size. Values are averages of 6 devices on the chip, fabricated on the same day and illustrative of general trends seen across many devices.	117
10.3	Photovoltaic device parameters of 7.6 ± 1.3 nm QDs as a function of incident light intensity. The series (Series Resistance (R_s)) and shunt (Shunt Resistance (R_{sh})) resistances were calculated using dV/dJ at $V =$ Open-Circuit Voltage (V_{oc}) and $V = -J_{sc}$ for each of the JV curves. . .	119

Abstract

PbS and Ge Nanocrystals: A Pathway Towards Third Generation Photovoltaics

by

Carena Puameli Church

Third-generation photovoltaics offer a way around the strict thermodynamic Shockley-Queisser limit of 33% for the efficiency of a single-junction solar cell by utilizing new physics to overcome the SQ limit while also remaining relatively cheap. This thesis deals with two pathways towards III-generation PV candidates: Pb-chalcogenide and Group IV quantum dots (QDs). QDs are attractive solar materials due to their low cost, solution processability, upscaleability, and tunable optical and electronic properties due to the quantum confinement effect. This tunability leads to bandgap engineering, enabling optimal bandgaps both for increased currents due to larger IR response and multiple exciton generation (MEG), the latter being particularly exciting as it could potentially surpass the SQ limit by creating multiple charge carriers from one incoming photon, enabling efficient collection of hot electrons whose excess energy would otherwise be wasted.

Pb-chalcogenides (PbX, where X= S, Se, Te) are good candidate QD systems to study, given their large exciton Bohr radii. Additionally, their robust syntheses offer fine control over size, and hence electric properties. In this work, we approach performance increases in two ways. First, we explore an alloyed $\text{PbS}_x\text{Se}_{1-x}$ system to examine how the inclusion of small amount of Se ($x=0.9$) can lead to devices with simultaneously high

photocurrents and voltages, leading to PCEs of 4.5% . Additionally, this alloyed ternary system exhibits EQE > 100 %, indicating MEG-like behavior and efficient photocurrent generation. Secondly, we use the PbS system and bandgap gradation techniques from traditional PV to increase the limited photovoltages found in QDSC. This route also serves to show the ease with which potential tandems or multijunction QDSC could be made.

Group IV materials are the traditional PV materials, with a large body of research behind them. They are also less toxic than both II-VI and IV-VI systems, increasing the interest in them as viable QDSC systems. However, the synthetic routes are much more complicated, thus systematic studies are largely nonexistent. Here, we use Ge QDs prepared via a facile, up scalable microwave synthesis that offers relatively good size control and crystallinity. These Ge QDs have been incorporated into both photoconductors and photovoltaic devices, while parameter space has been explored to optimize performance. We present the first all-nanocrystalline Ge solar cell, utilizing a donor/acceptor heterojunction structure with TiO₂ as the window layer. After a simple ligand exchange, our Ge QDSCs are photoconductive and require no further anneals or surface treatments, potentially lowering future manufacturing costs. For our best TiO₂-Ge QD heterojunction devices, short circuit currents of 450 μ A and open circuit voltages of 0.335 V are achieved. Our low currents, compared to PbX chalcogenide QD systems, are explained via analysis of intensity-dependent current-voltage characteristics.

Acknowledgments

I would like to extend my deepest gratitude to everyone who has shared their lives with me during my time at Santa Cruz. Nicole, Chris, Eddie, Omar, Jerome, my whole cohort, you made this crazy journey a very gratifying one. Thank you to past and present members of the Carter lab for teaching me all I know about devices, sharing your knowledge, ideas, and friendship with me, specifically: Alison, Guangmei, Chris, Ben, Shin Woei, and Derek. Thanks to my collaborators at UC Davis, Raja and Susan, for enabling our Ge studies. Thanks to my committee, Gergely and Glenn, for help and support, and especially, thank you to Sue for giving me the opportunity to study what I wanted to, to learn and grow, all the while providing me guidance and assistance along the way. Thank you Charles Shaw and Brian Dunn for writing assistance. Mom, Dad, Keani, and Kylee, thank you for your limitless love and support – and for catching my addition errors. TJ a legjobb; let's always enjoy endless kaymak and exploration.

Part I

First Part

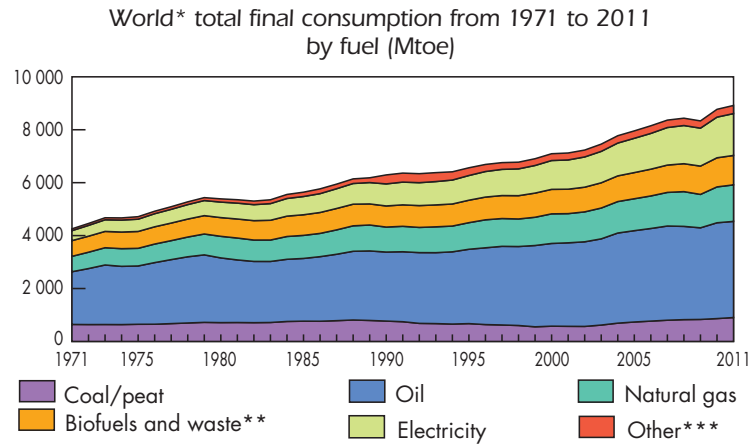
Chapter 1

Introduction and Motivation

In September 2013, the Intergovernmental Panel on Climate Change's Fifth Assessment Report (IPCC AR5-WG1) was released, wherein they conclude that it is "*extremely likely* that human influence has been the dominant cause of global warming since the mid-20th century." [1] This unprecedented disruption of Earth's natural state is a result of centuries of humanity's never-ending desire for bigger, faster, better, which, while increasing the standard of living, has to be fueled by something. That something has historically been dirty, finite coal, oil, and natural gas. While few are willing to leave behind the comforts of modern life, it is clear a disruption in the current energy landscape must happen before it is too late.

Current annual global energy use is close to 16 TW/year, of which 80% is still provided by fossil fuels, coal, and other non-renewable sources [2]. Figure 1.1 (top) shows the increasing energy consumption by source from 1971-2011, while (bottom) shows the increase in renewable energy use from approximately 1% in 1974 to close to

3% in 2013 [3].



1973 and 2011 fuel shares of total final consumption

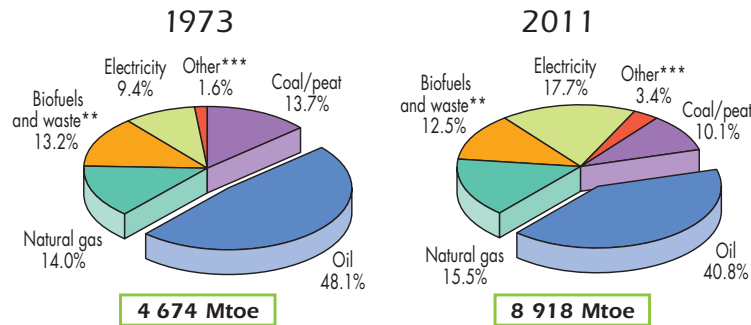


Figure 1.1: (top) World energy consumption from 1973 to 2011 show the increasingly exponential worldwide energy usage. (bottom) 1974 and 2011 data by fuel source represented, showing a 1% increase in renewables in over 40 years. * World includes international aviation and marine bunkers. ** Data before 1994 for renewables is estimated. *** Other includes geothermal, solar, wind, heat, etc.. Adapted from [3]

Though increased focus has been on renewables, they still contribute only 2% of the current market, well under 1 TW of energy [3]. Feasible hydropower could yield upwards of 2 TW/year, though it currently only provides about 1 TW/year. Wind sources are expected to eventually contribute 2-4 TW, while energy from biomass

cultivation would require over 15% of the total land on Earth for cultivation of suitable crops. Obviously, using all of Earth's farmland for energy production is not viable, and even then, biomass would only be able to produce 3 TW. This brings the total possible energy contribution of fossil and coal alternatives to under half of what is currently used.

The motivation to study solar is clear with one statement: over 120,000 TW/year in sunlight hits the surface of the Earth. This means that at current champion cell efficiencies, an area the size of Nevada can power the entire planet¹. Insolation across parts of the southwestern US are comparable to the highest regions around the planet, as seen in Figure 1.2, meaning that the US could utilize unused, relatively sparsely populated land as solar farms and produce more than enough energy to become net zero.

This potential for seemingly infinite energy has been realized since the early 1940s, when the first photovoltaic (PV) cells were fabricated. This PV prototype had a *Power Conversion Efficiency (PCE)*, of less than 1%, but efficiencies quickly rose to close to 6 % when the first Silicon (Si) pn-junction photovoltaic was fabricated. In 1961, William Shockley and Hans Queisser completed a thermodynamical study of the maximum theoretical efficiency of a solar cell, or the PCE, now known as the *Shockley-Queisser limit (SQ limit)* [4]. Their result: a single-junction solar cell under 1 sun equivalent can do no better than 33%. In the 1970s, spurred on by oil embargoes, growing political discord involving oil-producing nations, and the recognition of finite fossil fuel sources, photovoltaic research pushed cells to close to 20% PCE. Since then,

¹We don't need Nevada, do we?

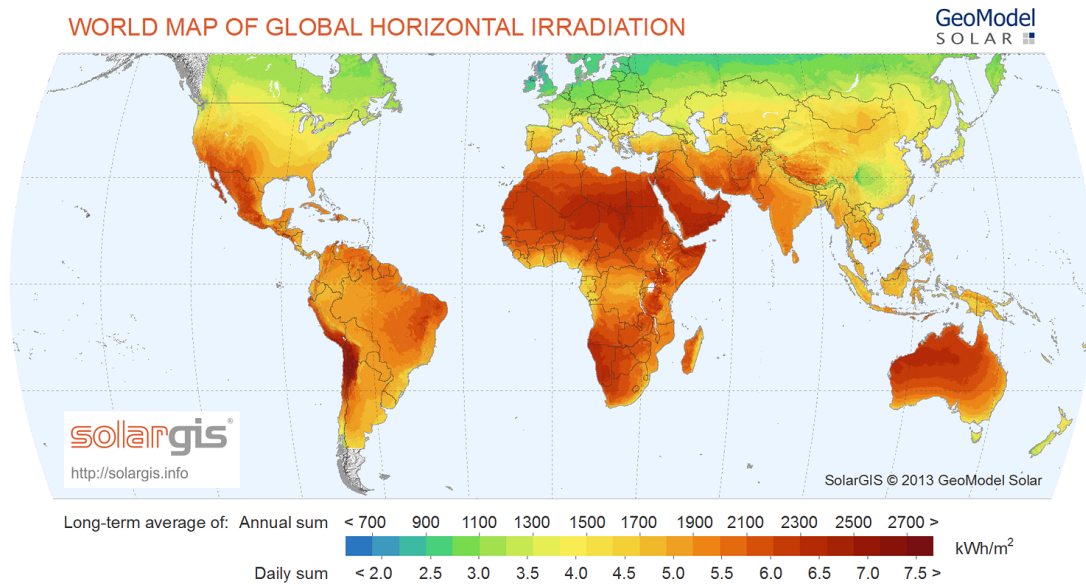


Figure 1.2: Map of the total global insolation, averaged annually, showing regions of the US are capable of competing with typical high insolation equatorial areas. Figure adapted from SolarGIS 2014 GeoModel Solar

improvements in technology have brought solar ever closer to the SQ limit: current champion monocrystalline-Silicon (mc-Si) cells have achieved 25% PCE, Gallium Arsenide (GaAs) world-records are nearing 30%, and concentrated solar cells have cleared 48% at a 418 sun equivalent.

These two approaches for solar energy conversion are known as the *first- and second-generation photovoltaics*. Photovoltaic technologies can be organized into generations by their cost, constituent materials, and theoretical efficiencies, as seen in Figure 1.3. First-generation PV made up of mc-Si dominates the current consumer PV market with module efficiencies close to 25%. Second-generation PV such as Cadmium telluride (CdTe), Copper indium gallium selenide (CIGS), amorphous-Si and other thin-film technologies aim to cut the cost of first generation PV by using less materials. While

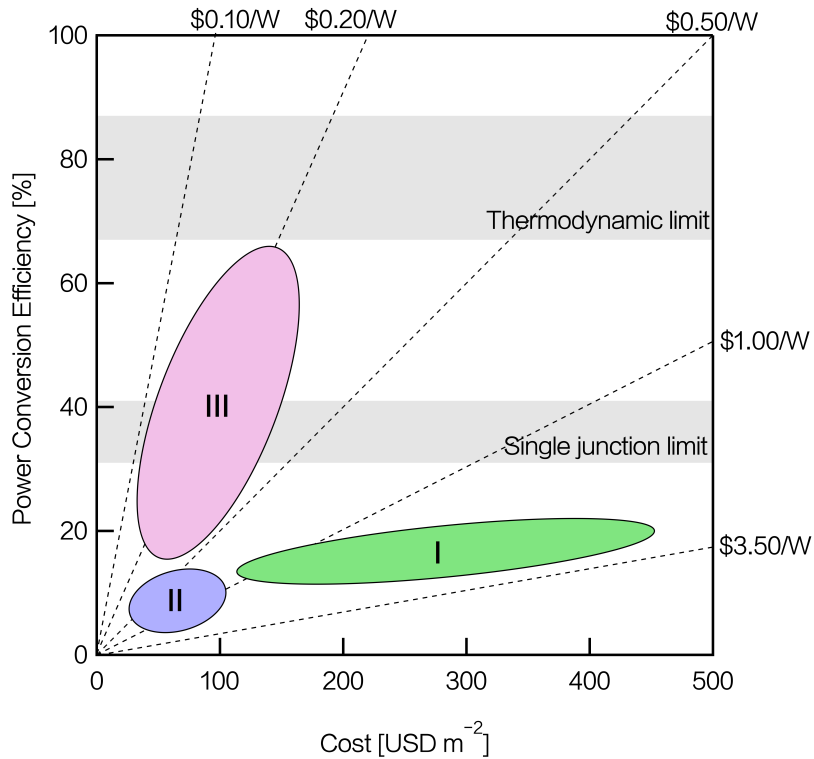


Figure 1.3: Cost-efficiency matrix for the three PV generations. Third-generation PV is defined as those technologies able to surpass the SQ limit while also being cheaply made.

important steps along the path to feasible solar energy conversion, both first and second-generation technologies are undesirable. Inching closer to the single-junction limit of 33% still requires expensive semiconductor processing techniques for low-defect, highly crystalline materials, while current concentrator technology is too costly for widespread adoption.

There are then two main strategies for current photovoltaics research: either reduce the total cost down to under \$0.20/W or take advantage of new physics that can overcome the SQ limit. Photovoltaics who belong to this genre of technologies are

known as *third-generation photovoltaics* and include potential game changers such as hot carrier solar cells, intermediate band, organics, hybrids, and nanostructured solar cells.

1.1 Scope of this Thesis

This dissertation is focused on exploring nanostructured materials to achieve higher performing third-generation photovoltaics. In order to do this, a fundamental understanding of the optical and electronic properties of these nanomaterials used is necessary. To that goal, the remainder of Part I begins with a brief overview of semiconductors and photovoltaic operating principles, then moves into a discussion of the benefits of nanostructured materials, and how bulk semiconductor properties change upon quantum confinement. Part I concludes with a brief discussion on typical fabrication and characterization techniques used in the course of this research.

Part II focuses on the first materials route explored towards higher performing nanostructured PV: lead chalcogenide nanocrystals. Chapter 6 is presented as a modified manuscript that was published on the fabrication and characterization of ternary alloyed Lead Sulfide-Selenide ($\text{PbS}_{1-x}\text{Se}_x$) TiO_2 solar cells. Interestingly, this alloyed system can retain the positive benefits of each constituent binary system. Chapter 7 involves unpublished work on bandgap engineering with the goal of increasing V_{oc} . This fabrication method can be applied to multi-junction solar cells, and lays the groundwork for colloidal QD devices of that type.

Part III focuses on the second materials route used to explore third generation photovoltaics: Group IV semiconductors. These archetypal semiconductor materials have only very recently been synthesized in their nanocrystalline form, so the Group IV nanocrystal field is very new. Chapter 8 motivates the use of these materials. Chapter 9 is presented as a modified manuscript that was published on the fabrication and characterization of photoconductors made from nanocrystalline Germanium (Ge). Chapter 10 is presented as a modified manuscript from a submitted publication involving the first all-nanocrystalline TiO₂-Ge solar cells.

Chapter 2

Basic Semiconductor Physics

Photovoltaics (in most cases)¹ operate on a very simple principle: one photon in, one electron out. Energetic light above a certain threshold² is capable of exciting electrons out of the material, leading to conduction. This phenomena was discovered in 1905 and is known as the Photoelectric Effect, the theory for which Albert Einstein eventually received the Nobel Prize. Both the photoelectric and the photovoltaic effects are quantum mechanical process, with the main difference being that in an operating photovoltaic device these generated carriers are separated by an external force and extracted to an outside circuit where they are able to perform work. This separating force is typically provided by spatial variations in the electronic environment of the materials. In the following sections, a brief introduction to semiconductors as well as the operating mechanisms of solar cells will be described.

¹This does not have to be the case, and indeed, for "energetic enough" photons, more than one exciton can be generated. This process is called Carrier Multiplication and is one of the main routes explored for overcoming the SQ limit. This will be discussed in detail later.

²This threshold is the work function for metals and the bandgap for semiconductors.

2.1 General Background

It is helpful to start the discussion with an overview of the concepts used in solar energy conversion. In a single atom, electrons occupy specific orbital states due to their bonding. If two atoms are in close enough proximity to each other, their orbitals must split due to the Pauli exclusion principle. For solids with crystal lattices, there are N such atoms in close proximity, giving N split levels in close proximity; these levels become a continuum known as a *band*. It is this band structure at absolute zero that determines what type of material a solid is.

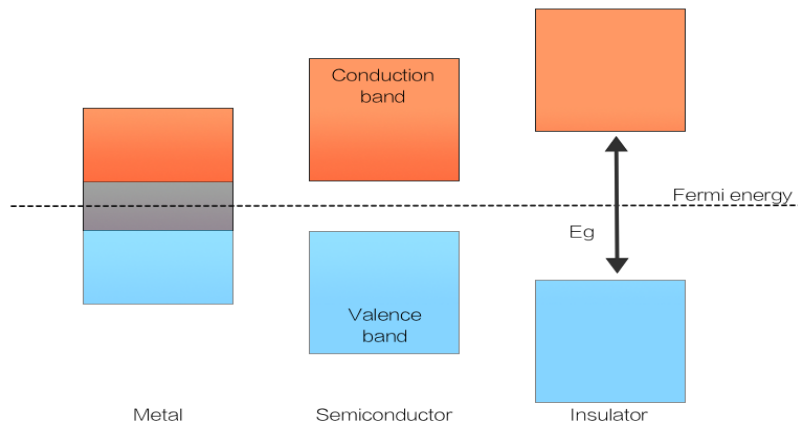


Figure 2.1: Energy-distance band diagrams for metals, semiconductors, and insulators, showing the overlap in bands leading to conduction for metals. Small bandgaps allow semiconductor conduction via thermal or photo generation, while the larger bandgaps found in insulators typically make even photo generation impossible but for the most energetic solar photons.

Figure 2.1 shows the band structure for metals, semiconductors and insulators at absolute zero and their respective *Fermi energies*. The Fermi energy represents the

level at which 50% of the energy states are filled at absolute zero; a more useful quantity for operating devices is the *Fermi level*, which is the *chemical potential* μ of the electrons, represents how difficult it is to add an electron to the closed system, and is valid for all temperatures. The location of the Fermi level determines what majority type a semiconductor will be. At absolute zero, all electrons in a semiconductor are in bonding states (no free electrons), so the *Valence Band (VB)*, or the highest occupied state, is full while the *Conduction Band (CB)*, or the lowest unoccupied state, is empty. Both full and empty states cannot sustain any current, so the materials are not conductive. If an electron gets excited out of the filled VB into the CB, it leaves behind a space which is quickly filled by its neighboring electron; this space is called a *hole* and it is helpful to think about holes as the free carriers in the VB.

For metals, the conduction and valence bands overlap, so there are always free electrons available and current flows easily. For semiconductors and insulators, there is a forbidden range of energies for which no states can exist; this is known as the *bandgap* of the material and is primarily determined by the bonding structure of the material. Alternatively, the bandgap, E_g , can be thought of as the ionization energy for charged carriers, or the energy required to free a carrier from the lattice so that it may participate in conduction.

There is not much difference between semiconductors and insulators at absolute zero, however at finite temperatures T the bandgap of a semiconductor is small enough such that thermal excitations below the material's melting point allow electrons to be promoted from the VB to the CB. Typical bandgaps for semiconductors range from

approximately 0.3 eV through 3 eV and have a large impact on both the optical and electronic properties of the material.

At a finite temperature T , the carrier occupation will follow the Fermi-Dirac distribution function, which is given in Equation 2.1 and shown in Figure 2.2:

$$f(e) = \frac{1}{e^{(E-E_F)/k_B T} + 1} \quad (2.1)$$

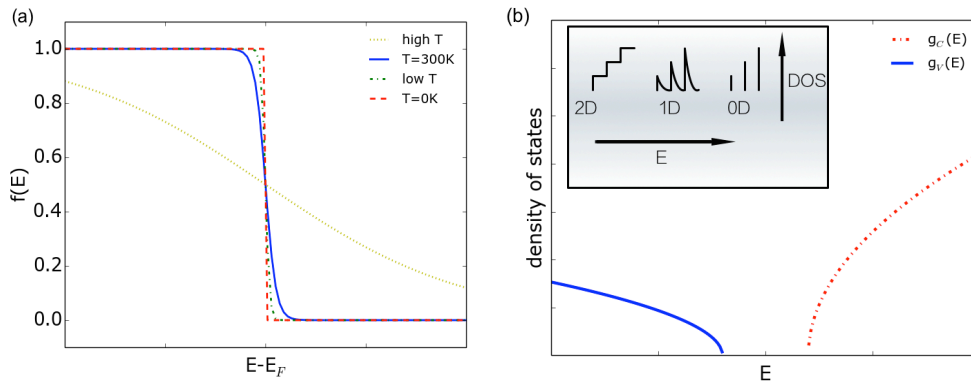


Figure 2.2: (a) The Fermi-Dirac distribution as a function of T . Several values of $f(E)$ are shown, including $T=0$, low temperature, room temperature, and high T . As the temperature increases, it becomes more probable to find an electron in the conduction band. (b) DOS for a 3D sphere. Inset: Shapes of the DOS for confined structures.

At absolute zero, all of the electrons are in the valence band. As the temperature increases, the probability of an electron being in the conduction band increases. At room temperature, the bandgaps are usually too large for much thermalization to occur, but with increasing temperature this happens more and more. The actual occupation is given by $(f(e) \cdot g(E))$ where $g(E)$ is the *density of states (DOS)* of the material.

2.1.1 Density of States

It is helpful now to derive³ the density of states, which is a measure of how many states are available to the electron (hole) per unit volume in \vec{k} -space.

From the Pauli exclusion principle, each state can contain two electrons of opposite spin. Because \mathbf{k} is a "good" quantum number, each state can be described by a unique \mathbf{k} value, and there are two allowed electrons per \mathbf{k} . Consider a crystal in 3D: it has volume $L \times L \times L$ and can be described by k_x, k_y , and k_z . The solution to the Schrodinger equation for a well of width L is

$$k_x = \frac{\pi}{L}n_x, k_y = \frac{\pi}{L}n_y, \text{ and } k_z = \frac{\pi}{L}n_z \quad (2.2)$$

where n_x, n_y , and n_z are integers. Now, we need to know how many states are available per unit volume of k-space which is $(\frac{\pi}{L})^3$ states from Equation 2.2. The total number of states should be $(\frac{\pi}{L})^3 \frac{1}{V}$. At temperature T, the typical volume containing all states is much larger than L^3 , so considering positive $k_{x,y,z}$, we calculate the volume of a sphere with radius k.

$$\# \text{ of states, } N = 2 \times \frac{1}{8} \times \frac{4}{3}\pi k^3 \times \left(\frac{L}{\pi}\right)^3 = \frac{1}{3} \frac{L^3}{\pi^2} k^3 \quad (2.3)$$

We can fill this volume with a number of states equal to two (considering spin) times one eighth (octant of positive k values) times the volume of a sphere divided by the volume of our unit cell (one state). It's useful to express this in terms of energy instead of momentum. If the band minima/maxima are not wildly varying and located

³this derivation follows Nelson [5]

at $\mathbf{k}=\mathbf{k}_{0c,0v}$, we can use the *parabolic band approximation*:

$$E(\mathbf{k}) = E_{c0} + \frac{\hbar^2 |\mathbf{k} - \mathbf{k}_{0c}|^2}{2m_c^*} \quad \text{for electrons} \quad (2.4)$$

$$E(\mathbf{k}) = E_{v0} - \frac{\hbar^2 |\mathbf{k} - \mathbf{k}_{0v}|^2}{2m_v^*} \quad \text{for holes} \quad (2.5)$$

where $m_{c,v}^*$ is the *effective mass*, a measure of how strongly the atomic potentials affect the electrons (holes), and is defined from the band structure by the following:

$$\frac{1}{m_{c,v}^*} = \frac{1}{\hbar} \frac{\partial^2 E_{c,v}(k)}{\partial k^2} \quad (2.6)$$

It follows that for an electron (hole) in the CB (VB),

$$\frac{dk}{dE} = \frac{1}{2} \left(\frac{2m_c^* E}{\hbar^2} \right)^{3/2}. \quad (2.7)$$

Then, the number of states in the energy interval $(E + dE)$ is given by,

$$\frac{dN}{dE} = \frac{dN}{dk} \frac{dk}{dE} = \sqrt{2} \frac{L^3}{\pi^2} \frac{m_c^{*3/2}}{\hbar^2} \sqrt{E - E_{c0}} \quad (2.8)$$

Finally, the density of states is

$$g(E_c) = \frac{dN}{dE} \frac{1}{L^3} = \frac{\sqrt{2} m_c^{*3/2}}{\pi^2 \hbar^2} \sqrt{E - E_{c0}}, \quad E > E_{c0} \quad (2.9)$$

$$g(E_v) = \frac{dN}{dE} \frac{1}{L^3} = \frac{\sqrt{2} m_v^{*3/2}}{\pi^2 \hbar^2} \sqrt{E_{v0} - E}, \quad E_{v0} > E \quad (2.10)$$

The DOS calculated from Eqs. 2.9-2.10 can be seen in Figure 2.2b, where the shape of the parabolas is determined by m_c^* and m_v^* .

As seen above, the DOS is a dimensional-specific quantity. The DOS for lower dimension materials such as quantum wells, nanowires, or quantum dots can be found

in a similar manner to the 3D derivation. Since this thesis deals with materials confined in 3D, it is helpful to discuss the 0D (QD) DOS. From Sze we have [6],

$$g(E_{QD}) = 2\delta(E - E_0) \quad (2.11)$$

This tells us that the DOS of a 3D confined material is also affected by confinement, leading to a collection of discretized, atom-like orbital states where E_0 corresponds to the energy state for each orbital. The 0D DOS is seen in the inset of Figure 2.2b, along with the DOS for 2- and 1D materials.

2.2 Requirements for Good Photovoltaic Action

This work involves improving current photovoltaics through a variety of engineering techniques and materials pathways, specifically using nanomaterials. However, for any good photovoltaic device, there are three main requirements which will be discussed in the following sections:

1. Generation
2. Separation
3. Extraction

2.2.1 Carrier Generation

Most semiconductors have bandgaps which enable electrons to be ionized by visible light. So the first requisite for a good solar cell, carrier generation, is easily

achieved through photon absorption. Photons with energies $\geq E_g$ are capable of exciting an electron out of the filled valence band into the mostly empty conduction band, leaving a hole in its place. Generation depends on the intensity of the incoming photon flux as well as the absorption coefficient and DOS for the material. The absorption coefficient of a material depends strongly on the behavior of the bands near the extrema. If the minima of the CB and maxima of the VB lie at $\vec{k} = 0$, the crystal is considered a *direct bandgap* semiconductor. If the extrema are separated by $\vec{k} = \vec{k}'$, the material is called *indirect*. In the parabolic band approximation, absorption coefficients are expressed as Equations 2.1 (for direct bandgaps) and 2.2 (for indirect bandgaps), where it's easy to see how their behaviors are quite different:

$$\alpha(E) = \alpha_0(E - E_g)^{1/2} \quad (2.12)$$

$$\alpha(E) \propto \alpha_0(E - E_g)^2 \quad (2.13)$$

Since \vec{k} is a good quantum number and must be conserved, it is necessary to include phonons for indirect transitions. This leads to overall lower absorption coefficients and, as a direct consequence, indirect materials do not absorb as strongly as direct materials in addition to the onset of absorption being more gradual. This also means that a thicker layer will be necessary to absorb 100% of available photons for an indirect material; for Si, the absorber must be hundreds of microns thick.

There are also other generation mechanisms⁴, though photogeneration is far and away the most important generation mechanism and largest contribution to solar

⁴Thermalisation contributions are small and increase with decreasing bandgaps.

cells.

2.2.2 Carrier Separation

For photovoltaics, this requisite separation is most often induced by a gradient in the composition of the materials. The most simple and well known example of this is the *pn junction*. Donors or acceptors are added to the crystal lattice to create a doped material that is either majority p- or n-type. For Si, these dopants are typically boron and phosphorus. The p- and n-type regions are brought in spatial proximity to form the pn junction. At thermal equilibrium, no net current flows and the Fermi level is independent of position.

Then, at any point, the current is given by:

$$J = J_n + J_p = \mu_n n \nabla E_{F_n} + \mu_p n \nabla E_{F_p} \quad (2.14)$$

which becomes

$$J_n = qD_n \nabla(n - n_0) + \mu_n(n - n_0)(qF - \nabla\chi - kT\nabla \ln N_c) \quad (2.15)$$

for electrons and

$$J_p = -qD_p \nabla(p - p_0) + \mu_p(p - p_0)(qF - \nabla\chi - \nabla E_g + kT\nabla \ln N_v) \quad (2.16)$$

for holes, where n_0 and p_0 are the carrier densities in equilibrium [5].

It's straightforward to see from Eqs. 2.15 - 2.16 that there exist two currents: the first term represents diffusion while the second term represents the drift. Simply put, at the junction, a charge carrier gradient of holes and electrons forms, causing a diffusion

current. As the carriers move back and forth forever⁵, into the opposite regions, they leave behind an area of positive (n moving to p) and negative (p moving to n) charge region. This creates a *depletion region* in which an electric potential builds up due to the electric field created by the migrating charges. In a pn junction, this diffusive current is then balanced by an opposing carrier "drifting" in the opposite direction of the diffusion. It is this depletion region that drives the diode nature of a pn junction.

Figure 2.1 shows schematically what happens when you put a p and n region together. Initially, when the two regions are separated, their Fermi levels lie close to the majority bands. At contact, the carriers diffuse and drift until equilibrium is reached. At equilibrium, there is significant band bending to accommodate the new Fermi level, and a *space charge region* is created. The *Built-In Voltage* (V_{bi}) is also represented by ϕ_B in Figure 2.1, where V_{bi} is the maximum chemical potential available in the junction.

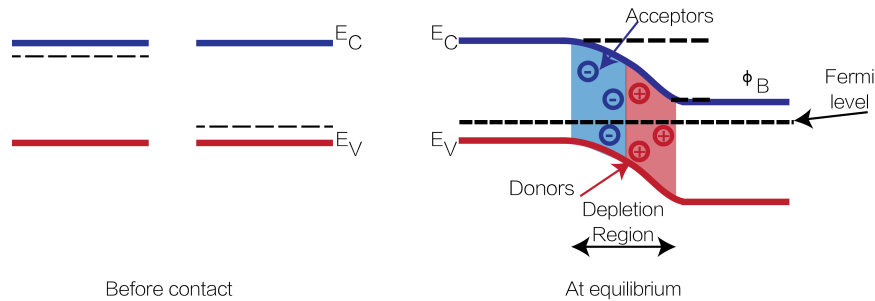


Figure 2.3: Energy-band diagram showing a p- and n-region before contact and at equilibrium. At contact, carriers drift and diffuse until they are in equilibrium. Band bending occurs to accommodate the new Fermi level.

⁵not really forever

2.2.2.1 Other Junctions

Generally, most photovoltaic cells can be classified as *heterojunctions* or *homojunctions*. A homojunction is a junction where the same intrinsic material with the same bandgap is doped into p or n layers and placed together (the pn junction from the previous section). However, all of the devices studied in this work are heterojunctions, or junctions comprised of two different materials, with different majority carriers and typically different bandgaps. Semiconductor heterojunctions are classified according to the relative alignment of the *Electron Affinity (EA)* and *Ionization Potential (IP)* of the two materials. In a *type I heterojunction*, the band edges of a semiconductor fall within the energy gap of the second one, while a *type II heterojunction* is formed when a staggered level alignment sets in. Only in this latter case is charge separation at the junction interface energetically favorable, and thus the junction may serve to convert photogenerated excitons into free charge carriers. A heterojunction will also undergo band bending at the interface, similar to what we saw in Figure 2.3.

Another useful device structure is the *Schottky diode*, which utilizes a metal-semiconductor (MS) junction instead of the typical semiconductor-semiconductor interface to drive separation. The barrier at the MS interface is determined by the fermi level of the metal⁶ and the bands of the semiconductor. There is typically a smaller driving force in Schottky devices, and the V_{oc} s are also typically lower, so they do have their drawbacks. However, these are helpful prototypical devices because they are generally simpler to make than hetero- or homojunctions.

⁶the work function, ϕ

2.2.3 Extraction

The last step for efficient photovoltaic action requires the unimpeded extraction of charge carriers. In theory this is simply achieved by finding an ohmic contact material, often times a *Transparent Conducting Oxide (TCO)* or metal whose work function matches most closely to the band levels of the electrons and holes. This can also be accomplished using *selective contacts*, or contacts whose energy bands/offsets allow only one carrier type to pass. However, in practice, any mismatch or interface in the device can cause large resistive losses and the formation of an additional diode in the cell.

2.3 The Shockley-Queissar Limit

Before discussing the benefits of NCs, a brief introduction of the famous Shockley-Queissar limit (SQ limit) is presented. Shockley and Queissar's calculation of the ideal efficiency of a single-junction solar cell is based on purely thermodynamic considerations. They make the following assumptions:

1. The sun radiates as a blackbody $\geq E_g$ of the semiconductor.
2. Only one *electron-hole pair (ehp)* generated per absorbed photon; for photons with $E \gg E_g$, the electron quickly thermalizes to the band edge.
3. There are no other losses besides purely radiative recombination (detailed balance between optical generation and radiative recombination).

Given these assumptions, it is straightforward to calculate both the ideal V_{oc} and J_{sc} as a function of bandgap.

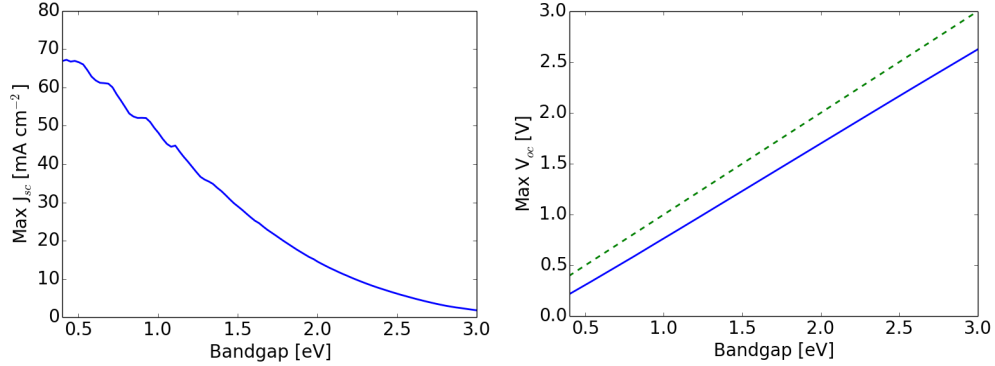


Figure 2.4: Maximum theoretical short-circuit current densities and open-circuit voltages as a function of absorber bandgap energy for single-junction photovoltaics. The dashed line in the open-circuit voltage figure represents the absolute limit, the bandgap of the material.

Finally, this gives us the SQ limit as a function of bandgap:

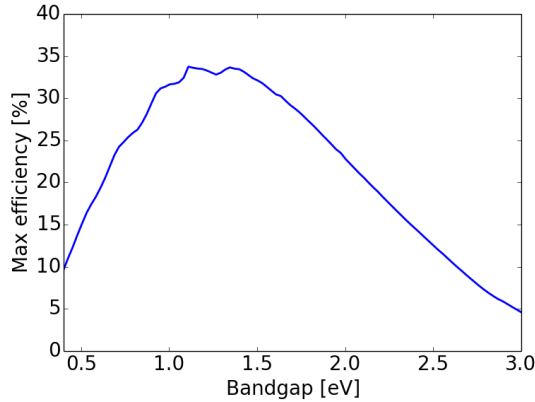


Figure 2.5: The famous Shockley-Queisser limit on the total efficiency of a single-junction solar cell.

The $\sim 33\%$ PCE comes from considering a 1.34 eV material. There are a few differences between this limit and real-life limits, mostly due to the spectrum deviating

from a perfect blackbody and non-ideal bandgaps in real world materials. For example, Si, the most ubiquitous semiconductor, has a bandgap of 1.1 eV, yielding a maximum PCE of only 29%.

The SQ calculation may also be used to analyze loss mechanisms for PV. From assumption 1 we know that all photons under the bandgap do not contribute to generation; this loss accounts for about 23% of the available solar energy. From assumption 2 we find that photons with energy greater than the bandgap do not contribute more than one electron-hole pair, and instead quickly thermalize down to the band edge; this loss accounts for $\sim 30\%$ of the sun's power [5]. It follows then that if we can harness the almost 55% of lost energy, our efficiencies will increase dramatically. Resolving the first loss mechanism is the motivation behind multi-junction photovoltaics, while QDSC and hot carrier devices attempt to reduce the second loss through third-generation principles.

Chapter 3

Nanostructured Materials – Why quantum dots?

This thesis deals with using semiconducting nanomaterials as a viable third-generation solar conversion candidate. But what makes them special and how are they different from the materials typically used today? The main difference is size – nanocrystals are typically tens of nanometers and may have between 100-10000 atoms in their lattice. This reduced size puts them on the order of the Bohr radius¹ which leads to a number of interesting and important consequences for their electronic and optical properties.

¹The Bohr exciton radius is defined as the usual Bohr radius with the nuclei replaced by the hole. Recall, the Bohr radius is defined as the average distance an electron is from the nuclei.

3.1 Quantum Confinement

When the physical size of a crystal becomes comparable with the *Bohr exciton radius*, a_B ,

$$a_B = \frac{\hbar^2 \epsilon}{q^2} \left(\frac{1}{m_e^*} + \frac{1}{m_h^*} \right) \quad (3.1)$$

for that material, the excitations are said to be quantum confined. The dimensionality of confinement leads to the type of confined crystal, in the following way:

- Quantum Dots (QD), Nanocrystals (NC), or Nanoparticles (NP)² have excitonic confinement in all three spatial dimensions.
- Quantum rods/wires are defined as materials whose excitons are confined in two spatial dimension, with free propagation allowed in the third.
- Quantum wells are defined as materials whose excitons are confined in one spatial dimension, with free propagation allowed in the remaining two.

Confinement can be quantified by the ratio between the Bohr radius, a_B , which represents the onset of confinement, and the physical radius of the particle, a_r [7]. NCs are considered to be in the *strong-confinement regime* if $a_r \ll a_B$; this leads the complete quantization of both carriers. The *intermediate regime* occurs when one of the carrier's effective mass is much larger than the other, for example if $m_e^*/m_h^* \gg 1$, leading to $a_h < a_B < a_e$. In this case, the hole experiences much more confinement than the electron. *Weak confinement* is defined as $a_r > a_B$.

²NC, NP, and QD will be used interchangeably in this thesis.

The nanocrystal walls act as a physical barrier to the carriers and may be modeled, to first approximation, as an infinite potential well. The confinement of electrons or holes in these potential wells leads to the creation of discrete energy levels in the well, compared to the continuum of states in bulk material; confinement also leads to a major change in the density of states, as we saw in Figure 2.2. The problem is analogous to the well-known "particle in a box" problem where the energy levels can be calculated in the usual way. We may start by using an electronic wave function, ψ_n , of the form

$$\psi_n = e^{i\vec{k}\cdot\vec{r}} U_k(\vec{r}) \phi_n \quad (3.2)$$

where k is the transverse electron wave vector, $U_k(r)$ is the Bloch wave function, and ϕ_n is the envelope wave function. The envelope wave function is determined by solving the Schrodinger equation:

$$\left(\frac{\hbar^2}{2m^*} \frac{\partial^2}{\partial r^2} + V_e \right) \phi_n = E_n \phi_n \quad (3.3)$$

Then, in our simple model of a quantum well with an infinite barrier, the NP energy gap $E_g(QD)$ is related to the bulk semiconductor gap $E_g(bulk)$ by the following expression:

$$E_g(QD) = E_g(bulk) + \left(\frac{\pi^2 \hbar^2}{2m_r R^2} \right) - \frac{1.8q^2}{\epsilon R} \quad (3.4)$$

where the first modification arises from the confinement of the exciton to an infinite well. The second energy shift can be attributed to the enhanced Coulombic attraction between the electron-hole bound pair.

From Equation 3.4 we find the first difference between QDs and their bulk counterparts is that the QD bandgap is increased by a factor inversely proportional

to the radius³; that is, with decreasing physical size, the bandgap is increased. This straightaway leads to the ability to tune both the optical and electronic properties of the NC.

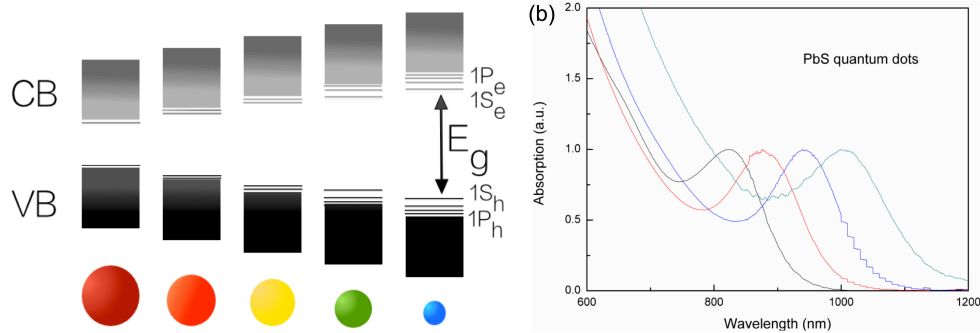


Figure 3.1: Size-dependence of the bandgap in a confined crystal is shown. (a) The colors represent visible emission of CdSe QDs ranging from 6nm (red) to 2nm (blue) showing the blueshift in emission with decreasing particle size. (b) Size-dependence of the bandgap in PbS QDs used in these experiments can also be shown by the shifting position of the first exciton peak in the absorption spectra.

This is a striking result and readily seen in the absorbance and fluorescence spectra of these colloidal NP inks, as seen in Figure 3.1. The position of the *exciton peak*, generally accepted as the energy of the first allowed electron transition and thus the bandgap, blueshifts with decreasing dot size as predicted in Equation 3.4. A schematic of the CB and VB band shift with radius decrease is also shown, to illustrate what happens to the continuum energy states when they become discretized in the strong confinement regime. Discretization accurately describes the case only for states near the band edge, though. Deep in the band the number of available states increases,

³Or for wells, the width of the well. The results are general, but from now on we will focus on QDs

tending to the continuum limit for particularly large NCs. This effect can also be seen in Figure 3.1b, as the absorption spectra exponentially increases into the UV due to the increase in available states and thus transitions.

Since this effect is so easily seen via absorption, the sizes of QDs are often given in terms of their first excitation absorption peak or bandgap instead of their physical diameter. From the Planck relation we have:

$$E = \hbar\omega = h\nu = \frac{hc}{\lambda} \quad (3.5)$$

Bandgaps are usually approximated from absorption spectra in this way, by letting $hc \sim 1240 \text{ nm}\cdot\text{eV}$.

A second consequence to quantum confinement is that \vec{k} is no longer a good quantum number:

$$\Delta k \Delta x > 1 \quad (3.6)$$

This results in a relaxation of optical selection rules, leading to a higher oscillator strengths for QDs compared to their bulk, which means we should be able to use much thinner absorbers to achieve complete absorption. This also results in slowed cooling of hot carriers, by the so-called *phonon bottleneck* and fact electronic states are discretized, which has a high impact on generation and recombination processes and will be discussed later in this chapter.

A third consequence is that instead of producing charge carriers, confined NCs produce excitons. In bulk materials, excitonic generation is not a large contribution of total generation due to the fact that the excitonic binding energy is quite small, so $k_B T$

provides enough energy to dissociate the electron and hole. However, for NCs, strong spatial confinement leads to increased Coulombic interaction and higher exciton binding energies. As a practical side note, for NCs to be usable in PV devices, we need to figure out a way to dissociate the generated excitons and collect the resulting free electrons and holes with high efficiency.

3.2 Synthesis

Generally speaking, nanostructured materials are synthesized in one of two ways: either colloiddally or via vacuum deposition techniques. The colloidal syntheses are especially exciting for third generation principles, as they are robust, simple, up scalable and relatively cheap. Currently, most colloidal syntheses are of the hot injection type, whereby metal precursors are injected into solutions containing other precursors and surfactant materials used to control the size and shapes of the resultant nanocrystals. The timing and temperature at which these injections occur affect the physical properties of the nanomaterials. For example, in a PbSe→CdSe cation exchange, if you inject at a lower temperature you get nanorods instead of quantum dots; the same effect can be achieved in other systems by supersaturating the precursor solutions. These reactions are allowed to proceed under heating until desired size and dispersion are achieved. The resultant nanomaterials are generally washed and then dispersed in solutions that are optimized for either spin casting or dip coating. Good

size control, defined as dispersity $<10\%$ ⁴, is important for the optoelectronic properties of the resultant ink and any device made from the ink.

The other synthesis route involves using vacuum deposition techniques, usually a form of Molecular Beam Epitaxy, Chemical Vapor Deposition or through the use of Plasma RF reactors. NCs synthesized in this way are more easily deposited on substrates, can be synthesized with or without ligands, and typically have higher reaction yields when compared to the colloidal syntheses. Occasionally these vacuum synthesized NCs are collected and dispersed into a NC ink, in which case it is necessary for a stabilizing ligand to be added to the surface of the NC. The main downside to this synthetic route is the use of expensive vacuum deposition technology.

3.3 Generation and Recombination in QDs

In the SQ limit, only radiative recombination and optical generation above the bandgap of the material are considered. However, for real-world nanostructured (and bulk) materials, there are multiple competing generation and recombination processes.

3.3.1 Generation

Normal photogeneration occurs in the same way for nanomaterials as it does for their bulk counterparts with one caveat. Since the bandgap is tunable for NCs, one material with an appropriate bulk bandgap can be used in its NC form to absorb the

⁴This is typically quantified from the full-width at half maximum value (fwhm) of the excitonic peak in the absorption spectra

entire visible spectrum. An example of this is Lead Sulfide (PbS), whose bulk bandgap is 0.4 eV (not useful at all for solar energy conversion), can effectively be tuned from 0.9 - 1.7 eV. Additionally, a more interesting generation mechanism can happen with higher energy photons called *Multiple Exciton Generation (MEG)*⁵.

3.3.1.1 Multiple Exciton Generation

MEG is the theory that if an incoming photon with $E \geq 2E_g$ ⁶ is absorbed by the nanostructured semiconductor, it may excite two or more excitons. A high-energy photon is absorbed, exciting an electron into the CB. Instead of transferring its excess energy E_{ex} to the lattice, E_{ex} is transferred to another exciton. It is this reason that MEG is also often thought of as a reverse (inverse) Auger process. Figure 3.2 shows a cartoon of the MEG process.

It is the nanocrystalline analogue to bulk *Impact Ionization(II)*, but occurs at a higher rate and at a lower turn-on threshold in nanomaterials due to the strong correlation between electron and hole, relaxation of conservation of momentum, and the discretization of states near the band edge. These last two effects can also suppress fast carrier cooling rates, normally a sub-ps process in bulk, so that the MEG process may be able to compete. This is known as the phonon bottleneck, where the cooling rate due to phonons is much lower than in the bulk and proportional to increases in hot carrier density [8] due to discretization of energy states.

⁵Also called *Carrier Multiplication (CM)*, though MEG is preferred since bound e^-h^+ pairs are produced in nanostructured materials.

⁶This is the limit due to conservation of energy. MEG turn-on thresholds are typically $> 2.8E_g$.

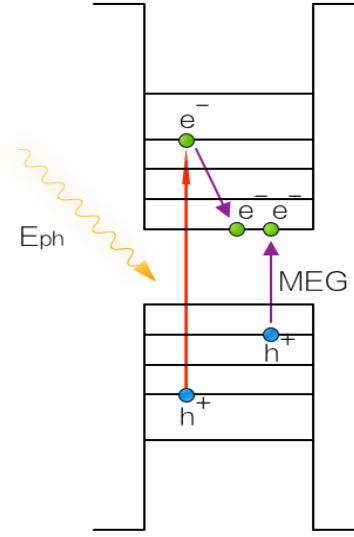


Figure 3.2: Cartoon schematic of the MEG process showing incoming photon with energy in excess of the bandgap exciting two excitons.

Impact Ionization was studied as a potential way to increase the efficiencies of mc-Si PV for quite some time, but was ultimately abandoned as it does not become a competitive channel in bulk Si until $\sim 4-5E_g$ due to efficient phonon-mediated thermalization and conservation of energy and momentum considerations. Of course, II at $5E_g$ does not increase the efficiency of a solar cell due to the low spectral intensity available at those wavelengths. Due to similar considerations, the optimal bandgap for MEG enhancement in NCs is at 0.8eV.

MEG is an especially fast process, on the order of 100 ps or less. Experimentally, it is seen in the rapid Auger-like decay of multiexcitons in transient absorption spectra. There are a few theories attempting to explain the MEG effect, but none yet are capable of a complete physical description. Efficient MEG has been reported for CQD solutions of PbTe, PbSe, PbS, CdSe, Si, and InAs [9, 10, 11]. MEG has also

been seen in films of PbSe and in an operating PbSe solar cell [12, 13, 14, 15]. It is a topic of intense research since it can potentially overcome the SQ limit, which famously only considers one generated electron-hole pair for one absorbed photon, though PCE increases have yet to be observed. In fact, the maximum efficiency for a single-junction solar cell becomes 45% when maximum MEG enhancements are considered [16].

3.3.2 Recombination

There are three main sources of recombination in solar cells, radiative recombination, Auger recombination, and Shockley-Reed-Hall recombination. *Radiative recombination* is the normal band-to-band (interband) recombination. If this is the only type of recombination, there is not much trapping or mid-gap states. In PV and other power positive applications, radiative recombination is to be minimized for optimal performance. Of course, in an ideal cell, detailed balance is the only limiting factor of radiative recombination.

Auger recombination is a non-radiative recombination process in which an electron in the CB recombines with a hole in the VB and instead of emitting a photon, the energy from the recombination event is passed to a third electron, exciting it to a "hot" carrier. After this interaction, the hot carrier usually loses its excess energy to thermal fluctuations and relaxes back to the band edge. This can happen as $h^+h^+e^-$ or $e^-e^-h^+$ event with equal probability given equal carrier densities. Since this process involves 3 particles, it is usually only relevant in non-equilibrium conditions when there is an excess of carriers. The probability for an Auger event is carrier density dependent

and increases with increasing density, so it is very important in highly-doped materials.

The third main recombination pathway is *Shockley-Reed-Hall (SRH)*, or trap-assisted, recombination. SRH recombination refers mostly to mid- or deep-gap trap states that typically arise from impurities in the crystal lattice. These traps can be carrier specific, especially if they are closer in proximity to one band or the other. Sometimes these traps are incorrectly described as *recombination centers*, but this is only true if the typical trap lifetime is long enough so that an electron or hole can find it and recombine. SRH recombination is particularly important for indirect materials since the trap can absorb changes in momentum.

In some instances, *surface recombination* can be another large source of recombination, usually attributed to the sharp end of the lattice which can contain many recombination centers due to dangling bonds, surface defects, grain or interfacial boundaries. For QDs, this is particularly important since an estimated 15% of total states reside on the surface due to the large surface-to-volume ratio. These surface states must be well passivated otherwise a large number of trap states will be available.

3.4 Current State of QDSC Research

While quantum dots have been researched since the early 1990s, only recently have groups been able to utilize their positive attributes in a solar cell device. During my graduate studies, QD solar cell efficiencies have increased threefold. Starting in 2009, the champion cell was a ITO/ZnO/PbS/Au structured cell [17] with a certified PCE

of 2.9%. This cell was fabricated in an air-free environment, but is otherwise simple to make. A few years later, the Sargent group announced they had reached 6.6% with an ITO/TiO₂/PbS/Au heterostructured device [18]. This huge increase in efficiency was attributed to better QD surface passivation in synthesis, improved electron mobility in the TiO₂ layer, and better transport of carriers. Then, in 2014, the Bawendi group certified the current world record cell, a ITO/ZnO/PbS/Au structure that ditched the imperfect, unstable hole transport MoO₃ layer for a certified PCE of 8.6% with a lab-reported PCE of greater than 9.2%. This device has the highest fill factor reported for any QDSC to date at 67%, due to improved PbS surface passivation and more intelligent ligand exchange. Additionally, the fill factor does not decrease in over 2 months, indicating well-passivated NPs and vastly increased stability.

Figure 5.1 shows the efficiency chart for various solar technologies. Third-generation PV, including semiconductor quantum dots, can be seen in the lower right hand corner, in orange.

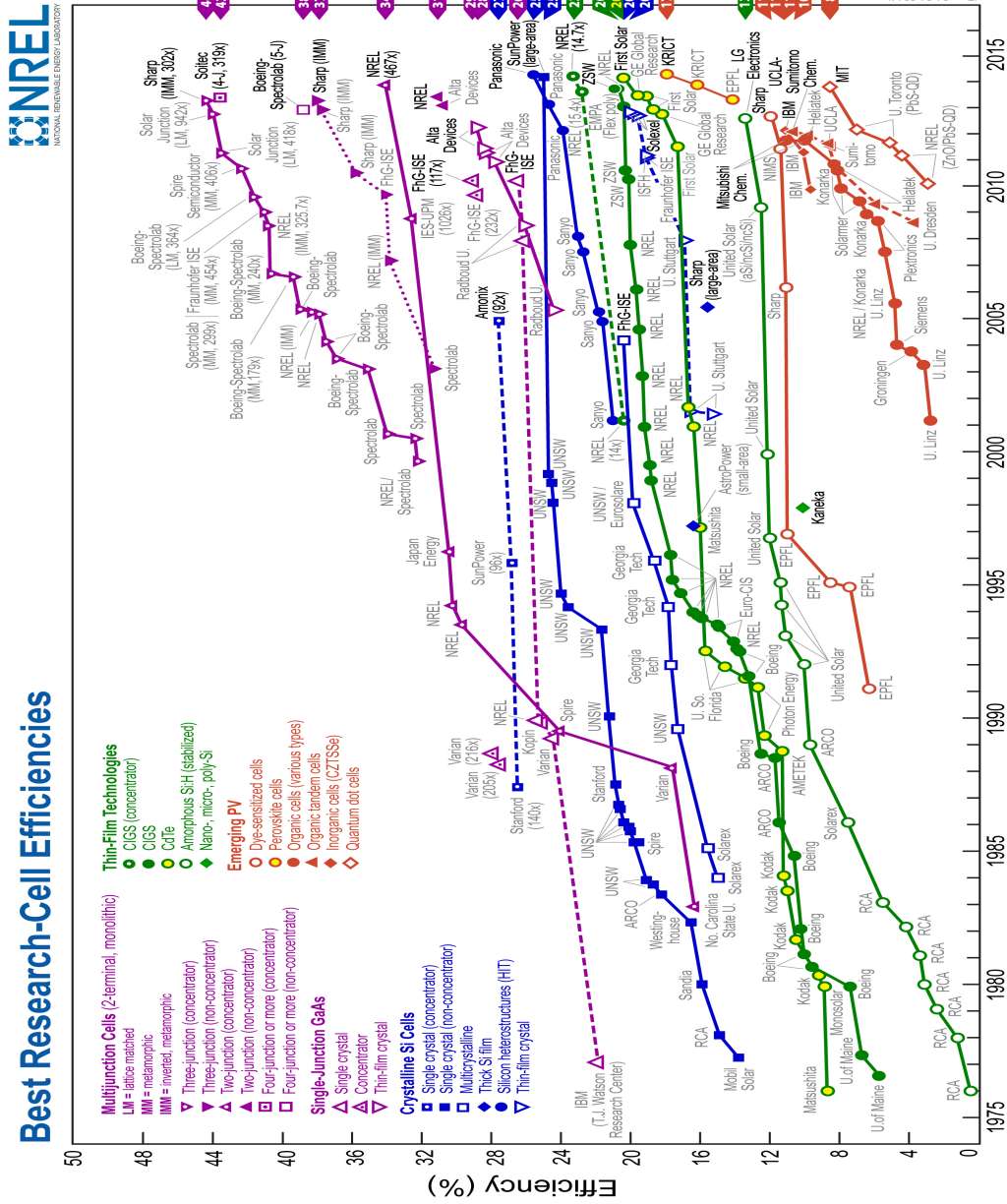


Figure 3.3: The current world champion photovoltaic cells, as certified by NREL and current as of Mar 2014.

Chapter 4

Practical Solar Cells

Before discussing the research performed, it's helpful to briefly introduce how we fabricate and characterize our devices. The optoelectronic device fabrication and characterization methods along with performance metrics used throughout these studies will be discussed in the following chapter.

4.1 Optoelectronic Device Fabrication

The fabrication method is more or less the same for all devices studied in this thesis, save for the active layer. 1" by 1" Corning glass substrates were pre-patterned indium tin oxide (ITO) or fluorine-doped tin oxide (FTO) and purchased from TFD Inc. The materials properties for both TCOs is given below in Table 4.1. The ITO was approximately $145 \pm 10\text{nm}$ thick with a resistivity of $20 \pm 5 \Omega/\text{cm}^2$.

These glass substrates were cleaned by sonicating in solutions of Alconox[®], deionized water (DI H₂O), isopropyl alcohol and ethanol, followed by drying with com-

pressed, desiccated N₂.

Material	Deposition	Work function [eV]	Transmission [%]	Roughness [nm]
ITO	Ion-beam	4.9 ± 0.1	85	5
FTO	CVD	4.7 ± 0.1	80	10

Table 4.1: Transparent Conducting Oxide materials parameters provided by TFD Inc.

TiO₂ sol-gel was prepared by the standard procedure described previously [19]. Briefly, 125 μ L of DI H₂O is added to 5 mL of anhydrous ethanol. 2 drops of concentrated hydrochloric acid (HCl) is added to the ethanol mixture, after which 375 μ L of titanium-ethoxide (99% purim, purchased from Sigma Aldrich) is added. 40 μ L of the TiO₂ sol-gel is spun onto the cleaned glass substrate at \sim 1350 rpm in air. The sides and back of the substrate are cleaned with ethanol, and the sol-gel film is sintered at 450 °C for 30 minutes in air after deposition to facilitate crystal growth from an amorphous anatase phase. After a brief resting period, 40 μ L TiO₂ nanoparticle solution (purchased from Solaronix) is spun onto the sintered sol-gel film \sim 1500 rpm, again in air. The film is again sintered at 450 °C for 30 minutes in air after deposition to improve conduction, primarily through annealing off organic ligands.

The prepared substrates are then brought into the N₂ glovebox for absorber layer deposition. NP inks are comprised of quasi-spherical nanoparticles typically ranging in size from 3 nm-10 nm and dispersed in various organic solvents. For Pb-based devices, the NPs are capped with oleic acid (OA) and dispersed in hexane to concentrations of 50 mg/mL for spinning solutions, and 20 mg/mL in hexane:chloroform for

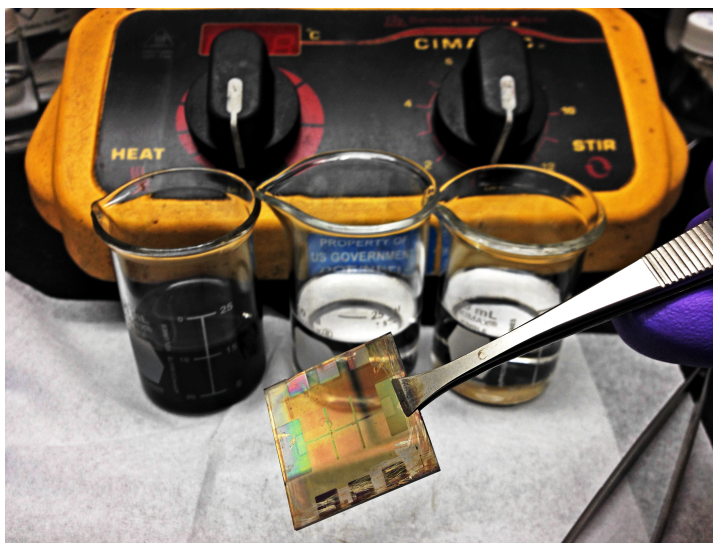


Figure 4.1: Photo of PbS-TiO₂ device being hand dipped. Fabrication is simple, can be done in air, and requires no expensive equipment. From left to right the beakers contain the PbS ink, MPA in ACN for ligand exchange, and an ACN wash.

dipping solutions. For Ge, the NPs are capped with oleylamine (OAm) and dispersed in toluene to concentrations of 5-30 mg/mL. These inks are deposited by spin casting or hand dipping onto the TiO₂ covered ITO substrates. The thickness of the QD film is controlled by spin (hand) speed, number of cycles, and concentration of the QD ink. Figure 4.1 shows a QD PbS film being deposited by hand dipping in air. For both absorbers, no anneal was performed; this is important as annealing tends to recover the bulk properties of the material, so by not annealing the beneficial quantum confinement properties may be retained. The dried NC films then undergo ligand exchange, which is accomplished by immersing the substrate into a solution of 1M hydrazine, pyridine, or 1,2-ethanedithiol (EDT) in acetonitrile for 15 seconds. Table 4.2 shows the various ligands used for capping and exchange and their structures.

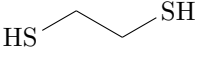
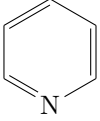
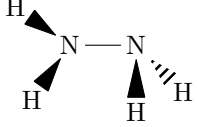
Ligand	Structure	Molecular Formula
1,2-ethanedithiol (EDT)		$C_2H_4(SH)_2$
pyridine		C_5H_5N
hydrazine		N_2H_4

Table 4.2: Chemical structures of ligands used in PbS and Ge device fabrication.

Finally, 100 nm of various back contacts were thermally evaporated in the oxygen-free glovebox under high vacuum at a base pressure of 10^{-6} Torr. Pb-based devices used gold (Au) as their back contact, while Ge devices used Au, silver (Ag), calcium (Ca), aluminum (Al), or magnesium (Mg). The area of each device formed is 0.03 cm^2 . Figure 4.2 shows the top-down flat schematic and side-view of our device stacks.

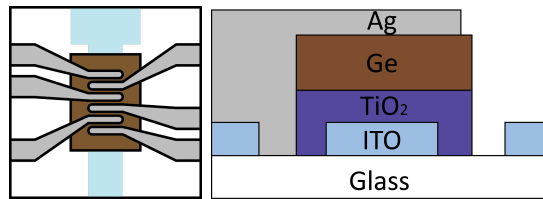


Figure 4.2: Left: Top-down flat schematic of device showing ITO pattern (light blue), Ge NP layer (brown), and Ag back contact pattern for 1"x1" substrates, with 6 devices on each substrate. The area of each device formed is 0.03 cm^2 . Right: Side view of device stack.

All device fabrication work involved in this thesis was completed in an air-free N_2 environment with O_2 concentrations under 50 parts per million, unless otherwise specified.

4.1.1 Ligand Exchange

As synthesized and deposited (without anneals)¹, the QDs are electrically insulating due to barriers formed between them from the long, insulating organic ligands. These ligands serve a variety of purposes from controlling growth kinematics during synthesis, to surface passivation and enabling a stable colloidal solution after growth, and to setting interdot distances in a film. A crucial step in colloidal QD device fabrication is known as *ligand exchange*. Simply put, these long capping ligands used during synthesis are exchanged, either in solution or solid state, with a much shorter ligand, decreasing the barriers between the NCs in a film. A cartoon image of what is occurring during ligand exchange is shown in Figure 4.4.

Recently, the role ligands have on the resultant electrical properties of the NCs has been investigated. Many ligands are able to dope the NC, while other ligands, such as hydrazine, have been found to increase conductivities by orders of magnitude [20]. Additionally, there are many reports of large surface treatment-dependent valence band shifts due to the creation of a QD-ligand surface dipole [21, 22], which needs to be addressed for efficient photovoltaic device design.

¹Though annealing tends to rid the films of their quantum confinement properties, it can be helpful as it is another method of increasing the conductivity of the film due to complete or partial ligand removal, along with grain and crystal growth.

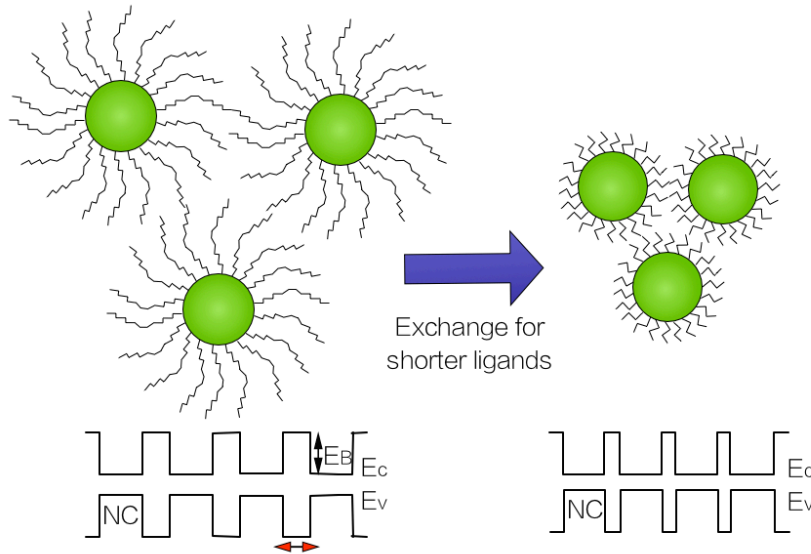


Figure 4.3: Schematic showing what happens during ligand exchange. Initially, particles are capped with long, insulating ligands. After exchanging them with shorter ligands, the potential barrier between dots decreases, increasing the conductivity of the NC film. The black arrow represents the barrier height, while the red arrow represents the barrier width.

4.2 Solar Cell Device Characterization

When light is incident on a solar cell, a *photocurrent* and a *photovoltage* are produced. The relationship between these quantities is the main way researchers judge the merits of a solar cell.

Light testing is typically done using a solar simulator while biasing the device from $[-1, 1V]$. These simulators are intensity and spectrum matched to NREL calibrated Air Mass (AM) values, which are simply measures of the optical path length sunlight must travel through the atmosphere before impinging on the solar cell, with typical spectrum values of AM0 (zero atmosphere, i.e. space), AM1.5G (where G=global and

contains direct and diffuse radiation), and AM1.5D (where D=direct radiation only). Both AM1.5G and D correspond to a zenith angle of 48.2° . Figure 4.3 shows NREL calibrated spectra for AM0, AM1.5D, and AM1.5G, with spectral intensity of AM1.5G normalized to 1000W m^{-2} .

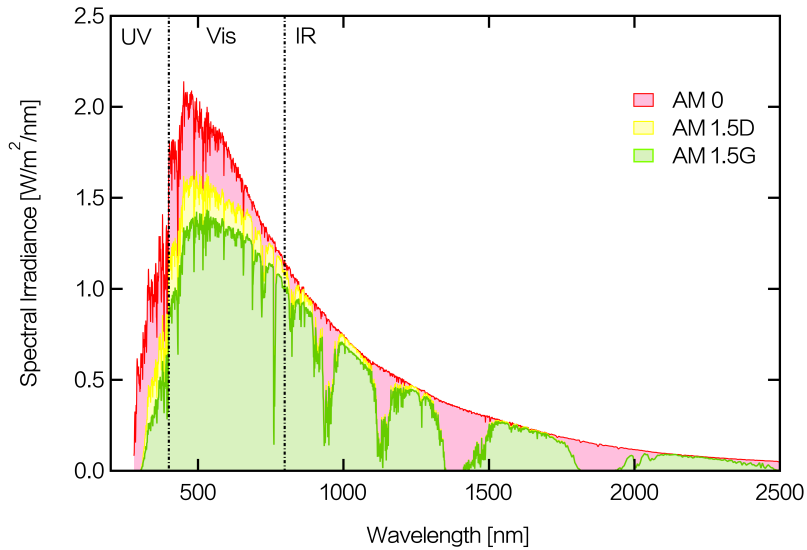


Figure 4.4: NREL calibrated solar spectrums, AM0, AM1.5G, and AM1.5D

A photodiode with known response to the desired spectra is then used to calibrate individual solar simulators across labs.

4.2.1 Current-Voltage Analysis

An ideal solar cell can be modeled by an equivalent circuit consisting of a current source in parallel with a diode. For diodes, typical device performance is judged by the

current-voltage analysis, also known as the diode’s characteristic curve. Because we are modeling the system as a diode, we can start with the ideal diode equation for a device in the dark:

$$I_{dark}(V) = I_0(e^{\frac{qV}{k_B T}} - 1) \quad (4.1)$$

Current is a measure of charge flux and depends on area; to remove this dependence it is typical to use the *current density* J when speaking of solar cells to normalize performance across different cell sizes. Under illumination, both a photocurrent and photovoltage are produced. Then, the total current-voltage (JV) characteristic of a solar cell can then be represented by the sum of its dark current and photocurrent (Equation 4.2). The photocurrent can be approximated by the short-circuit current, J_{sc} , which is the current that flows when the contacts are shorted².

$$J(V) = J_{sc} - J_{dark}(V) \quad (4.2)$$

Then, from Equation 4.1 for an ideal diode, we have:

$$J = J_{sc} - J_0(e^{\frac{qV}{k_B T}} - 1) \quad (4.3)$$

It has been shown that the J_{sc} is mainly sensitive to the absorption and morphology of the active layer. It is also intensity-dependent through its absorption dependence.

The photovoltage can then be found from Equation 4.3 by letting $J \rightarrow 0$,

$$V_{oc} = \frac{kT}{q} \ln\left(\frac{J_{sc}}{J_0} + 1\right), \quad (4.4)$$

²Also called the zero load limit.

where it is represented by the open-circuit voltage, V_{oc} , defined as the maximum voltage a solar cell can generate under an external load³. This occurs when the dark current and photogenerated current cancel out ($J(V)=0$). Thermodynamically, V_{oc} represents the maximum free energy available in the system to do work (potential) on a carrier, and because of that, is always limited by the bandgap of the material. It is also often thought of as a measure of recombination. Additionally, due to the linear dependence on temperature, the maximum theoretical V_{oc} decreases monotonically as temperature increases. Traditionally, in PV V_{oc} is defined so that it occurs in positive bias, i.e $V \geq 0$. At $V < 0$ the device acts as a photodetector, consuming power to generate a photocurrent.

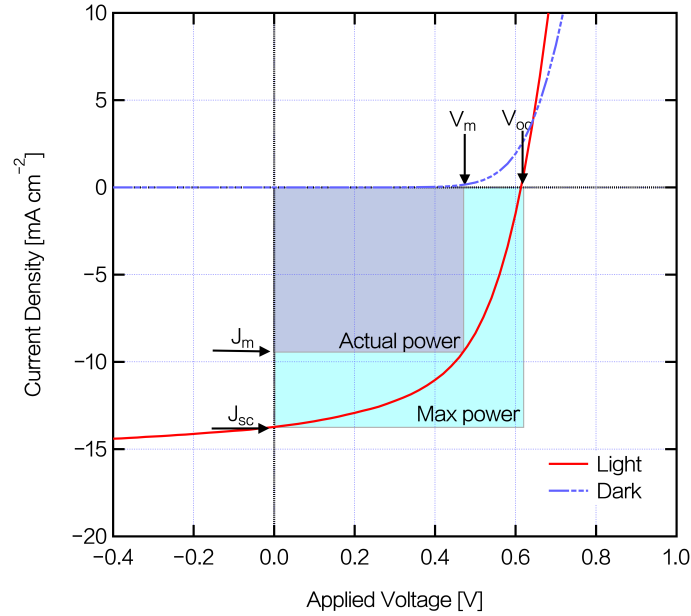


Figure 4.5: Figures of merit from the current-voltage curve of a photovoltaic device, showing operating point, J_{sc} , V_{oc} , and how fill factor is related to them. The fill factor for this particular device is close to 54%, leading to a η of over 4.5%.

³Also known as the infinite load limit

4.2.1.1 Non-ideal parasitic effects

A true solar cell is not an ideal diode, but also contains some contribution from parasitic losses (non-ohmic contacts, leaking around the active areas, etc.). These losses can be modeled by resistors in parallel and series to the diode, with the equivalent circuit of a solar cell shown in Figure 4.8.

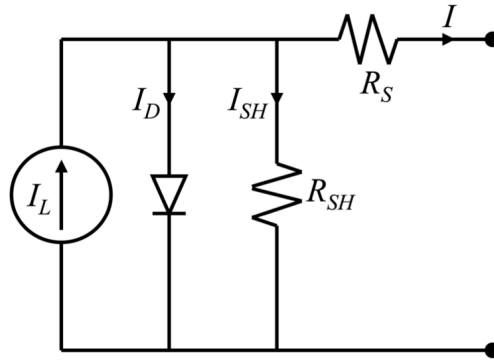


Figure 4.6: Equivalent circuit for a photovoltaic device..

R_s is mostly attributed to contact or interfacial resistivity. It can be approximated by the slope of the JV curve at J_{sc} . In an ideal solar cell, $R_s \rightarrow 0$.

R_{sh} is strongly related to recombination. It can be approximated by the slope of the JV curve at V_{oc} . In an ideal solar cell, $R_s \rightarrow \infty$

4.2.2 Fill Factor and Power Conversion Efficiency

Fill Factor (FF) is simply defined as the ratio between maximum power output and actual power output of a solar cell. It is a measure of the "squareness" of the JV

curve and expresses the performance quality of the device. Mathematically, it is

$$FF = \frac{V_m J_m}{V_{oc} J_{sc}} \quad (4.5)$$

where V_m and J_m are the maximum voltage and current operating points. Typically, real world solar cells are biased at the V_{oc} or close to the V_m for operation. FF is heavily influenced by recombination through its V_{oc} dependence.

Finally, we can define the *PCE or* (η) of a solar cell. It is the ratio of input power to output power, or

$$\eta = \frac{V_m J_m}{P_s} \quad (4.6)$$

where P_s is the incident light power density. It is simply related to the other figures of merit by the following

$$\eta = \frac{V_{oc} J_{sc} FF}{P_s}. \quad (4.7)$$

4.2.3 Incident Photon to Carrier Efficiency

Incident Photon to Carrier Efficiency (ICPE) or *External Quantum Efficiency (EQE)* is a spectrally resolved measure of the power output of the solar cell, or

$$EQE = \frac{\text{electrons/sec}}{\text{photons/sec}} = \frac{\text{current}/e^-}{\text{total power of photons/E of one photon}} \quad (4.8)$$

It is simply related to J_{sc} through the following relationship:

$$J_{sc} = q \int b_s(E) QE(E) dE \quad (4.9)$$

where the experimentally determined J_{sc} is often used to confirm the validity of the EQE spectra.

QE depends on the absorption coefficient of the PV material, the efficiency of charge separation, and the efficiency of charge collection in the device, but does not depend on the incident spectrum. Therefore, it is a key quantity in describing solar cell performance under different conditions [5].

A similar quantity is the *Internal Quantum Efficiency (IQE)*, which is

$$IQE = \frac{EQE}{\text{absorption}} = \frac{EQE}{1-R-T} \quad (4.10)$$

This quantity accounts for absorption losses in the device so is typically higher than EQE values. It is often reported in studies of MEG.

Both EQE and IQE are measured by passing light from the solar simulator through a monochromator to get wavelength-specific current values, then comparing those values to a calibrated Si photodiode whose response is known.

Part II

Pb-Chalcogenide Quantum Dot

Solar Cells

Chapter 5

Introduction

Lead salts (PbX where X=Te, Se, S) are the prototypical NC systems to study for a number of reasons. First, they all have large exciton Bohr radii (80, 46, 20nm) which lead to dramatic variation in confinement energy with NC size. This large confinement energy arises from a combination of small effective masses and large high-frequency dielectric constants [23]. Secondly, they are IR absorbers in the bulk ($E_g=0.27, 0.6\text{eV}$ for Se, S) and so even with large confinement increases of $\sim 400\text{meV}$ this places these materials in the 0.8 eV range, which is the optimum bandgap for high MEG current enhancements. Not only that, under confinement these materials have bandgaps which can span the entire solar spectrum, enabling further efficiency improvements through fabrication of multi-junction cells from the same material. This is better for a number of reasons, but one can motivate it just through the ease of deposition and lack of lattice mismatch.

PbS is the primary solar conversion candidate for QDs, mainly due to a rela-

tively high V_{oc} leading to the highest QDSC efficiencies. Unfortunately, these efficiencies are still quite low compared to thin-film PV technologies, and even low amongst the third-generation candidates, due to lower V_{oc} than other candidates¹, limited absorption despite their higher oscillator strengths, and typically low FF due to high recombination. Conversely, it is widely accepted that PbSe is the higher photocurrent producer and additionally, is a better candidate for MEG enhancement; indeed, the only device to show these MEG effects used PbSe as its active absorber layer [15]. Unfortunately, PbSe is even more susceptible to oxidation, defects, and trap states than PbS, so overall efficiencies have hovered around 4% for quite some time.

Generally, there are two routes to increasing photovoltaic performance: increase the photocurrent or increase the photovoltage. MEG enhancements can lead to current boosts by increasing generation while voltage is always limited by the bandgap and recombination. In the two following chapters, we explore these different approaches to increasing the performance of Pb-chalcogenide based solar materials.

¹For example, lead iodide Perovskite solar cells recently reached 15% efficiencies with a V_{oc} of over 1V.

Chapter 6

PbS_{1-x}Se_x -TiO₂ Solar Cells

We report on photovoltaic cells based on ternary PbS_{0.9}Se_{0.1} quantum dots (QDs) utilizing a heterojunction type device configuration. The best device shows an AM 1.5 power conversion efficiency of 4.25%. Furthermore, this ternary PbS_xSe_{1-x} quantum dot heterojunction device has a peak external quantum efficiency above 100% at 2.76 eV, approximately 2.7× the bandgap energy. The ternary quantum dots combine the higher short circuit currents of the binary PbSe system with the higher open circuit voltages of the binary PbS system. This majority of this material was published in 2012 in the *Applied Physics Letters* [24].

6.1 Introduction

PV devices with active layers consisting of films formed by colloidal IV-VI QDs have attracted considerable attention due to their low-cost solution processability, desirable electrical properties [25], high photoactivity in the near-infrared spectral region

and potential ultrahigh conversion efficiencies via multiple exciton generation (MEG) [26, 9] in the past few years [10, 27, 28]. So far, Schottky and heterojunction solar cells based on binary IV-VI QDs, such as PbS and PbSe, have been intensely investigated and great progress in device fabrication and performance has been made. However, solar cells employing ternary $\text{PbS}_x\text{Se}_{1-x}$ QDs have not received as much attention even though it has been demonstrated that $\text{PbS}_x\text{Se}_{1-x}$ QDs can maintain the advantages of both binary compound counterparts [29]. The few papers [29, 30] on ternary $\text{PbS}_x\text{Se}_{1-x}$ QD solar cells demonstrate an efficiency of $\sim 3.4\%$ in a Schottky junction device. However, Schottky junction solar cells have several drawbacks which potentially impede further improvement of device performance [31, 5]. Heterojunction solar cells can overcome the limitations of Schottky architecture by introducing a charge-dissociating junction formed between QD films and transparent metal oxide layers, such as TiO_2 and ZnO . Moreover, only heterojunction structures have shown MEG in working solar cell devices.

MEG in quantum dot systems has been mainly observed in colloidal QD solutions [9, 10, 11] and films [14, 12, 13] via spectroscopic measurements to date. An absorbed photon-to-current efficiency greater than 100%, namely internal quantum efficiency $>100\%$, has recently been reported in a photoelectrochemical cell composed of a monolayer of PbS QDs chemically bound to single crystal TiO_2 [32]. The sensitivity of QD devices to environmental condition [33] and significant optical interference and scattering of multi-layer stack in devices implies that the only conclusive measurement of MEG is an external quantum efficiency (EQE) above 100% in working solar cells. Despite some Schottky junction devices showing high J_{sc} [34], MEG has not been

shown to exist in these devices. The NREL group has very recently reported a peak EQE exceeding 100% in ZnO/PbSe QD devices [15], in which PbSe QDs were treated by 1,2-ethanedithiol (EDT) and hydrazine sequentially, showing conclusive evidence for MEG in QD heterojunctions. Nonetheless, these results largely occurred at energies above 2.8 eV, where solar intensities are too low to take advantage of MEG to achieve higher J_{sc} .

Here, we report on the fabrication and characterization of heterojunction solar cells consisting of a TiO_2 window layer and a ternary $\text{PbS}_x\text{Se}_{1-x}$ QD absorber layer. We show that both high photocurrents and reasonable V_{oc} are achieved simultaneously in such devices. The best AM 1.5 power conversion efficiency of these devices is 4.25%, representing an improvement of about 30% compared to its former Schottky counterpart [29]. Moreover, we demonstrate a peak EQE above 100% in EDT treated ternary $\text{PbS}_x\text{Se}_{1-x}$ QD heterojunction devices at energies less than 2.7x the bandgap energy, and thereby directly demonstrate the existence of MEG-like phenomena in $\text{PbS}_x\text{Se}_{1-x}$ QD devices at solar relevant energies. Even though EDT was reported to reduce MEG efficiency of binary QDs [12], we observe these results in the absence of hydrazine, suggesting that MEG can still preserve even in the EDT treated QD devices by selecting the appropriate QDs and optimizing device fabrication. Our research demonstrates that the $\text{PbS}_x\text{Se}_{1-x}$ system is promising for utilizing MEG while retaining high V_{oc} to achieve higher efficiency quantum dot solar cell devices.

6.2 Experimental Methods

Lead oxide (PbO, 99.999%), selenium (99.99%), oleic acid (OA, 90%), diphenylphosphine (DPP, 98%), bis(trimethylsilyl) sulfide (TMS₂-S, synthesis grade), 1-octadecene (ODE, 90%), Titanium(IV) ethoxide (technical grade), anhydrous solvents were purchased from Sigma-Aldrich and used as received. Trioctylphosphine (TOP, >96%), 1,2-ethanedithiol (EDT, > 95%) and TiO₂ nanoparticle pastes were acquired from Cytec, Alfa Aesar, and Solaronix, respectively. Standard air free techniques were used throughout synthesis and purification process. Ternary PbS_xSe_{1-x} QDs, provided by Solexant, were synthesized using a variation on a literature route [29]. Briefly, 1.38 g of PbO, 4.2 g of OA, and 30 g of ODE were mixed in a three necked flask and then degassed and heated at 150 C for one hour to dissolve the PbO and dry the solution. The temperature was then lowered to 118°C, and a mixture of 1 M TOP/Se solution (2.1 mL), TMS₂-S (189 μL), DPP (120 mg), and ODE (3.6 mL) was rapidly injected. The total amount of Se and S precursor was 3 mmol with the ratio of 7:3. The reaction was quenched after 20 seconds by injecting 20 mL of room temperature hexane to halt the nanocrystal growth. The QDs were purified with isopropanol and finally dispersed in octane to achieve a concentration of 50-100 mg/mL.

The TiO₂ sol-gel was prepared using titanium-ethoxide as precursor by the standard procedure described previously [19]. The TiO₂ sol-gel and nanoparticle paste were spin-coated onto a cleaned glass substrate with prepatterned ITO electrodes of 150 nm thickness (Thin Film Devices, Anaheim) sequentially. Both TiO₂ sol-gel (~75-100

nm thick) and nanoparticle (~ 225 - 250 nm thick) layers were sintered at 450 °C for 30 min in air to improve conductivity. The $\text{PbS}_x\text{Se}_{1-x}$ ternary QD film was deposited onto the TiO_2 film via multilayer spin-coating QD ink in nitrogen-filled glove box. Each $\text{PbS}_x\text{Se}_{1-x}$ layer was treated briefly by immersing the substrate into EDT in solution (1% , v/v) for around 15 seconds to increase electronic coupling between the QDs. The thickness of QD film was controlled by adjusting spin-coating speed, iteration times and concentration of QD ink. Finally, 100nm of gold contact was thermally evaporated under high vacuum ($10^{-5} - 10^{-6}$ Torr) at a rate of 0.6 \AA/s . The area of each device formed is 0.03 cm^2 .

All device characterizations were carried out in nitrogen-filled glove box, at an oxygen partial pressure below 50 ppm. JV curves were taken using a calibrated solar simulator and a Keithley 2400 source meter, and EQE curves were taken using the solar simulator coupled into an Oriel monochromator. In monochromatic measurement experiments, diode lasers of 405 nm and 447 nm were used as light sources. For light intensity dependent experiments, a set of neutral density filters (Newport) were used to adjust the intensity of light source. A Shimadzu UV-3101PC UV-VIS-NIR spectrometer was used to measure the absorption spectra of ternary $\text{PbS}_x\text{Se}_{1-x}$ QD solution. Optical properties of ternary QD films were measured via a StellarNet TF-C-UVIS-SRN dual spectrometer. Transmission electron microscopic (TEM) images were taken using a Philips CM200UT electron microscope. The topography and thickness of $\text{PbS}_x\text{Se}_{1-x}$ QD film was obtained by an atomic force microscope (AFM) operating in tapping mode. A Hitachi S-4800 II field emission scanning electron microscope was employed to observe

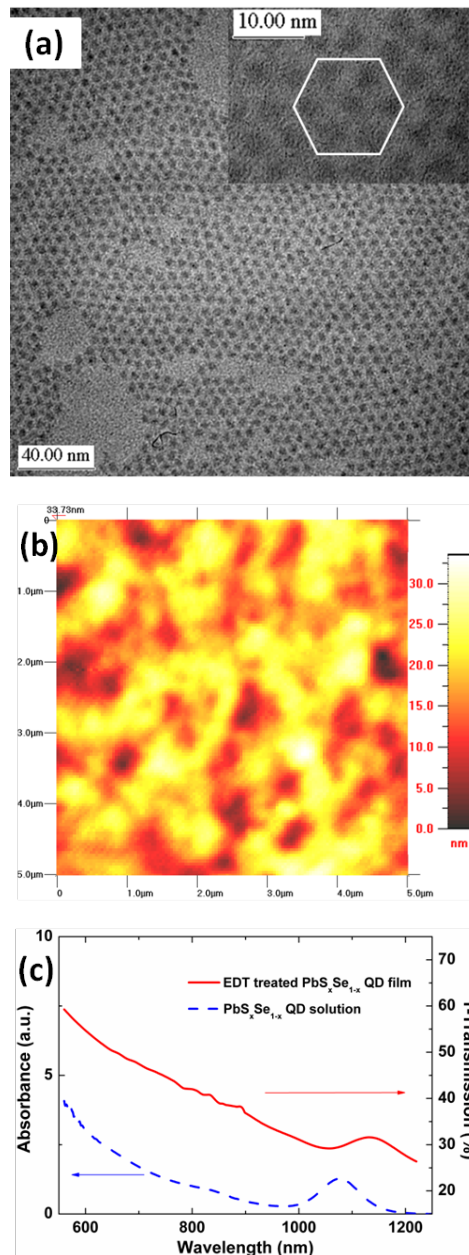


Figure 6.1: Characterization of $\text{PbS}_x\text{Se}_{1-x}$ ternary QD inks and films used in this work. (a) TEM image of ternary $\text{PbS}_x\text{Se}_{1-x}$ QDs. Inset: showing these QDs tend to self-assemble into a hexagonal array. (b) an atomic force microscopic topographical image of a $5\mu\text{m} \times 5\mu\text{m}$ area of the EDT-treated QD film on a glass substrate. (c) room-temperature optical absorption spectra of QD ink in tetrachloroethylene (blue dashed line) and as a film treated with EDT (red solid line).

the cross section of device and confirm the thickness of each layer. Energy dispersive X-ray spectroscopy (EDX) measurements were taken via an EDX spectrometer attached to the HR-SEM.

6.3 Results

Figure 6.1a shows TEM images of $\text{PbS}_x\text{Se}_{1-x}$ QDs employed in this work. These images reveal the formation of quasi-spherical nanocrystals with diameter of around 3.4-3.5 nm. The ensemble of QDs in the images exhibited that ternary nanocrystals have a diameter distribution of $<15\%$ and were self-organized into a hexagonal array. EDX results (Figure 6.2) indicate that $x=0.90 \pm 0.05$, i.e. that our QD is comprised of $\text{PbS}_{0.9}\text{Se}_{0.1}$. Figure 6.1b shows an AFM topography image of a $\text{PbS}_x\text{Se}_{1-x}$ QD film treated with EDT on a glass substrate. The surface of ternary QD film has a root mean square roughness of 4 nm.

The room-temperature absorption (blue dashed line) of $\text{PbS}_x\text{Se}_{1-x}$ QDs capped with oleic acid molecules is shown in Figure 6.1d. The spectrum exhibits an obvious sharp absorption peak at the wavelength of 1076 nm due to strong quantum confinement effect, which also indicates the narrow size distribution of QDs employed here. The red solid line in Figure 6.1d represents the absorption of spin-cast QD film treated with EDT. Both absorption spectra appear to be nearly identical in shape except for the red-shift of the first exciton in the EDT treated film by around 60 meV likely due to strengthened dipole-induced dipole interactions and wavefunction delocalization [35].

According to the relationship between nanocrystal diameter and absorption band gap for binary PbS [36] and PbSe [37] QDs reported previously, the obtained x value of ternary $\text{PbS}_x\text{Se}_{1-x}$ QDs would be approximately 0.8 ± 0.1 . This value is lower than what is suggested by our EDX measurements, but consistent with the relatively large uncertainties for both measurements.

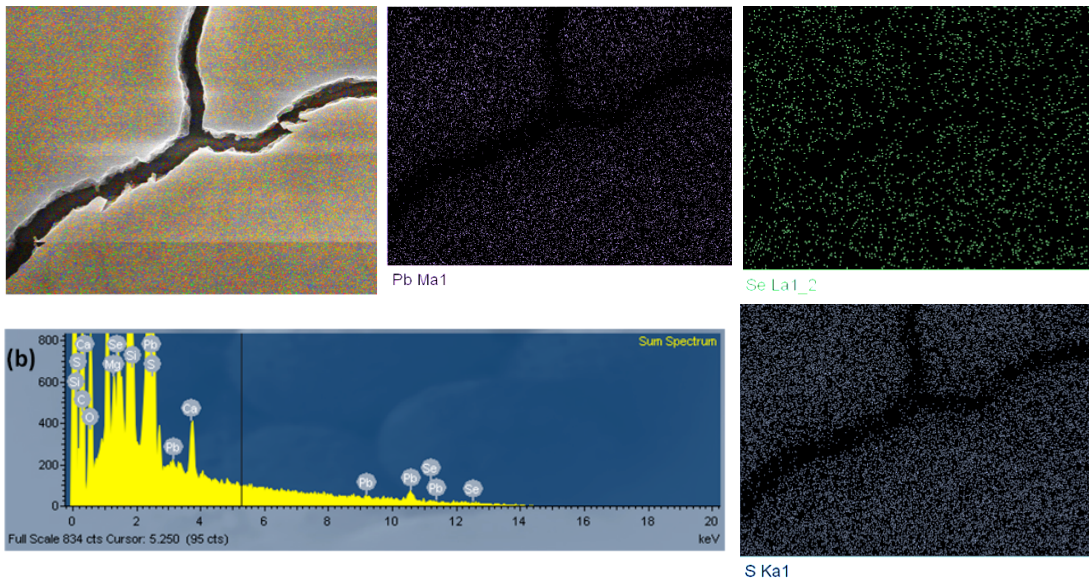


Figure 6.2: (Color online.) EDX data for a film of $\text{PbS}_x\text{Se}_{1-x}$ ternary QD on quartz glass. HRSEM image of the film overlaid with colored hits for Pb, Se, and S. Individual maps of counts for Pb, Se, and S are also shown, while (b) shows the full EDX result.

The structure and cross-sectional HR-SEM image of a photovoltaic device incorporating n-type TiO_2 sol-gel and nanoparticle layers and a p-type ternary $\text{PbS}_x\text{Se}_{1-x}$ QD layer are presented in Figure 6.3. We studied the effects of ternary $\text{PbS}_x\text{Se}_{1-x}$ QD film thickness on solar cell performance. We note that the thickness of $\text{PbS}_x\text{Se}_{1-x}$ QD films herein was determined from QD films deposited on glass substrates with same

spin-cast process as that for the devices. Considering the roughness of TiO₂ NP film and expected penetration of QDs into mesoporous TiO₂ film as depicted in Figure 6.3, the maximum actual thickness of PbS_xSe_{1-x} QD films which photogenerated charge carriers might need to travel between QD-Au interface and QD-TiO₂ interface in devices may be up to 100 nm less than the measured PbS thickness. Here, for convenience we still use the thickness values obtained from QD films on glass to label them.

Figure 6.3a shows the dependence of J_{sc} on PbS_xSe_{1-x} QD film thickness for such solar cells. It is clear that J_{sc} increases with QD film thickness initially and then peaks when the film thickness reaches ~ 360 nm, which is near the thickness where the absorption reaches nearly 100% at 400 nm. As the thickness of QD film further increases, J_{sc} starts to decrease. FF, as shown in Figure 6.3b, experiences a slight reduction with increasing thickness of the PbS_xSe_{1-x} QD film. Within our experimental error, V_{oc} remains unchanged on increasing the QD film thickness (Figure 6.4). Therefore, the changes in the PCE of devices with increasing QD film thickness (Figure 6.3b) resembles the trend of J_{sc} .

For reasonable device performance, the photogenerated excitons must effectively dissociate, travel through the PbS_xSe_{1-x} film, and be collected by electrodes within QD film and/or interfaces between QD film and electrodes (TiO₂ and Au), which is strongly affected by the thickness of QD film and quality of interfaces. As illustrated in Figure 6.2a, the rough surface of our mesoporous TiO₂ NP layer results in the formation of quasi-bulk heterojunction region in the vicinity of QD-TiO₂ interface, which would allow much more QDs loaded on TiO₂ film comparing to regular planar heterojunction

structure and thereby facilitates the achievement of sufficient light absorption without sacrificing efficient dissociation, transportation and extraction of photogenerated charge carriers in devices.

This benefit is similar to depleted bulk heterojunction PbS QD devices previously reported [38]; however, for our devices a tradeoff exists between light absorption and efficient carrier collection as a bulk heterojunction structure is not formed throughout the whole active layer. We ascribe the increase of J_{sc} before PbS_xSe_{1-x} QD film reaches 360 nm thick to additional excitons photoexcited in thicker films. The main discrepancy on EQE in near infrared region for the devices with 240 nm and 360 nm thick PbS_xSe_{1-x}QD films, shown in Figure 6.5b, supports that the lower J_{sc} of thinner devices is limited by light absorption. The following decrease of J_{sc} with further increasing thickness of QD film is likely due to the recombination loss of charge carriers in too thick QD film.

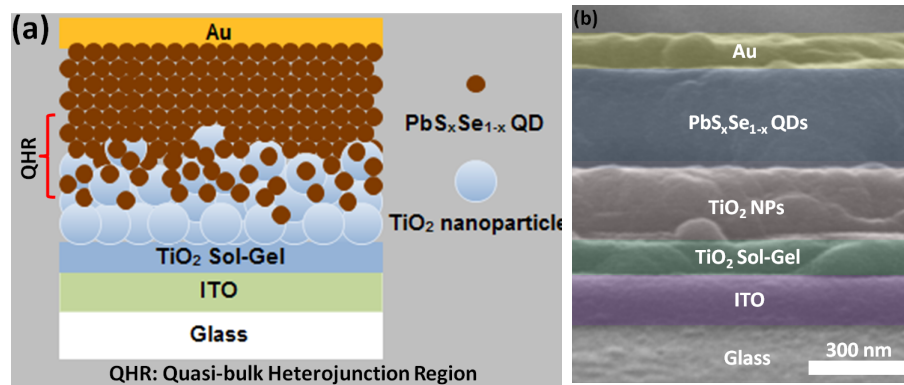


Figure 6.3: (a) Schematic of the PbS_xSe_{1-x}QD/TiO₂ heterojunction solar cell. Note that the thickness of each layer is not proportional to their actual thickness in real devices. The quasi-bulk heterojunction region is highlighted here. (b) Cross-sectional HR-SEM of the PbS_xSe_{1-x}QD/TiO₂ solar cell illustrated in (a).

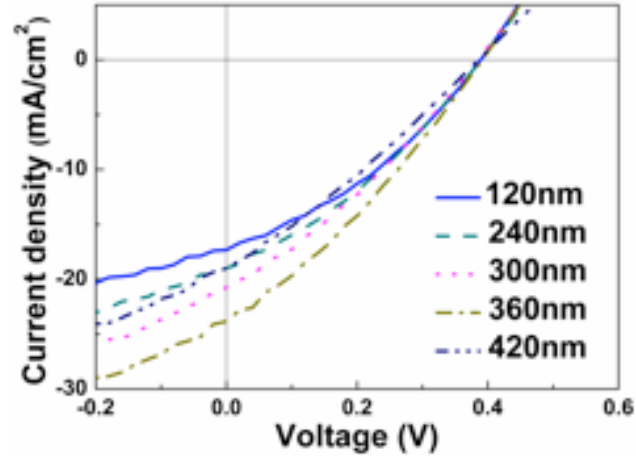


Figure 6.4: Current density-voltage (J-V) characteristics of $\text{PbS}_x\text{Se}_{1-x}$ QD heterojunction solar cells incorporating different thickness of active layers under 100mW cm^{-2} simulated AM 1.5G illumination. The devices were measured after ~ 24 -hour aging in N_2 - filled glove box.

Fill factor is a more complicated parameter compared to J_{sc} and V_{oc} as it is affected by a lot of factors. The reduction of FF with increasing QD film thickness observed in this work was also reported in titanium oxide/conjugated polymer photovoltaics with similar device configuration [19], which is induced by resistive loss of charge carriers in QD film. The increase of FF with lowering light intensity was also observed in our work, indicating that the loss is less important at low intensities due to the direct relationship between the power and current flowing through a resistive layer [19].

The $\text{PbS}_x\text{Se}_{1-x}$ QD heterojunction solar cells stored in the dry nitrogen glove box showed improvements in V_{oc} and FF over days without reduction in J_{sc} , reaching a maximum improvement in 1-3 days of storage. A similar phenomena exists in our heterojunction solar cells based on binary PbS QD treated with EDT [39], which also

resembles the aging effects reported very recently in ZnO/PbSe QD devices though treated with EDT + hydrazine instead of EDT only [15]. Unless stated otherwise, our data were taken after the initial rise in performance.

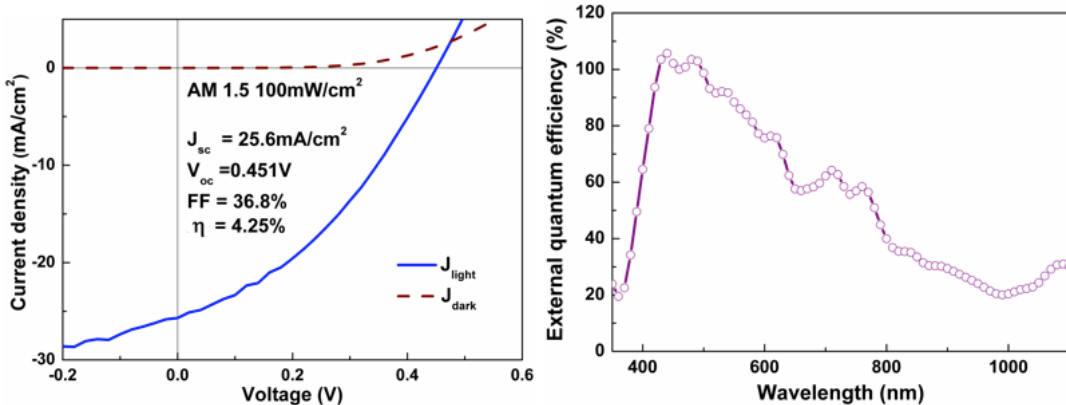


Figure 6.5: (a) Current density-voltage (J-V) characteristics of a $\text{TiO}_2/\text{PbS}_x\text{Se}_{1-x}$ QD heterojunction solar cell with best performance under 100 mW cm^{-2} simulated AM 1.5G illumination. (b) External quantum efficiency (EQE) curve of the ternary QD heterojunction solar cell characterized in (a).

Figure 6.5a shows the J-V characteristics of our best solar cell which composes of $\sim 360 \text{ nm}$ thick $\text{PbS}_x\text{Se}_{1-x}$ QD film. The solar cell exhibited a J_{sc} of 25.6 mA/cm^2 , V_{oc} of 0.451 V , fill factor of 36.8% , and an overall power conversion efficiency of 4.25% under illumination of 100 mW/cm^2 simulated AM 1.5G light, which represents $\sim 30\%$ improvement of device performance compared to ternary $\text{PbS}_x\text{Se}_{1-x}$ QD Schottky junction devices reported previously [29]. The J_{sc} of such ternary QD device is also much higher than that of our previous binary PbS QD device [40].

The EQE spectrum of corresponding solar cell, as shown in Figure 6.5a, was measured from 350 to 1100 nm relative to that of a calibrated Si photodiode from New-

port. Integrating the product of the EQE and the AM 1.5G spectrum from 350 to 1100 nm yields J_{sc} of 24.1 mA cm^{-2} , which is in good agreement with that extracted from J-V curve given that the photocurrent contribution beyond 1100 nm is not accounted for. The device shows peak EQE exceeding 100% (i.e. $\sim 105\%$) at 440 nm, indicating the existence of MEG-like behavior in $\text{PbS}_x\text{Se}_{1-x}$ QDs at much lower energies than have been previously reported [15]. However, the EQE of devices starts to drop with further decrease of light wavelength probably due to the gradually increased absorption and reflection of ITO glass and TiO_2 layers (see Figure 6.6). Significant interference peak at about 730 nm can also be seen in the EQE spectrum due to the built-up of optical mode in dielectric stack of devices. As expected, the position of these interference peaks shifts with change of $\text{PbS}_x\text{Se}_{1-x}$ QD film thickness, as shown in Figure 6.7.

6.3.1 Monochromatic Device Performance

We measured the EQE of the same device with a new Thorlabs calibrated silicon photodiode and two diode lasers (447 nm and 405 nm) to check the accuracy of our EQE measurements shown above via the Newport calibrated silicon photodiode. As shown in Figure 6.8a, we obtained the EQE of $101 \pm 4.6\%$ at 447 nm at different laser intensities, which agrees with the EQE spectrum above. The EQE of the device at 405 nm also shows agreement with EQE spectrum (inset in Figure 6.8). The slight decrease in the EQE at 405 nm with increasing illumination intensity ($> 10 \text{ mW/cm}^2$) is probably due to reduced recombination lifetime of charge carriers under stronger illumination [41]. All EQE $< 100\%$ at different 405 nm laser intensity also confirms the

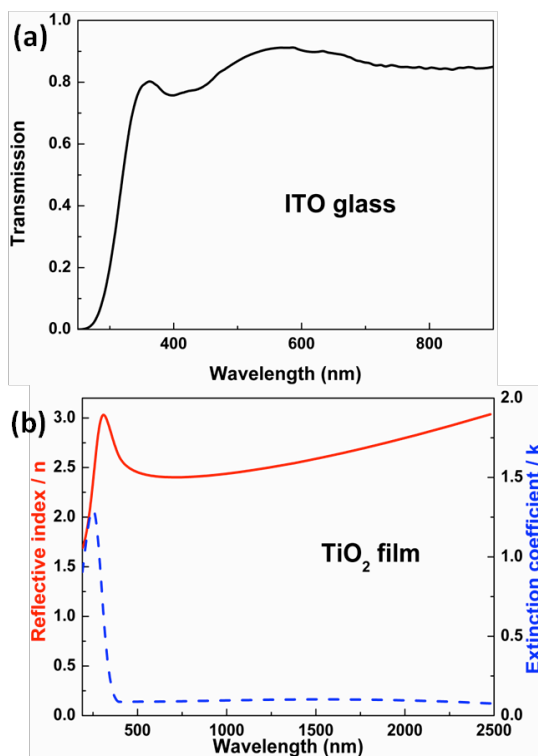


Figure 6.6: (a) Transmission spectrum of ITO glass using air as background. (b) Extinction coefficient and reflective index of TiO_2 sol-gel film.

observation in the EQE spectrum shown above that quantum efficiency is lower than 100% in short wavelength portion of the light spectrum (< 440 nm) most likely caused by light loss in ITO glass and TiO_2 layers. Enhanced interfacial recombination of charge carriers excited by these high energy photons may also contribute to the drop in EQE [15]. A similar drop of EQE in the region of 400-500 nm was also observed in IV-VI QD devices with comparable structure by other groups while their peak EQEs are much lower than 100% [42, 43, 44]. In Figure 6.8b, the performance of a $\text{TiO}_2/\text{PbS}_x\text{Se}_{1-x}$ QD heterojunction solar cell under 3.35 mW/cm^2 447 nm laser illumination is shown with an energy conversion efficiency of 5.65%.

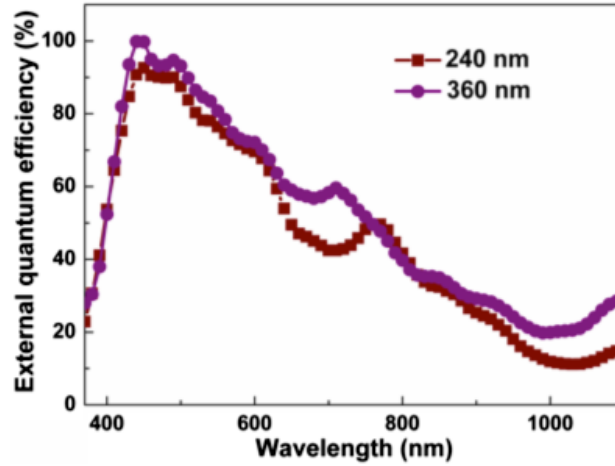


Figure 6.7: Dependence of EQE on $\text{PbS}_x\text{Se}_{1-x}$ QD film thickness. Typical EQE curves for heterojunction solar cells with 240 ± 20 nm (circles) and 360 ± 30 nm (squares) thick $\text{PbS}_x\text{Se}_{1-x}$ QD films, respectively.

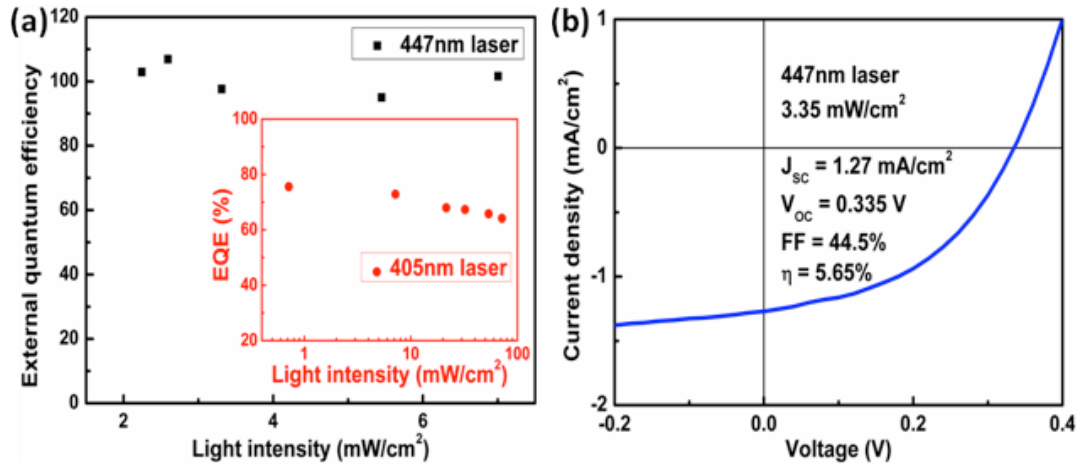


Figure 6.8: (a) External quantum efficiency (EQE) of corresponding $\text{PbS}_x\text{Se}_{1-x}$ heterojunction device at different intensities of 447 nm laser light. Inset: external quantum efficiency (EQE) of the same device at different intensities of 405 nm laser light. (b) Current-density-voltage (JV) characteristics of a $\text{PbS}_x\text{Se}_{1-x}$ QD heterojunction solar cell under 3.35 mW cm^{-2} 447 nm laser illumination.

While our devices show high J_{sc} and V_{oc} , the performance is still limited by

lower fill factor. As shown in Figure 5, shunt resistance (estimated by the reciprocal of the slope of J-V curve at short-circuit) is reduced significantly when the cell is illuminated compared to that in the dark. This so-called photoshunt effect, similar for the ZnO/PbSe QD devices [42], is one of the reasons for the low fill factor. Moreover, the crossing of J-V curves under illumination and in the dark is observed under forward bias in our devices, which is also thought to limit fill factor and device performance [42, 45]. It is recently reported that hydrazine + EDT treatment can eliminate the crossover [15]. If hydrazine was used as ligand together with EDT in ternary QD devices further improvement in fill factor, EQE and energy conversion efficiency of $\text{PbS}_x\text{Se}_{1-x}$ QD devices might be expected. In all, we believe that there is still much room for further improvement in device performance by changing device fabrication process and optimizing device structure parameters to increase shunt resistance.

6.4 Conclusion

In conclusion, we have fabricated heterojunction solar cells employing ternary $\text{PbS}_x\text{Se}_{1-x}$ QDs and transparent TiO_2 layer. These devices show both high photocurrent and high open circuit voltage, which has proven a challenge for quantum dot solar cell devices. The best devices achieve the efficiency of up to 4.25%, showing great potential of ternary QDs in the application of QD photovoltaic devices. In addition, EQE exceeding 100% at 2.7x the bandgap energy are achieved in these ternary QD heterojunction devices with EDT treatment, providing evidence for the existence of MEG-like effects

in $\text{PbS}_x\text{Se}_{1-x}$ QDs.

6.4.1 Acknowledgements

The authors of the manuscript would like thank Dr. Campbell Scott in IBM Almaden research center and Dr. Sanjay Tiwari in UCSC for help in measuring optical parameters of TiO_2 . We acknowledge support through the DOE SETP program (DOE DE-FG36-08GO18104) and the NSF Solar program (NSF DMR 1035478). G. Z. acknowledges support of China Scholarship Council.

Chapter 7

PbS Graded Bandgap Solar Cells

7.1 Introduction

As mentioned in Chapter 5, Pb-chalcogenide based devices are potential multi-junction candidates since their first exciton peaks can span the visible to IR range, increasing absorption and generation. Recently, PbS and PbSe QD solar cells have achieved photocurrents up to 24 mA cm^{-2} [15], which is comparable to photocurrents [46] achieved with a Si NC absorber layer. However, these currents are still low compared to bulk crystalline materials. Additionally, the QD PV sector has been unable to reach high efficiencies, primarily due to this combination of low currents and low photovoltages, which can be attributed to low electron mobilities [47] resulting in short diffusion lengths [48] leading to a trade off between absorption and extraction in our absorbers. Complicating this further, the V_{oc} is generally understood to be limited by non-radiative recombination processes associated with Fermi level pinning in the

mid-gap [34] due to surface defect states on the QD [49]. This leads to the limit $V_{oc} \leq .5E_g$.

Of all QD-based solar cells (QDSC), PbS QDSCs have the highest efficiencies and best open circuit voltages, though they are still limited to $V_{oc}=.5E_g$. We saw in the previous chapter that V_{oc} does not vary with absorber layer thickness, so perhaps a route to higher performance should focus on enhancing the V_{oc} through absorber layer engineering. Recently, Yoon et al [50] published on the highest V_{oc} achieved thus far, 0.69V, using a Schottky type device structure. They find that their V_{oc} has an empirical limit of $V_{oc}(\text{mV}) = .553E_g/q-59$ [50], which is higher than $.5E_g$ due to increased QD passivation. These recent advances show that increasing V_{oc} is possibly via a number of paths. To that end, this chapter deals with using bandgap engineering to increase the V_{oc} .

The spectral response tailoring enabled by the colloidal QD solution is a potential pathway to higher efficiencies by extending absorption to both the IR and visible regions. Here, single-junction ultra thin-film (~ 200 nm) TiO_2 -PbS photovoltaics (PV) with a graded PbS absorber layer have been investigated and show interesting device performance. Normal, reverse, and notch (double) type grading structures are studied while the bandgap is varied over 2 or 3 different bandgaps, ranging from 1.65 eV to 0.98 eV.

These grading structures are used often in more traditional solar cells to produce a variety of beneficial effects, such as back surface fields in crystalline PV [51, 52] and in organics to produce blocking or transport layers [53, 54]. It can be even more

useful in our case, as the confinement primarily affects the conduction band due to a combination of strongly varying electron affinities compared to the ionization potential [55] and relatively flat valence bands due to the (mostly) uniformly doped p-type PbS. This means that once generated and separated, the electrons will have an additional driving force for extraction. Recent work by Sargent [56] takes advantage of this additional force, but they do not vary the initial PbS layer.

7.2 Experimental Methods

PbS nanocrystals were synthesized and provided by Solexant, TiO₂ nanoparticle solutions were purchased from Solaronix. The synthesis results in quasi-spherical nanocrystals ranging in bandgaps from approximately 0.98 eV to 1.65 eV. The nanocrystals are capped with oleic acid during the synthesis, then the NCs were washed and redissolved into a mixture of 8.5:1 hexane:chloroform to concentrations of 20-50 mg/mL. The first excitonic peaks and resultant bandgaps for the range of NCs explored in this study are given in Table 7.1.

1st exciton peak[nm]	Bandgap [ev]
763	1.65
820	1.51
875	1.42
945	1.31
1003	1.24
1260	0.98

Table 7.1: First excitonic peaks and resultant bandgaps of PbS QDs used in gradation experiments.

Colloidal QDs provide an especially simple way of investigating graded structures, since the inks can just be deposited one after the other in the typical layer by layer fashion. Our graded absorbing layer is accomplished via spin-casting colloidal solution PbS quantum dots (QDs) onto a glass/ITO/TiO₂ substrate and performing ligand exchange with 5mM EDT in acetonitrile after each spin step to remove the oleic acid and cap the QDs with the shorter, more conductive EDT ligand. The absorber layer is built up in the same way as in Chapter 6, to an final absorber thickness of approximately 200 nm. Finally, 100 nm of Au is deposited as the back contact under vacuum in an oxygen-free thermal evaporator.

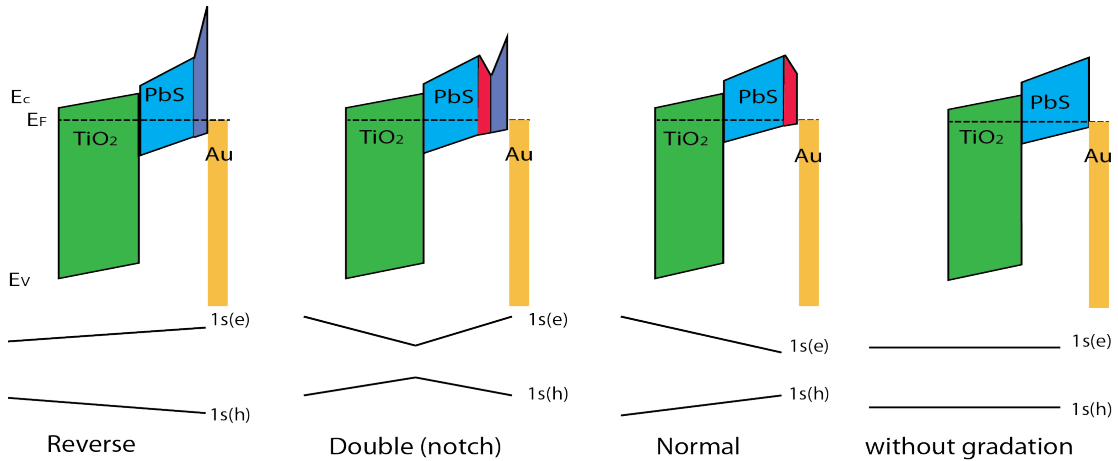


Figure 7.1: Energy-band distance diagrams of the types of bandgap gradings used in this study are shown (top), along with the expected band edge shifts (bottom). For all devices made with only two different sized QDs, the normal grading structure is used.

Figure 7.1 shows both the energy-band distance diagrams of the types of bandgap gradings used in this study (top), along with the expected band edge shifts (bottom). Note, these band shifts are not to scale but are exaggerated and shown here

for illustrative purposes. Figure 7.2 shows a cartoon schematic of the device structure used in these studies, with the blue and purple spheres each representing different sized PbS nanocrystals. For all devices made with only two different sized QDs, the normal grading structure is used.

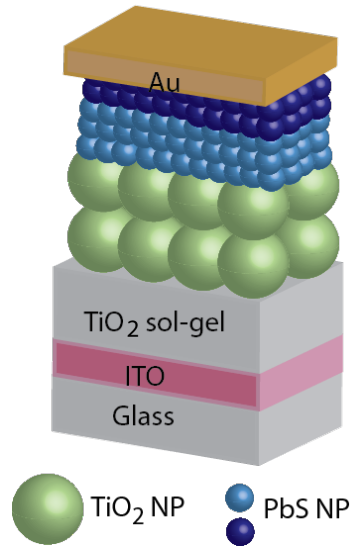


Figure 7.2: Cartoon schematic of device structure used in PbS graded bandgap studies. Blue and purple spheres represent different sized PbS nanocrystals.

7.3 Results

First, we present our baseline devices comprised of one size only. Figure 7.3 shows the JV characteristics of devices as a function of decreasing bandgap. Focusing on J_{sc} and V_{oc} , we see that the best overall performer is the 1003 nm QD, giving $J_{sc} = 17.0 \text{ mA cm}^{-2}$. With a bandgap of 1.2 eV and the a maximum theoretical V_{oc} of $.5E_g$,

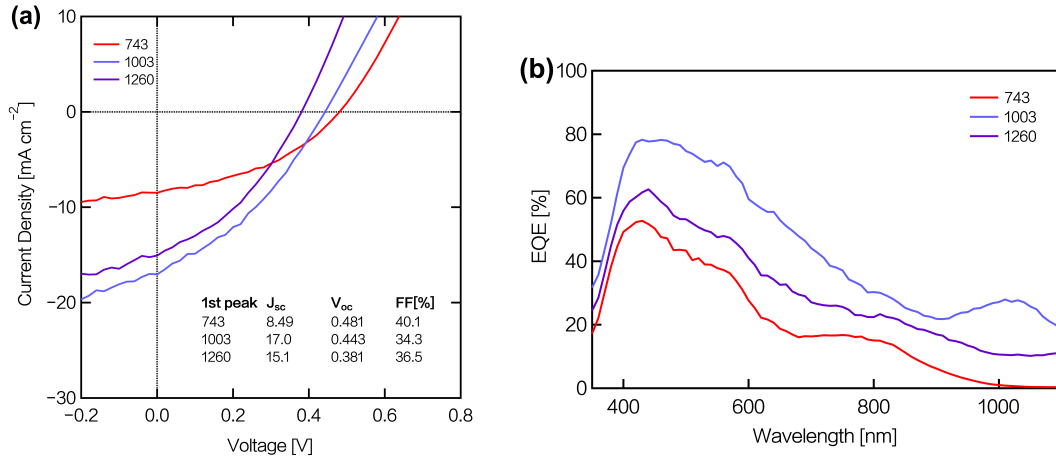


Figure 7.3: Monosize studies, showing size dependence of PbS QD solar cells, for comparison to the graded studies shown above. (a) JV characteristics of devices made with PbS QDs ranging from 763 nm-1260 nm. (b) EQE spectral response for the same devices shown in (a).

our V_{oc} of 481 mV is still about 27% below the expected 600 mV. The EQE spectra has a maximum of 80% near 400 nm. Exciton peaks line up with absorbance spectra measurements (Figure 3.1b), with the 1.2 eV QDs clearly showing a higher response across all wavelengths, as expected from the JV characteristics.

7.3.1 Two-sized Studies: Normal Gradation

Comparing the graded structures to our baseline devices allows us to quantify the improvement, if any, that these graded structures lead to. Figure 7.4a shows the JV characteristics of devices made with two differently sized dots, arranged in a normal gradation. The blue curves correspond to devices made starting with an initial layer of 763 nm QDs forming the junction with TiO_2 , while the red/pink curves correspond to devices starting with 820 nm. The gradation is accomplished by then depositing 1003

nm or 1260 nm QDs adjacent to the starting layer, allowing us to locate which layer in the junction contributes, if any, the largest increases in performance.

The results of the two-sized studies indicate that the primary controlling factor for increasing the open circuit voltage depends on the bandgap of the layer immediately next to the TiO₂ window layer. That is, the only limiting factor to photovoltage boosts is the layer closest to the light incident interface. Of course, this is how multi-junction solar cells are designed, so this is no big breakthrough. Our best performing device features an absorber layer comprised of 763 nm and 1003 nm QDs, leading to an open-circuit voltage of 589 mV. This represents an increase of over 100 mV from the best performing monosized PbS device, however, this also leads to much lower photocurrents. Due to the fundamental tradeoff between J_{sc} and V_{oc} , though we have succeeded in >100

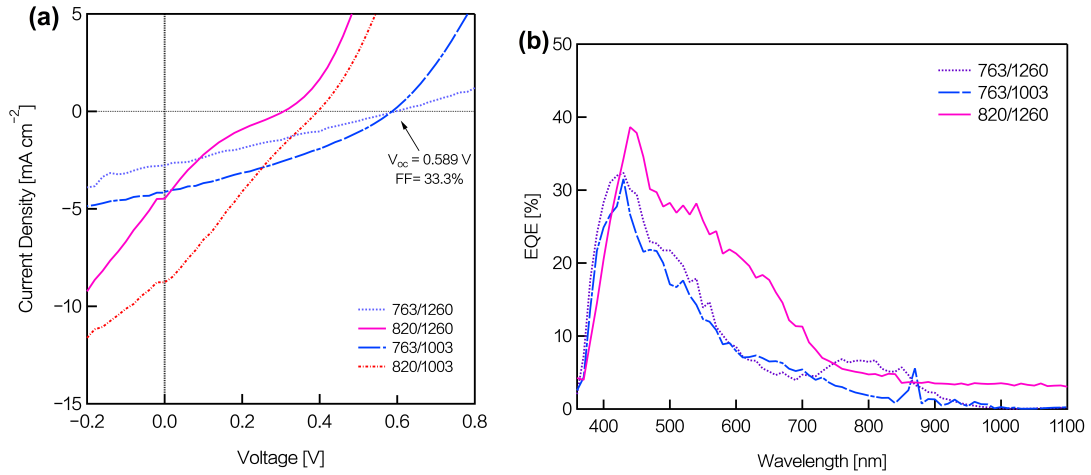


Figure 7.4: JV curves and EQE response for the two-sized normal gradation studies. (a) the JV spectra indicate that devices formed with 763 nm QDs closest to the light incident surface achieve the largest V_{oc} boosts. (b) EQE spectra for 2 sized studies, showing that the gradation involving 820/1260 has a higher spectral response, agreeing with J_{sc} for that device in Figure 7.3 above.

mV increases in V_{oc} , the J_{sc} is reduced in all devices utilizing a normal gradation.

The fill factors for graded structures, regardless of initial PbS layer, all decrease by over 10%, indicating that recombination becomes a much larger issue for these types of absorber gradations. This can be attributed to introduction of poor size dispersity leading to a disruption in the QD matrix formed after ligand exchange. Lower mobilities have been seen in PbS QD films where good size control is not achieved, and is [48] attributed to a disruption of carrier hopping sites leading to decreased mobilities. It is also likely a result of increased interfacial recombination due to the introduction of another PbS layer.

Interestingly, we also find that even if we use QDs whose bandgaps differ by even ~ 60 meV, these voltage boosts are lost. The JV curves for both devices made with 820 nm QDs show a steep decrease in V_{oc} , with a best open circuit voltage of 380 mV, performing even worse than the single-sized devices. This indicates that recombination is occurring at a higher rate in devices fabricated with 820 nm QDs, possibly due to increased disruption of the QD lattice using that specific size or possibly more efficient interfacial recombination. These devices do, however, exhibit higher short-circuit currents, which is expected, and corroborated by their EQE response seen in Figure 7.4b.

7.3.2 Three-sized Studies: Gradation-specific Enhancements

Now we investigate just how the specific gradation type can affect the photovoltage. The normal and double gradation devices for this study start with 763 nm QDs

as the layer closest to the light-incident interface, while the reversed gradation device flips this around to start with the smallest bandgap QD, 1260 nm. The intermediate size used for all three gradation types is 1003 nm.

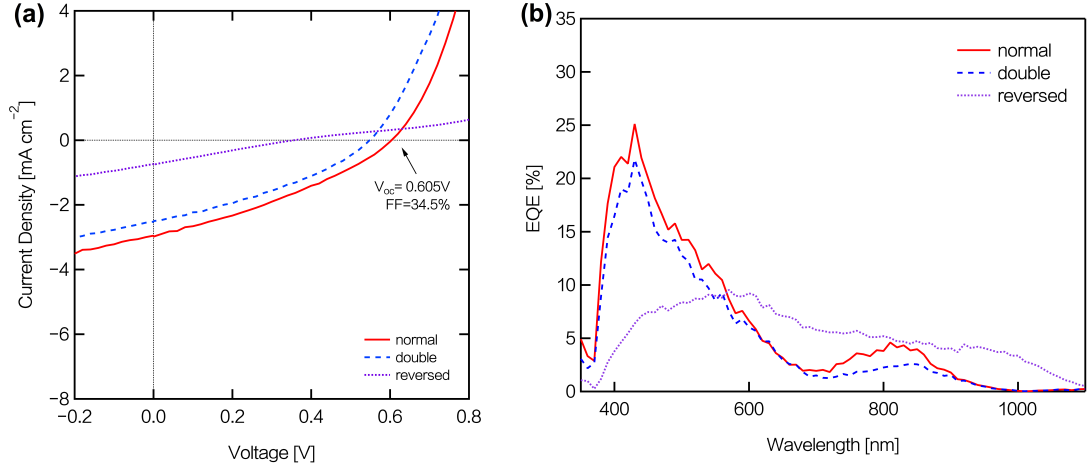


Figure 7.5: EQE spectra for 2 and 3-sized gradation experiments. (a) For 3-gap experiments, normal and double gradations give similar JV characteristics, with the largest V_{oc} boost achieved through the use of normal gradation.(b) The normal and double stacks have similar EQE response, while the reversed has much lower response in blue wavelengths.

Figure 7.5 shows the JV characteristics of each type of gradation fabricated. As seen in the previous study, normal gradation provides the best performance for these devices, though the double structure is not far behind. The V_{oc} boost achieved here is just over 120 mV. This is an even larger increase than we have seen with the two-sized normal gradation, yielding a V_{oc} of 606 mV. Compared to our device fabricated with just 763 nm QDs, this normal graded device produces over 75% of the expected V_{oc} , while the single-sized device yields 72%. This is indicative that there is indeed additional driving force aiding the extraction of the minority-limited electrons.

The clear lowest performer is the reversed structure, which features the smallest bandgap (1260 nm) at the light incident interface. There are two effects at work leading to the decreased performance. First, the main loss is in photovoltage and can be simply explained from the reduction of available bandgap. Secondly, there is also a marked reduction in photocurrent. The EQE spectrum in Figure 7.5b shields additional light on this, showing a large decrease in response in the blue wavelength region. We attribute this decrease to the shorter penetration depth of blue photons, leading to a lower collection rate for the reversed type structure as the layers after 1260 nm do not contribute. These reversed type structures may also lead to the creation of a recombination zone near the back contact. Additionally, since excitons in QD films tend to have low diffusion lengths, the added graded layers behind this initial 1260 nm layer instead present an even larger barrier to extraction as the carriers have to travel farther to escape.

7.4 Conclusion

We have achieved device performance improvement by bandgap grading using up to three different PbS QD sizes with normal, double, and reversed gradations over the absorber layer. The best device employs a three-sized normal gradation, giving $V_{oc} = 0.605$ V, which is an enhancement of over 0.2 V compared to monosized devices utilizing the same sized PbS QD/TiO₂ junction. We find V_{oc} is increased with higher bandgap materials at the light incident interface; however, for all devices, both J_{sc} and

FF decreases. The results show that devices with normal gradation have the potential for the most improvement of V_{oc} for PbS QD solar cells and demonstrates an upscaleable, simple pathway towards improving V_{oc} and FF for QD solar cells. If finer synthesis control was possible, we see no reason why this gradation could be done more gradually to potentially give larger increases while also retarding the J_{sc} decrease.

Part III

Group IV QDSC

Chapter 8

Introduction

In Part II we saw that Pb-chalcogenide nanocrystals are robust materials that offer a clear pathway towards disrupting the solar landscape through third-generation principles. They are an intense subject of research and are still the only system to exhibit MEG in an actual device [15]. We have shown two potential routes to increase their photovoltaic performance: (1) increasing the available photocurrent through MEG-like increases in the EQE, and (2) increasing the photovoltages through bandgap engineering.

Despite the interesting and positive research results with PbX nanomaterials, there are some drawbacks to this system. First and foremost, the heavy metal cation used in all of these materials, Pb, is toxic to the cardiovascular, nervous, and reproductive systems of humans and has been restricted (along with tellurium) in the European Union. It is especially toxic to children as it can cause behavioral changes and interfere with the development of the nervous system. Additionally, it accumulates in the environment, causing potential for increased uptake in humans and animals. Secondly, the

Element	% Weight
Si	27.7
Al	8.1
P	0.1
S	0.05
Zn	0.01
Cu	0.007
Ga	0.002
Ge	0.0007
As	0.0005
Sb	0.0001
Cd	0.00002
In	0.00001
Se	0.000009
Te	0.0000002

Table 8.1: Abundance of elements relevant to solar cell manufacturing, by percent weight found in Earth’s crust.

chalcogens are not particularly Earth abundant, save for sulfur, as seen in Table 8.1.

It is mainly for these two reasons that researchers are now looking towards other QD systems. Naturally, there is large interest in exploring a nanomaterial system comprised of the archetypal semiconductors from Group IV, germanium and silicon, who happen to be much safer than lead, relatively Earth abundant, as seen in Table 8.1, and for whom we already have a large body of knowledge and industrial know-how.

Since the early 1990s, Si has been researched as a potential game-changing nanomaterial with a large amount of research being focused towards it. Recently, MEG was even observed in Si NCs and nanorods with a considerably higher efficiency compared to bulk Si, showing a turn on at $2.4 \pm 0.1E_g$ with a quantum yield of 2.6 ± 0.2 excitons per absorbed photon at $3.4E_g$ [57]. This is the first report of MEG in

indirect-gap semiconductors, further increasing interest in Group IV nanomaterials¹.

However, Ge, which is often overlooked in favor of Si, may in fact be a better third-generation materials candidate for a few reasons.

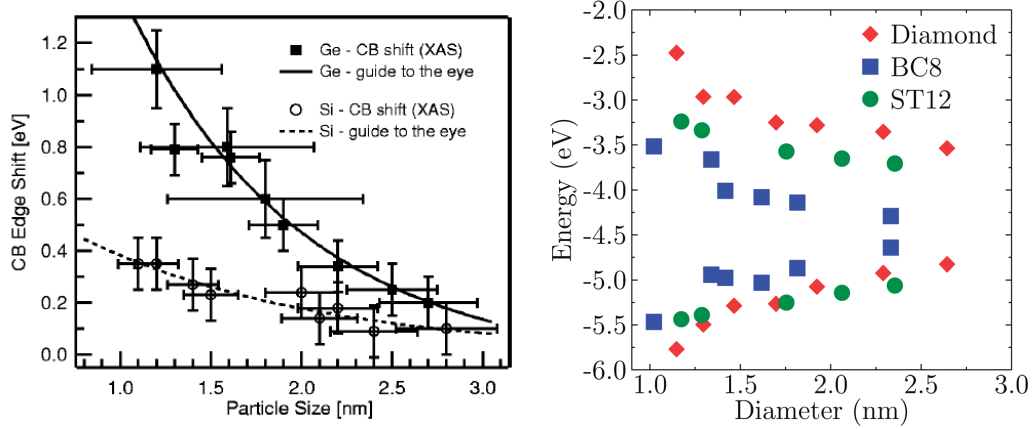


Figure 8.1: left: Experimentally determined CB shifts for Ge and Si as a function of decreasing radii shows the much larger response in Ge. This is attributed to the much larger exciton Bohr radius, enabling Ge to remain in the strong confinement regime for all sizes shown. Conversely, the Bohr radius for Si is much smaller at $\sim 4\text{nm}$, meaning they are not experiencing as much confinement over the range shown. Adapted from [59]. Right: HOMO and LUMO shifts for different phases of Ge, from theoretical predictions. Adapted from [60].

First, Ge has a much larger exciton Bohr radius (24 nm versus 4.9 nm for Si), placing all but the smallest Si NCs out of the strong confinement regime. Typically, it is more difficult to synthesize very small NCs with good crystallinity [61]², which has been seen in Ge NCs. Another consequence of Ge’s larger Bohr radius is that it should experience much stronger confinement resulting in large effects upon quantum

¹Though MEG has not yet been observed in Ge NCs, impact ionization was observed in bulk Ge (in addition to other systems that now exhibit MEG), so it is not unreasonable to expect it [58].

²They tend to be more amorphous with less crystal ordering.

confinement. Theoretical and experimental work suggests that Ge's bandgap is very sensitive to crystallite size reduction; Figure 8.1a shows the results of one such study indicating the Ge CB shift is larger at all NC sizes.

Although the bulk bandgap of Ge at 0.67 eV (Figure 8.2) is too narrow for use as a single-junction photovoltaic, Ge has been used in tandem cells and other thin-film PV. Considering the large confinement effects seen in Figure 8.1a, Ge NCs should easily be able to reach bandgaps of 0.8 eV, the energy for optimal MEG enhancement. Indeed, recent theoretical predictions indicate the HOMO-LUMO gap almost doubles as the NC goes from 3.0 nm to 1.0 nm (Figure 8.1b). Conversely, Si with a bulk bandgap of 1.1 eV will be shifted even further away from the optimal energy. This also makes Ge a better candidate for multi-junction photovoltaics.

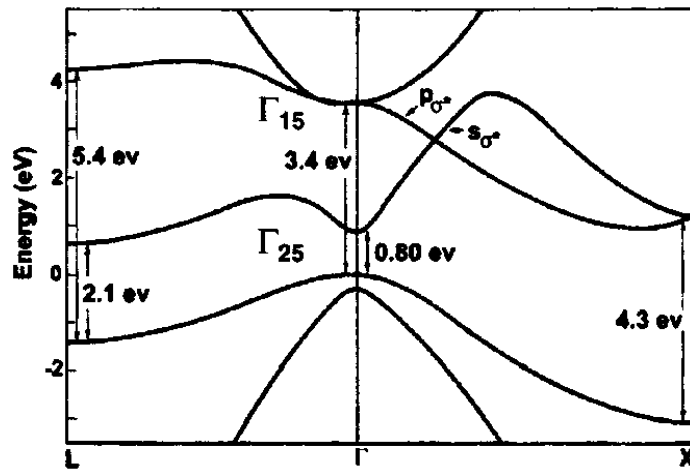


Figure 8.2: Energy-band diagram of bulk Ge. Adapted from [62].

Finally, though they are both indirect gap materials, Ge is a better absorber due to the strong direct gap at 0.8 eV (Figure 8.2). This, coupled with the focusing of oscillator strength under confinement, leads to Ge NCs having a much stronger absorption coefficient than Si NCs.

8.1 Ge NC synthesis

Unfortunately, colloidal syntheses of Group IV nanocrystals are much harder than II-VI CQD syntheses, primarily due to the covalent bonding nature of Si and Ge. This requires strong reducing agents along with high temperature syntheses to achieve nanocrystal formation but typically results in low yields. The initial synthetic route pursued for the Ge NCs used in these studies relied on conventional Schlenk line hot injection methods, similar to those used in the II-VI and IV-VI NC systems, where nucleation begins when heated solvent-precursor mixtures are injected with appropriate reagents, and ligands and temperature ramping controls crystallite size. This method uses germanium iodides (GeI_2 and GeI_4) with oleic acid (OA) as the capping ligand, but poor size control and growth kinematics lead them to abandon that route. When capped with oleic acid, Ge CQD ink was incapable of being ligand exchanged using the same methods that worked with Pb-chalcogenide systems. It is thought that the oxygen from OA binds with Ge to create an energetically stable oxide, resulting in the inability to perform the typical ligand exchange with thiols. Table 8.2 shows the diatomic bond energies [63]:

Table 8.2: Diatomic Bond Energies for Ge-*x* compounds.

bond	D_{298}^0 [$\frac{kJ}{mol}$]
Ge-C	460 ± 21
N-Ge	257
Ge-H	≤ 321.8
Ge-S	551 ± 5
Ge-O	658.1

As seen in the above table, the ligand exchange solutions on which we relied for the Pb chalcogenides won't work; they are simply not energetically favorable in this case.

Fortunately, Muthuswamy et al [61] came up with a new synthetic route utilizing oleylamine (OAm) as the solvent and capping ligand for reactions using a microwave-assisted heating route. This facile synthesis uses the same GeI_2 and GeI_4 precursors and heat ramp up time to control QD size, but is able to achieve higher yields and narrow size distributions due to enhanced reaction rates and more uniform heating. Additionally, the Ge NCs produced in this way achieve higher crystallinity at lower temperatures, leading to more reproducible reactions.

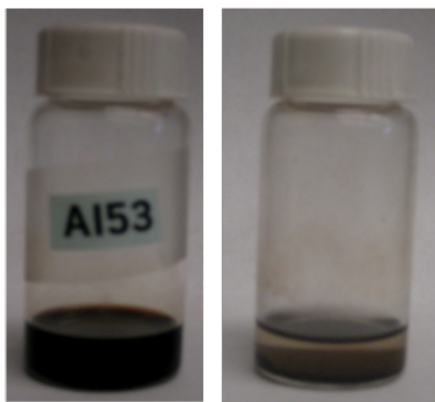


Figure 8.3: A sample of the Ge QD ink used in these studies. Left: stable dispersion. Right: Precipitated QDs.

Chapter 9

Ge QD Photoconductors

Spun cast TiO₂-Ge quantum dot (QD) heterojunction type photodetectors have been fabricated and characterized, with interest paid to photocurrent enhancements related to device design. Performance as a function of absorber layer thickness, QD size, and back contact is investigated. We have achieved ultra-thin (~ 200 nm) devices with photocurrents at 0.5 V of 10^{-4} A cm⁻² while the thickest devices have photocurrents at 0.5 V of 10^{-2} A cm⁻² with on-off ratios > 100 , which represents 5 orders of magnitude increase in photocurrents over previously fabricated Ge QD devices. At 0.5 V bias, the currents in our devices are competitive with thin-film Ge photo-voltaics. The majority of this material was published in 2013 in the *Applied Physics Letters* [64].

9.1 Introduction

Group IV semiconductors have long been used in photodetectors, photovoltaics (PV), sensors, and light-emitting diodes [65, 66], but recently, group IV colloidal quantum dots (CQD) have garnered increased interest in the optoelectronics field due to their lower toxicity compared to lead- and cadmium-containing colloidal QD systems, low-cost solution processability, desirable ability to tune electrical properties, increased response in the IR region, and potential for higher conversion efficiencies in PV devices due to Multiple Exciton Generation (MEG) [26, 23, 31, ?, 24, 15]. Specifically, Germanium (Ge) QDs have drawn interest due to their narrow bulk bandgap which can be readily tuned by quantization to the optimal energies for both maximum power conversion efficiencies (η) and MEG enhancements to η [67], and their large exciton Bohr radius which should provide the necessary quantum confinement effects [68, 59].

So far, however, unary group IV QD systems have not been widely studied, mainly due to difficult colloidal syntheses compared to the easier binary IV CQD syntheses. Recently, unary IV solution syntheses have begun to catch up with II-VI and IV-VI syntheses, enabling groups to begin studying Ge CQD optoelectronic properties.

Holman et al. have focused on Ge QD field-effect transistors fabricated via drop casting onto Si wafers, while Xue et al. focus on hybrid Ge nanoparticle (NP)-polymer blend photodetectors fabricated via drop casting Ge NP-P3HT ink blend [69, 70]. Although the hybrid photodetectors show good responsivity with photocurrents on the order of 10^{-9} A cm^{-2} , it is unclear what role the polymer is playing. To improve

and isolate Ge performance, we turn to fabricating heterojunction type devices, which have been studied in depth for II-VI and IV-VI CQD systems and are so far the only QD device type to show the MEG effect [24, 15].

Here, we report on the fabrication and characterization of photoconductive spun-cast heterojunction devices with a window layer of TiO_2 and Ge QDs as the active layer. Our treated films are not insulating and require no anneal, potentially lowering future production costs. We focus on performance improvements achieved through variations in absorber layer thickness, QD size, and back contact. Our best devices show improvement in photocurrents by 5 orders of magnitude over previous Ge QD devices, [70] and have photocurrents at 0.5 V comparable to Ge thin-film photovoltaics.[71] This work demonstrates that Ge QD heterojunction devices are a promising system for future photoelectric devices with ample room for improvement and optimization, while these devices represent a pathway to cheaper, more accessible photovoltaics.

9.2 Experimental Methods

Titanium (IV) ethoxide (technical grade) and anhydrous solvents (hydrazine and pyridine) were purchased from Sigma-Aldrich and used as received. 1,2-ethanedithiol (EDT, purum 98.0%) and TiO_2 nanoparticle paste were acquired from Fluka, and Solaronix, respectively.

A transmission electron microscope (TEM) image of the 4.3 ± 1.0 nm Ge QDs used, a cross-sectional high-resolution scanning electron microscope (HR-SEM) image

of the device stack, along with a cartoon of the device structure and energy band diagrams of our devices are shown in Figure 9.1. Standard air-free techniques were used throughout synthesis and purification process. The colloidal Ge QDs were synthesized at UC Davis using a microwave-assisted heating route prescribed via literature [61].

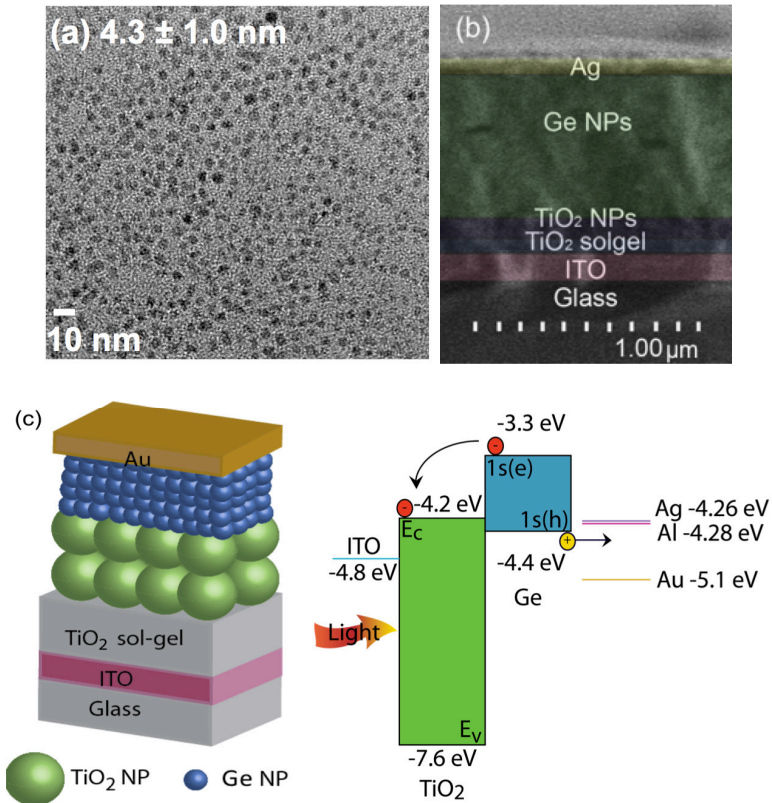


Figure 9.1: (a) TEM image of the 4.3 ± 1.0 nm Ge QDs used to fabricate devices. (b) (Color online) HRSEM cross-sectional image of device stack. (c) Cartoon of device structure with energy band diagrams of the TiO_2 -Ge heterojunction type devices studied in this paper.

This microwave-assisted synthesis produces quasi-spherical Ge NCs with good size control. Samples of 3 narrow size distributions were prepared for this work. Each

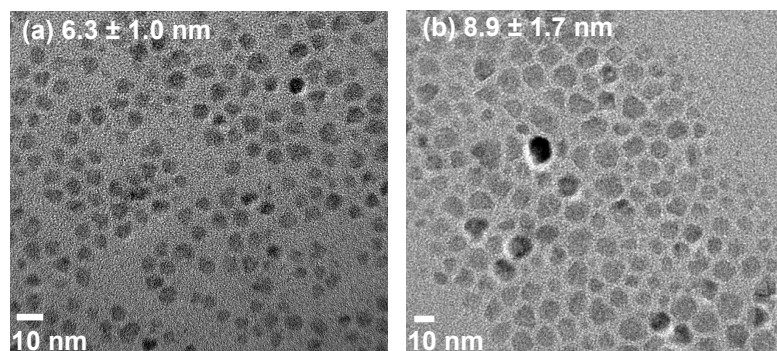


Figure 9.2: (a, b) TEM images of the 6.3 ± 1.0 nm and 8.9 ± 1.7 nm QDs used in this study show quasi-spherical nanocrystals with $< 25\%$ monodispersity.

size set has less than 25% dispersity.

Figure 9.2 shows transmission electron microscope (TEM) images of the two largest sized Ge QDs (6.3 ± 1.0 nm and 8.9 ± 1.7 nm) synthesized via this method and employed in this paper. The as-synthesized NPs are then washed in methanol, isolated, and finally dispersed in toluene or hexane to final concentrations ranging between approximately $10\text{-}30$ mg mL⁻¹. FTIR spectra (Figure 9.3) of the final Ge solution show absorption peaks consistent with oleylamine, indicating the presence of oleylamine on the surface.

9.2.1 Device Fabrication

TiO₂ sol-gel was prepared using titanium-ethoxide as precursor by the standard procedure described previously [19]. Both TiO₂ sol-gel and nanoparticle pastes were spin-coated onto a cleaned 1" x 1" glass substrate with pre-patterned Indium Tin Oxide

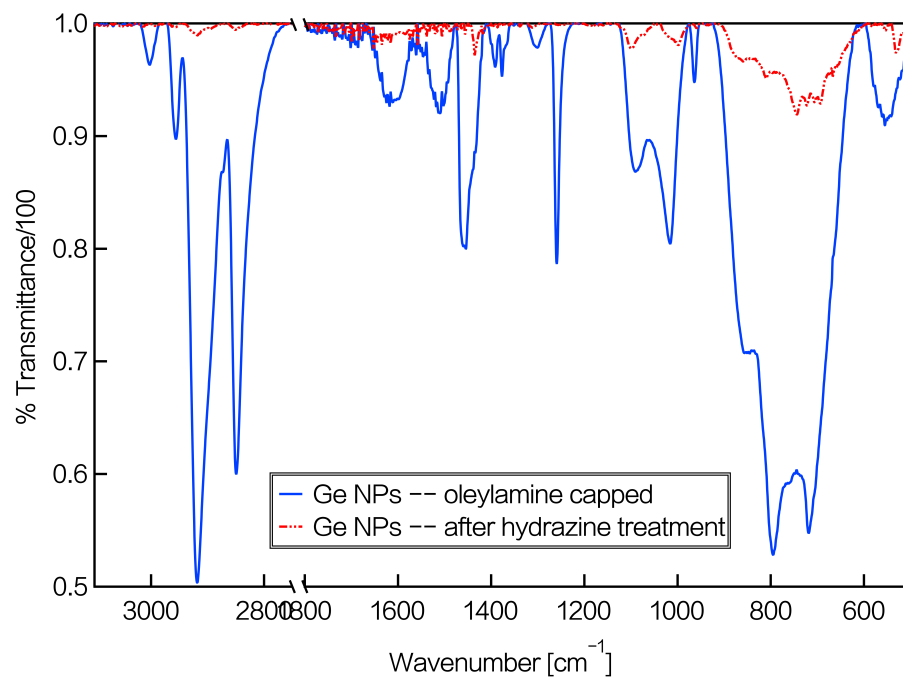


Figure 9.3: Baseline-corrected FTIR spectra of Ge NPs capped with oleylamine compared to Ge NPs after hydrazine treatment. The pre-hydrazine treated spectra show a number of signature peaks, indicating the presence of oleylamine on the surface of the Ge NP. Post-hydrazine treated spectra show complete removal of the bands corresponding to C-H symmetric and anti-symmetric stretching.

(ITO) electrodes of 150 nm thickness (Thin Film Devices, Anaheim) sequentially. Figure S3 shows the ITO pattern (blue) with an overlay of our back contact mask (black) for each substrate. Each TiO_2 layer, $\sim 75\text{-}100$ nm (sol-gel) and $\sim 150\text{-}200$ nm (NP), was sintered at 450°C for 30 minutes in air after deposition to improve conductivity. The Ge QD film was then deposited onto the TiO_2 film in a layer-by-layer deposition by spin-coating $8\ \mu\text{L}$ of QD ink in a nitrogen-filled glove box followed by immersing the substrate into a 1M solution of hydrazine, pyridine, or 1,2-ethanedithiol (EDT) in acetonitrile for ~ 15 seconds to facilitate film formation and increase electronic coupling

between the QDs. The thickness of the QD film is controlled by spin speeds (held constant at 4000rpm here), number of cycles, and concentration of the QD ink. For QD inks with approximately 30 mg mL^{-1} , each resultant layer is approximately 100-150 nm. Lastly, 100 nm of silver, gold, or aluminum contact was thermally evaporated under high vacuum (10^{-5} - 10^{-6} Torr) at a rate of 0.7 \AA s^{-1} ; the area of each device formed is 0.03 cm^2 .

For film formation characterization, the substrate is immersed in a 1M solution of hydrazine, pyridine, or 1,2-ethanedithiol (EDT) in acetonitrile. For all devices in the performance vs. thickness, QD size, and back contact studies, hydrazine treatment is performed after each spin cycle, following the usual layer-by-layer deposition technique.

Current density-voltage (J-V) curves were taken using a calibrated Oriel solar simulator and a Keithley 2400 source meter. UV-Vis-NIR spectra of diluted Ge NP dispersions and films at room temperature were taken using a Perkin Elmer Lambda 750 spectrophotometer and a Stellar Net spectrometer (Thin Film Measurement System), respectively. TEM was performed using a Schottky emitter JEOL2500SE electron microscope operating at a voltage of 200 kV. The images were captured with Digital Micrograph software provided by Gatan Inc. Samples for TEM analysis were prepared by placing a drop of a dilute Ge nanoparticle dispersion in toluene or hexane on the carbon coated 200 mesh/400 mesh Cu grids obtained from SPI. FTIR spectra were recorded using a Bruker Alpha spectrophotometer; sample preparation information can be found in Supplemental Information. The topography and thickness of Ge QD films were obtained via an atomic force microscope (AFM) operating in tapping mode. A

Hitachi S-4800 II field emission scanning electron microscope (SEM) operating at 3 kV was employed to observe the cross section of devices and confirm the thickness of each layer; these measurements were carried out in air. All device characterizations, unless otherwise stated, were carried out in a nitrogen-filled glove box at an oxygen concentration below 50 ppm.

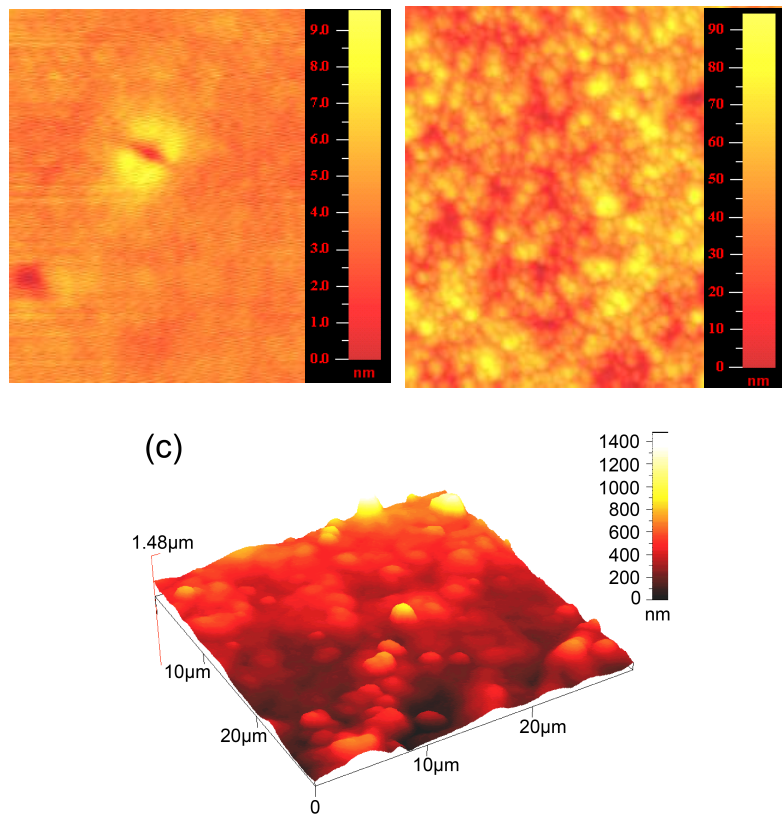


Figure 9.4: AFM images showing TiO_2 film morphology and film thickness for (a) sol-gel and (b) nanoparticle layers. Adapted from [24]. (c) Non-contact mode AFM image showing morphology of typical Ge QD film on quartz images of TiO_2 .

9.3 Results

As received, the oleylamine capped NPs are incapable of forming films via multi-layer spin- or dip-coating. Unlike previously studied group IV-VI QD systems, our Ge QDs are also incapable of forming films when exchanged with 1,2-ethanedithiol (EDT) [24], and we found that films fabricated with these oleylamine-capped QDs remain soluble until ligand exchange with a suitable amine is carried out. AFM measurements give a surface RMS roughness of 12 nm for the Ge QD film, indicating a rough, mesoporous layer (Figure 9.4).

Room-temperature absorbance of the colloidal Ge QDs capped with oleylamine in hexane and the absorbance of films formed by hydrazine exchange on a quartz sub-

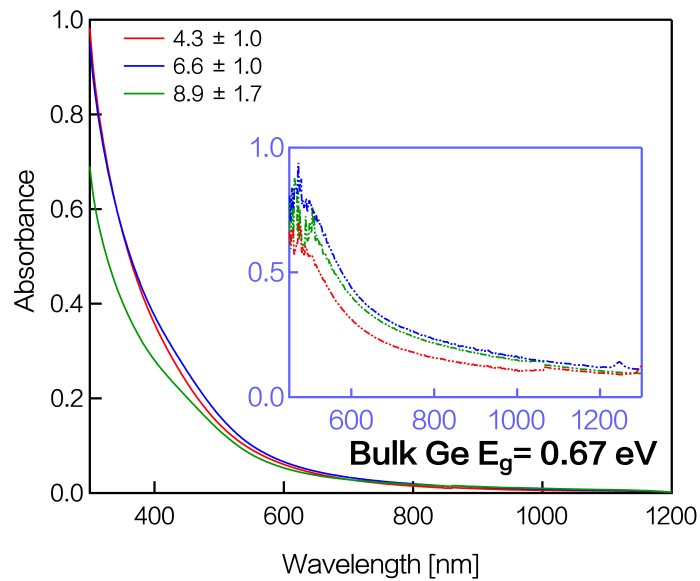


Figure 9.5: Room-temperature UV-Vis spectra of colloidal Ge QDs capped in oleylamine and dispersed in hexane. Inset: room-temperature UV-Vis spectra of films made with different sized QDs on quartz substrates.

strate (Figure 9.5) shows both the pre- and post-hydrazine treated spectra appear identical and have no observable exciton peak, consistent with previous literature reports [72, 73, 74]. FTIR spectra (Figure 9.3) show that hydrazine treatments result in the suppression of both symmetric and anti-symmetric stretching peaks associated with C-H bonds from oleylamine, indicating successful replacement of oleylamine on the surface of the QD with hydrazine, in contrast to recent reports with alloyed Ge NPs [75].

Of EDT, pyridine, and hydrazine, we find that only exchange with hydrazine is suitable for film formation (Figure 9.6). Tauc plots are obtained for both liquids and films, with film fits from a linear regression giving bandgaps ranging from 0.87 eV to 1.15 eV, which are comparable to the values reported by Neale et al. [72] for a similar

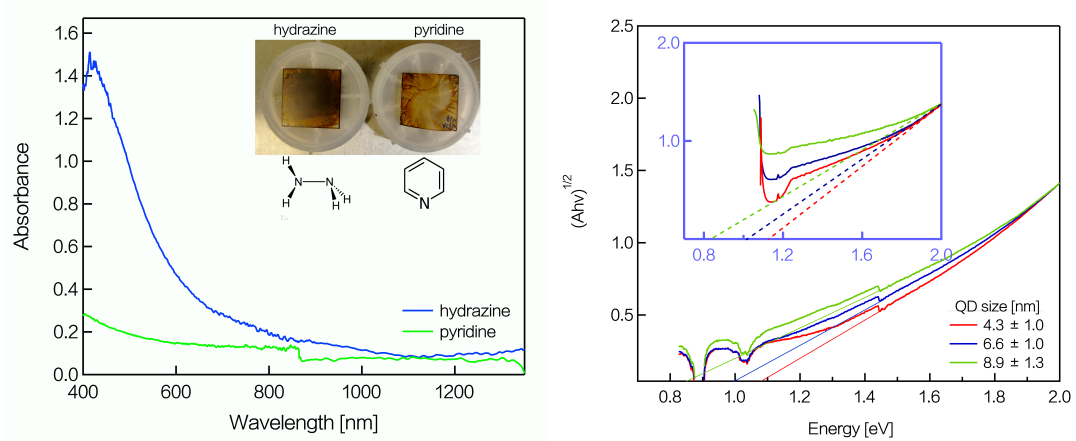


Figure 9.6: (left) room-temperature absorbance of films treated with hydrazine and pyridine on quartz substrates show hydrazine performs well in film building while pyridine does not. Inset, top: films produced with hydrazine on the left and pyridine on the right. Inset, bottom: chemical structures of ligands used in film formation. Pyridine renders the film partially soluble and is unsuitable for device fabrication. (right) Tauc plots obtained via absorption of QDs measured in (a) show bandgaps that approximately agree with those from film measurements shown in the inset with bandgaps of 0.87 eV, 1.05 eV, and 1.15 eV.

size range.

Current density-voltage (J-V) curves were taken in the dark and under calibrated AM1.5G illumination. The topography and thickness of Ge QD films were measured by both HRSEM and an atomic force microscope (AFM). All device characterizations, unless otherwise stated, were carried out in a nitrogen-filled glove box at an oxygen concentration below 50 ppm.

9.3.1 Effect of Absorber Layer Thickness on Device Performance

Initial devices were marred by poor QD film quality. Previous results [40] from similarly structured PbS-TiO₂ devices indicate a rough, mesoporous QD layer could decrease charge transport, which we observed in our early, thin devices. We note that considering the roughness of TiO₂ nanoparticle film (Figure 9.4a and b) and penetration of QDs into the TiO₂ NP film, the actual thickness of Ge QD films may be up to 100 nm less than the measured Ge QD layer thickness. This mesoporous interface between TiO₂ and Ge in our devices should allow for sufficient absorption while also aiding exciton dissociation [24].

As a first step in understanding our devices, we look at thickness versus performance. All devices in the thickness-dependence study employ the largest QDs with diameter of 8.9 ± 1.7 nm. Figure 9.7a shows the J-V curves for devices as a function of increasing active layer thickness, with thickness denoted by the number of spin+hydrazine treatment cycles, N. As a function of thickness, the photocurrents initially decrease, then increase through 1000 nm (N =10), before dropping off again (N > 10) due to the

trade-off between charge extraction (thinner devices) and increased photocurrents due to increased absorption (thicker devices). We attribute smaller photocurrents found in thinner layers to incomplete absorption of photons and shunting due to poor film quality.

Our early device performance was predominantly limited by this shunting. For our thinnest devices, film improvements lead to shunting decreases and performance becomes recombination-limited. For thicker films, film quality remains an issue. The thicker films remain visibly rougher, possibly introducing a larger number of interfacial recombination sites. Figure 9.7b shows the average photocurrents in our devices at a 0.5 V bias and percentage of solar photons absorbed, both as a function of device thickness. Based on absorption from 400-1000 nm, we find our photocurrents are limited mostly by recombination, since films with $N > 10$ (thickness $> 1\mu\text{m}$) absorb almost 80% of all available photons without considering IR absorption. At 0.5 V, the best photocurrents are 13 mA cm^{-2} with on-off ratios of greater than 100.

Assuming ideal diode characteristics and 100% absorption, the photocurrent is simply a function of bandgap.[76] For bandgaps ranging from 0.87 eV to 1.15 eV, the maximum possible photocurrent ranges from $\sim 40\text{ mA cm}^{-2}$ to $\sim 56\text{ mA cm}^{-2}$. 80% absorption over the whole spectrum brings the lower limit down to 32 mA cm^{-2} , which is only a few mA higher than our best devices.

To better understand the response mechanism behind our Ge NPs and confirm improvements over the previously reported hybrid Ge QD photoelectric devices, we tried Schottky-type devices with Ge NPs and various back contacts. All of these devices were

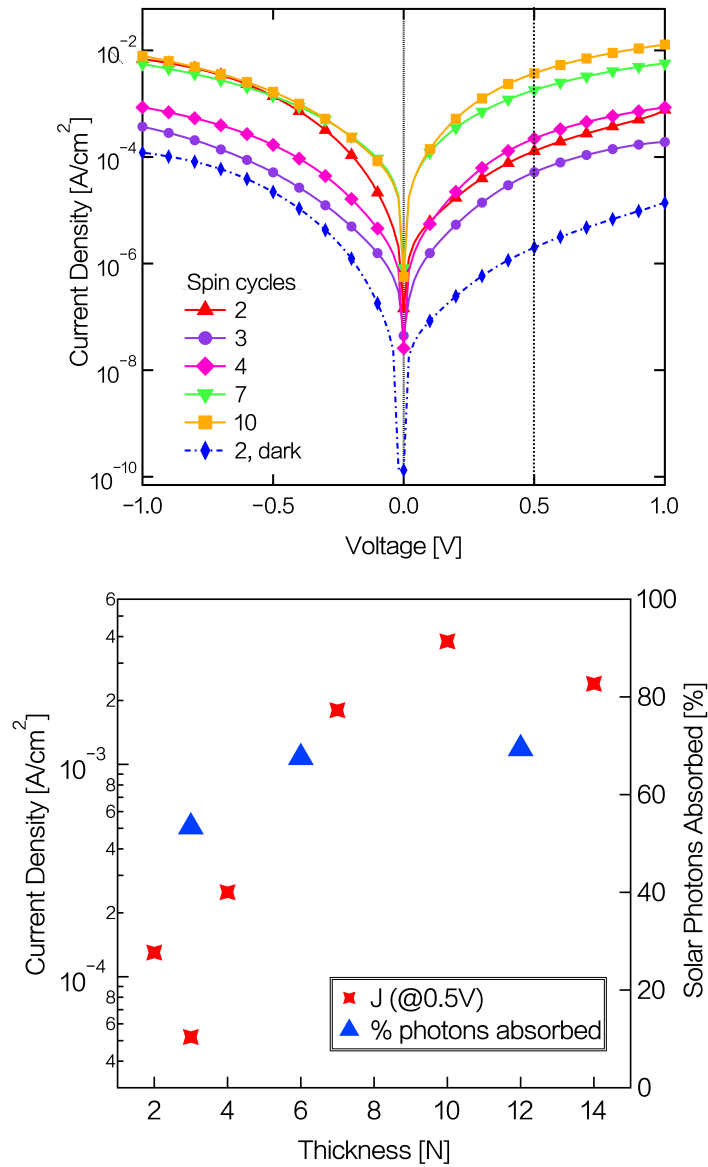


Figure 9.7: (a) J-V curves for the largest QDs vs. absorber layer thickness. Thicknesses are indicated by N, where N is the number of layers applied sequentially via spin-coating followed by a brief soak in hydrazine. N=1 is roughly equivalent to 100 nm. (b) Average photocurrents in our devices at a 0.5 V bias and percentage of solar photons absorbed, as a function of device thickness.

resistive, likely due to leakiness across the Ge NP layer. The TiO_2 sol-gel layer prevents this leakiness in our heterojunction devices, while the TiO_2 NP layer aids in charge extraction.

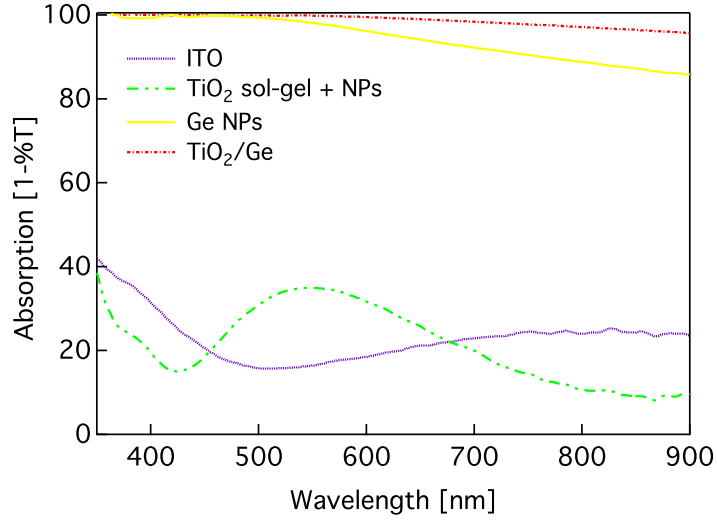


Figure 9.8: UV-Vis absorption spectra of pure Ge film on quartz, ITO on glass, and pure TiO_2 solgel and NP layers on quartz.

Additionally, we isolate improvement by looking at the absorption of individual components along with external quantum efficiency (EQE) of the device. Figure 9.8 shows UV-Vis absorption spectra of the ITO layer on glass, Ge NPs only, TiO_2 layer, and full TiO_2 -Ge NP heterojunction devices, however signals were too low for reliable EQE measurements. The large increase in absorption from TiO_2 only to full device stack indicates the window layer alone is not responsible for the increases in photocurrents.

9.3.2 Effect of Quantum Dot Size on Device Performance

To examine the effect of QD size on device performance, we held the thickness of Ge layers in subsequent devices constant at ~ 300 nm. In Figure 9.9, J-V curves for devices made with each size QD are shown. These trends hold over many devices, and indicate the largest QDs yield best performance, with best photocurrents at 0.5 V around 22 mA cm^{-2} while both smaller sizes have currents at 0.5 V of $10^{-3} \text{ A cm}^{-2}$. This is expected, as currents increase with QD size due to a larger percentage of the solar spectrum being available for carrier generation. Previous size-dependent studies with binary group IV-VI QD systems have shown evidence for increased mobilities with increasing QD size due to the smaller number of hops a carrier must take between generation sites and extraction interfaces [48], which our results seem to support. Additionally, optical characterizations of the Ge QDs used suggest the smaller NPs become increasingly amorphous [61], which could also play a role in their lower performance.

9.3.3 Device Optimization – Back Contact Studies

Another device design choice involves proper selection of the back contact to facilitate non-impeded charge extraction. Fig. 4b shows J-V characteristics of devices made with gold, silver, and aluminum back contacts. Ag and Al should both form ohmic contacts, however we find that Ag is the best performer in terms of favoring hole extraction. As seen in the inset of Fig. 4, the choice of contact can increase performance by up to 3 orders of magnitude, with Ag backed devices having currents 5 orders of magnitude greater than previous hybrid Ge/polymer devices [70].

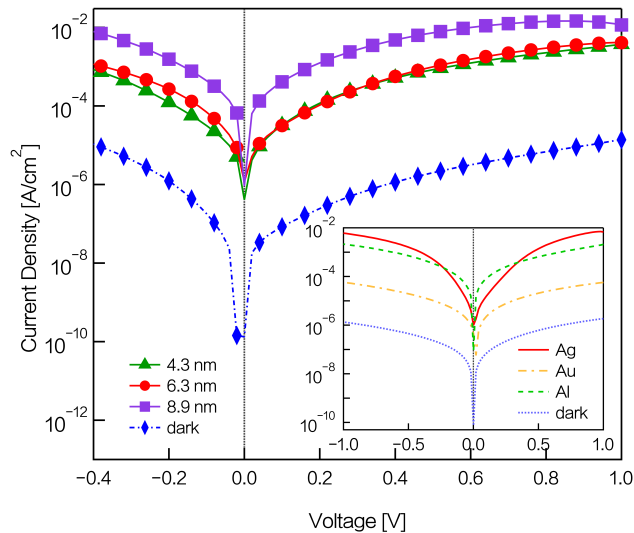


Figure 9.9: J-V characteristics of devices made with different sized QDs. All devices shown have absorber layer thickness ~ 300 nm. Inset: J-V curves show the difference in performance when back contact is varied.

Although we have achieved large increases in photocurrents, our devices behave as photoconductors, not photovoltaics, in that they do not have any meaningful open-circuit voltage. Based on our approximated energy levels, we should observe photovoltages $< 0.3V$. Our low photovoltages are likely a result of poor charge extraction at the electrode.

Additionally, it is unclear whether hydrazine is on the surface of the QD, as the expected Ge-N peak at 650 cm^{-1} in the FTIR spectra (Figure 9.3) is missing [77]. Our EDT + hydrazine devices perform more poorly than the majority of hydrazine-only devices (Figure 9.10). The hydrazine treatment was applied first in our trials, as an initial EDT treatment renders the film soluble. Other experiments have shown that hydrazine not only replaces the capping ligand but also acts on the transport

mechanisms and in some cases renders the QDs n-type [20, 14], which could be the cause of similar results between hydrazine + EDT and hydrazine only films. Recent theoretical studies indicate H-bonded ligands create sub-valance band donor states, further limiting the available photovoltage [78].

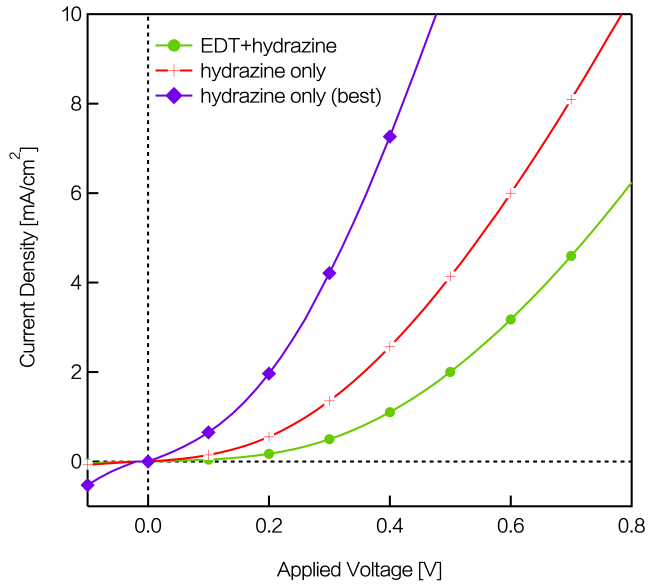


Figure 9.10: J-V characteristics of device made with sequential hydrazine/EDT treatments show no difference from devices made using just hydrazine.

9.4 Conclusion

In conclusion, we have fabricated and studied TiO_2 -Ge NP photodetectors, with particular interest paid to performance enhancements related to device design, Ge layer thickness and NP size. We have achieved ultra-thin (~ 200 nm) devices with

photocurrents at 0.5 V of 10^{-4} A cm $^{-2}$ while the thickest devices have photocurrents at 0.5 V of 10^{-2} A cm $^{-2}$ with on-off ratios > 100 , which represents 5 orders of magnitude increase in performance over previously fabricated Ge CQD devices. The best devices have photocurrents of 23 mA cm $^{-2}$ at 0.5 V bias, which is half of the ideal maximum 46 mA cm $^{-2}$ and comparable to those achieved in thin-film bulk Ge photovoltaic devices [71], opening the door for the use of Ge QDs in energy conversion applications. We note that the junction used herein is not optimal and upon further improvement or change in device structure, both increased photocurrents and photovoltages should be expected. Various device structures are being designed with the dual goals of achieving similarly high photocurrents at 0 V bias and increasing photovoltages.

9.4.1 Acknowledgments

The authors would like to thank the MACS laboratory at NASA Ames Research Center for their use of the Hitachi HR-SEM S4800. This work was funded by the NSF Solar program (NSF DMR 1035478).

Chapter 10

Ge QD Solar Cells

Here, we present the first reported all-nanocrystal Ge solar cell (QDSC) fabricated utilizing TiO_2 as the window layer. After hydrazine exchange, our Ge QDSCs are photoconductive and require no further anneals or surface treatments, greatly simplifying fabrication. Spun-cast and dip-coated donor/acceptor type device structures have been investigated, with performance versus QD size and Ge layer thickness explored. For our best TiO_2 -Ge NP solar cell, short circuit currents of $450 \mu\text{A}$ and open circuit voltages of 0.335 V are achieved. While these figures represent a large increase in performance for Ge QDSC devices, the currents are still quite low compared to PbX chalcogenide QD systems. This discrepancy is studied via analysis of intensity-dependent current-voltage characteristics, which reveal that our photocurrents are likely limited by the formation of a space-charge region due to unbalanced transport and extraction.

10.1 Introduction

Group IV nanocrystals (NCs) based devices are a topic of interest due to their native optical and electronic properties, their non-toxicity compared to other NC optoelectronic and photovoltaic (PV) candidates, increased IR harvesting, potential efficiency boosts from MEG and bandgap tunability, which allows for many possibilities, including multi-junction photovoltaics from one material [26, 23, 31, 10, 24, 15]. For materials with narrow band gaps and large Bohr radii, such as germanium (Ge), these effects become more pronounced and achievable [67, 68, 59]. In addition to the device engineering benefits, solution-processable Ge NCs offer a potential pathway towards reduction in manufacturing and energy costs since they have high scalability, are cheaper to fabricate, and use less material than both traditional crystalline Group IV materials and the more common Group IV NC vacuum growth and deposition methods.

Recent advances in Ge colloidal syntheses have provided crystalline samples with good size control, enabling rapid investigation of their optoelectronic potential. Several groups [79, 70] report on hybrid optoelectronic devices made with P3HT and Ge quantum dots (QDs) with good responsivity and photocurrents near 10^{-6} A cm^{-2} . Most recently, Neale et al. [75] reported electrically conductive drop-cast films of surface-treated Ge QDs alloys while Parola et al. [80] reported on p-i-n heterostructured Ge QDSCs with a best device power conversion efficiency (η) of 0.006%. Our recent paper [64] showed TiO₂-Ge QD photoconductors achieve similar currents to those found in thin-film Ge photovoltaics at a bias of 0.5 V, but suffer from nonexistent photovoltages.

None of the recent work, however, reports any photovoltaic activity associated with non-hybrid Ge CQD devices nor is any analysis completed.

Here, we report on the fabrication and characterization of spun-cast TiO₂/Ge nanocrystal (NC) heterojunction solar cells. As before, our hydrazine treated films are not insulating and require no anneal, simplifying fabrication and potentially lowering future production costs. Performance is discussed as a function of absorber layer thickness and quantum dot size. After initial thickness optimization, our best device has V_{oc} of 0.335V, likely limited by our choice of junction, and short-circuit currents (J_{sc}) 300 $\mu\text{A}/\text{cm}^2$, with fill factors up to 35%. Though our voltages are close to the expected theoretical maximum [42] for this junction, overall performance is hampered by low photocurrents. Both diode model fits and intensity-dependent current-voltage experiments point to photocurrents limited by a space-charge region (SCR) leading to unbalanced extraction and trap-assisted recombination.

10.2 Experimental Methods

Titanium(IV) ethoxide (technical grade) and anhydrous hydrazine were purchased from Sigma-Aldrich and used as received. TiO₂ nanoparticle paste was acquired from Solaronix. Pre-patterned ITO and FTO on 1" \times 1" Corning glass was provided by Thin Film Devices.

Standard air-free techniques were used throughout synthesis and purification process. Ge QDs with average diameters ranging from 3.6 ± 0.2 nm to 7.6 ± 1.3 nm

were synthesized at UC Davis using a microwave-assisted heating route by the procedure described previously [61]. This synthesis allows for more even heating, crystallization at lower temperatures, and increased reproducibility compared to traditional Schlenk line methods. Samples of 3 size distributions were prepared for these experiments with each resultant quasi-spherical NC size set having dispersity $< 25\%$; Figure 10.1 shows PXRD spectra indicating cubic-Ge. Our Ge NCs are synthesized in and capped with oleylamine, washed in methanol, isolated, and finally dispersed in toluene or hexane to final concentrations of approximately $5\text{-}20 \text{ mg mL}^{-1}$. FTIR spectra (Figure 10.1) of the final Ge NC ink solution show absorption peaks consistent with oleylamine, indicating the presence of the oleylamine capping ligand on the surface. Figure 10.2a shows transmission electron microscope (TEM) images of the 7.6 nm Ge QDs used in these studies.

Current density-voltage (J-V) curves were taken using a calibrated Oriel solar simulator and a Keithley 2400 source meter. UV-Vis-NIR spectra of diluted Ge NP dispersions and films at room temperature were taken using a Perkin Elmer Lambda 750 spectrophotometer and a Stellar Net spectrometer (Thin Film Measurement System), respectively. Transmission electron microscopy (TEM) was performed using a Schottky emitter JEOL2500SE electron microscope operating at a voltage of 200 kV. The images were captured with Digital Micrograph software provided by Gatan Inc. Samples for TEM analysis were prepared by placing a drop of a dilute Ge NP dispersion in toluene or hexane on the carbon coated 200 mesh/400 mesh Cu grids obtained from SPI. FTIR spectra were recorded using a Bruker Alpha spectrophotometer. The topography and

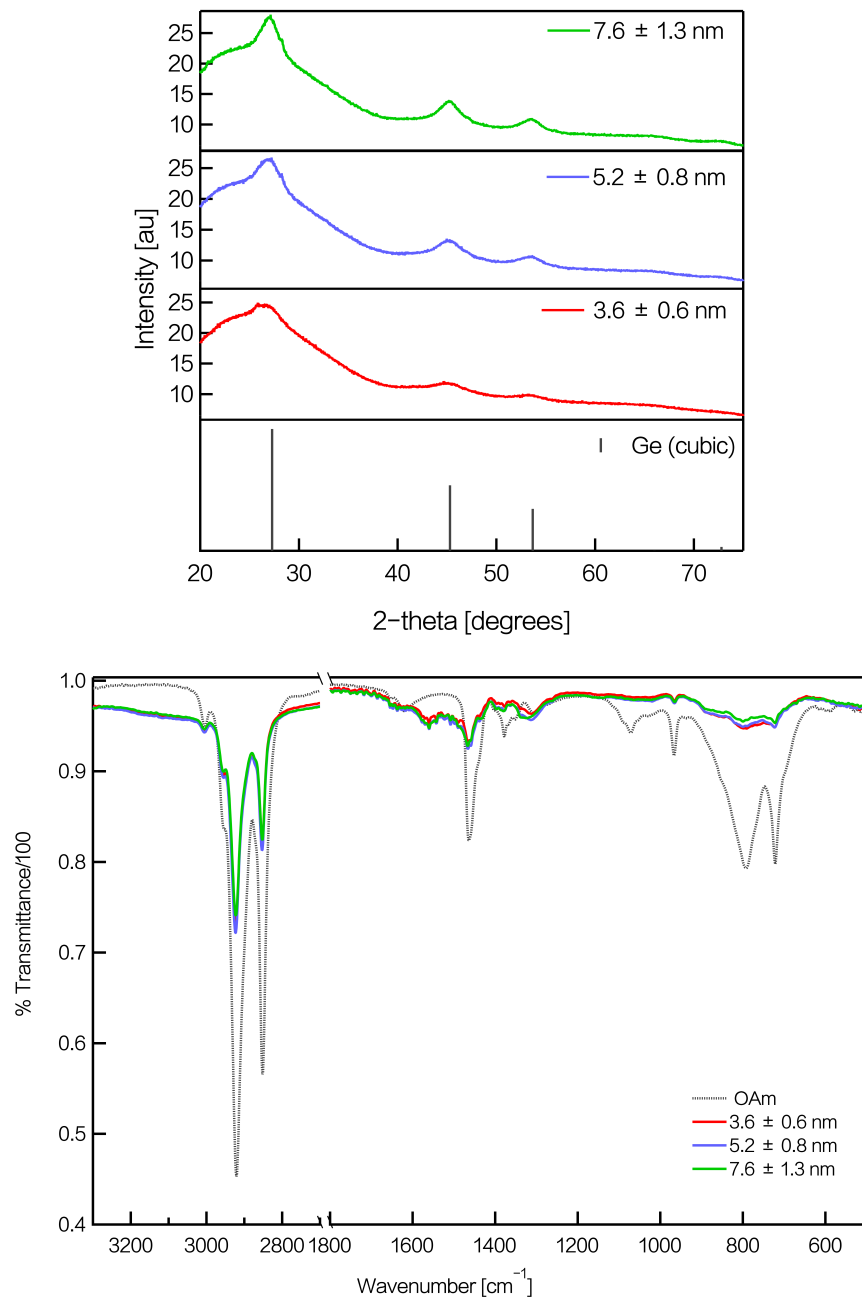


Figure 10.1: (top) PXRD of 3 sizes of Ge QDs synthesized for this experiment show peaks consistent with cubic-Ge. Peak widths indicate decreasing crystallinity with size. (bottom) FTIR confirms presence of OAm on the surface of the Ge NC.

thickness of Ge QD films were obtained via an atomic force microscope (AFM) operating in tapping mode. A Hitachi S-4800 II field emission scanning electron microscope (SEM) operating at 3 kV was employed to observe the cross section of devices and confirm the thickness of each layer; these measurements were carried out in air.

10.2.1 Device Fabrication

TiO₂ sol-gel was prepared by the standard procedure described previously [19]. Glass substrates pre-patterned with Indium Tin Oxide (ITO) or Fluorine Tin Oxide (FTO) electrodes of 150 nm thickness (Thin Film Devices, Anaheim) were cleaned via sonication and washing in a variety of solvents. Both TiO₂ sol-gel and NP pastes were spin-coated onto the cleaned glass substrates sequentially and sintered at 450 °C for 30 minutes in air after deposition to improve conductivity in the TiO₂ window layer. The Ge QD film is then deposited onto the TiO₂ NP film by spin-coating 20 μL of the QD ink in a nitrogen-filled glove box followed by immersing the substrate into a solution of hydrazine in acetonitrile for ~15 seconds to facilitate film formation and increase electronic coupling between the QDs. The thickness of a QD film built up in this way is controlled by spin speeds, number of cycles, and concentration of the QD ink. Finally, 100 nm of silver back contact was thermally evaporated under high vacuum; the area of each device formed is 0.03 cm². A cross-sectional HR-SEM image of the device stack is shown in Figure 10.2b, where the Ge NP layer was made especially thick for easier viewing.

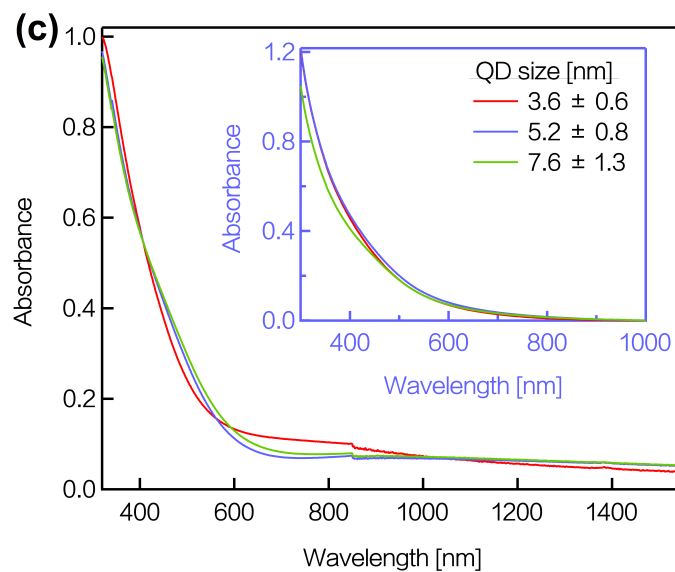
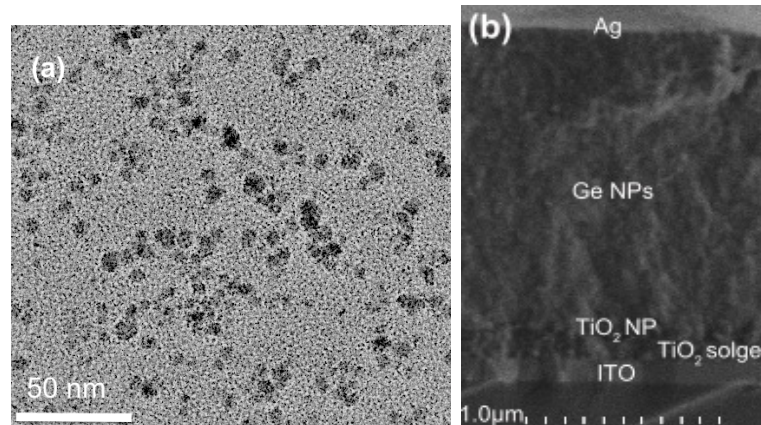


Figure 10.2: (a) TEM image of the 7.6 ± 1.3 nm quasi-spherical Ge QDs synthesized via microwave-assisted heating and used here. (b) HRSEM image of device stack used in these studies. The Ge absorber layer here is purposely made thicker for easier viewing. (c) Absorption spectra for Ge films after ligand exchange with hydrazine show no change in behavior from solution measurements, indicating quantum confinement effects may still be present. Inset: Absorption spectra for Ge QDs capped in oleylamine and dispersed in toluene. While the QD inks only absorb up to about 800 nm, the hydrazine treated films absorb into the NIR, increasing the range of photogeneration and increasing the photocurrents. In both cases the expected excitonic peaks are absent, consistent with solution measurements and literature reports.

10.3 Results

Room-temperature absorbance spectra of each Ge NC solution as received and films formed after hydrazine exchange are shown in Figure 10.2c. Both spectra appear similar; additionally, both spectra have no observable exciton peak, consistent with prior reports in literature and our recent publication [64, 61, 72, 73]. With a Bohr radius exceeding 24 nm, even our 7.6 ± 1.3 nm QD is expected to be in the strong confinement regime, with confinement increases of 200 meV-400 meV from the bulk value 0.67 eV putting our Ge NCs squarely in the range of optimal bandgap for potential MEG enhancement. Films formed with hydrazine exchange are considerably porous and not compact, which could potentially retain positive confinement effects as they do not exhibit bulk characteristics.

10.3.1 Effect of Absorber Layer Thickness and QD Size on Device Performance

The devices shown were spun-cast and made using PECVD FTO as the front contact, however the trends are the same for devices made using ITO and fabricated via dip-coating. Each device in the thickness study uses 5.2 ± 0.8 nm. Figure 10.4a shows the JV characteristic curves under dark and simulated AM1.5G conditions for a range of absorber layer thicknesses, with thickness reported as layer-by-layer cycles, n . The thickness increases linearly with spin cycles, where for these devices, a typical single layer thickness ($n=1$) is ~ 150 -200 nm. The films are porous and the dots can

infill with each subsequent layer, therefore $n=2$ may not exactly be 400 nm. The dark curves exhibit rectification of up to 3 orders of magnitude, confirming actual formation of the TiO_2 -Ge junction.

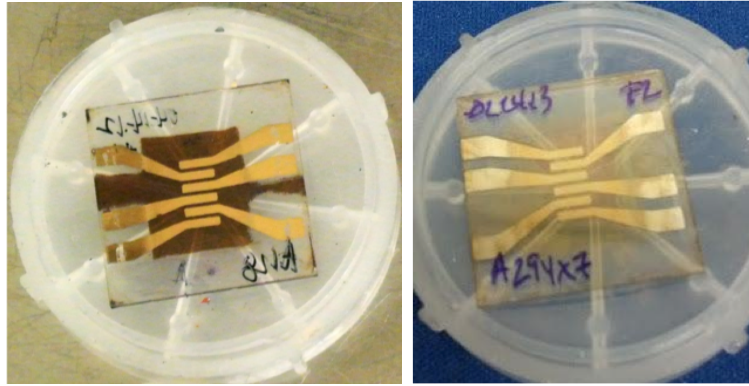


Figure 10.3: A comparison of previous photo conducting devices, on the left, which needed to be quite thick for good absorption, to the current, much thinner, more transparent devices, on the right.

An interesting observation is that the resultant films are not opaque (Figure 10.3). However, we find that even devices with semi-transparent films as thin as 100 nm result in photocurrents, which we attribute to Ge's high oscillator strength [74] when confined. We note that as thickness increases, currents fall drastically; from two to three spin cycles (100-300 nm) photocurrents drop by over half. This is most likely a result of poor charge transport due to both short diffusion lengths, as seen in most QDSCs, and a decrease in film quality. It is suggestive that future films need to be as thin as possible while simultaneously achieving 100% absorption. Film quality was also an issue in our previous work and in similar PbS-TiO_2 heterojunction nanoparticle devices; roughness

Thickness [nm]	J_{sc} [$\mu A \cdot cm^{-2}$]	V_{oc} [mV]	FF	η [%]
2	-227	316	32	.022
3	-107	305	30	.009
4	-87	335	28	.008

Table 10.1: Ge-TiO₂ QDSCs device response as a function of absorber layer thickness. Sample devices are the best of 6 on a chip, fabricated on the same day and illustrative of general trends seen across many devices.

and porosity of quantum dot films have been tied to an increase in surface sites for the carrier recombination [40].

From Table 10.1 we see that as absorber layer thickness increases we also have a decrease in fill factor; decreased fill factors are generally associated with an increase in series resistance, which is also the case here. We note that despite our low power conversion efficiencies (η), our best device PCE of 0.022% represents an 85% increase over the most efficient hybrid-Ge QD device to date and over 200% increase over a device fabricated using Ge NPs as the active absorber on a Si substrate [70].

Even though our best photocurrents have also improved to hundreds of μA , they are still much lower than the other QD systems currently studied, indicating some or all of the following: excitons generated in Ge have very short lifetimes, Ge films need to be of higher quality and as thin as possible, and better passivation of the Ge surface should be sought out. This last point is important: the lack of PL in our Ge NC system indicates incomplete surface passivation. Other colloiddally synthesized Ge NCs also suffer from this issue, with Neale et al synthesizing alkyl-terminated Ge NCs with near-IR PL QYs of less than 0.1% [72].

Another possible explanation is that our junction is not separating as strongly

as we'd like. To test this, we employed hot probe measurements. These very rough experiments consist of using a heat source to quickly determine the majority type of our semiconductor. Using this hot-probe technique, we find that our Ge NCs are n-type. A further confirmation of this n-type behavior is seen in surface photovoltage measurements of the same QDs [81]. These two measurements seem to indicate that along with the n-type TiO₂, we have an n-n junction; this could lead to unbalanced extraction and collection (i.e. only electrons are collected).

Size-dependent investigations were conducted with the absorber layer held constant at ~ 300 nm; additionally, all devices used ITO as the front contact for these studies, with all other fabrication conditions held constant. There have been reports of indium diffusing out of the TCO layer at temperatures above 400°; in order to put these fears to rest, Figure 10.5 shows the results of identical devices made with FTO versus ITO. The differences are quite small on this scale and we are confident in concluding that there are no negative effects when using ITO.

J-V curves under simulated AM1.5G illumination are seen in Figure 10.4b while photovoltaic figures of merit are included in Table 10.2. To highlight the increases in photovoltage and currents over our previous photoconductors, we show their JV curves (open, dashed lines) along with our newest results. We conclude that our smallest QDs with radius 3.6 ± 0.6 nm ($E_g = \sim 1.2$ eV) devices have the highest photovoltages, as expected, and in agreement with many QDSC size studies [82, 34], primarily resulting from the largest difference in quasi Fermi level splitting.

The photocurrents obtained from the 7.6 ± 1.3 nm QDs are the largest, again,

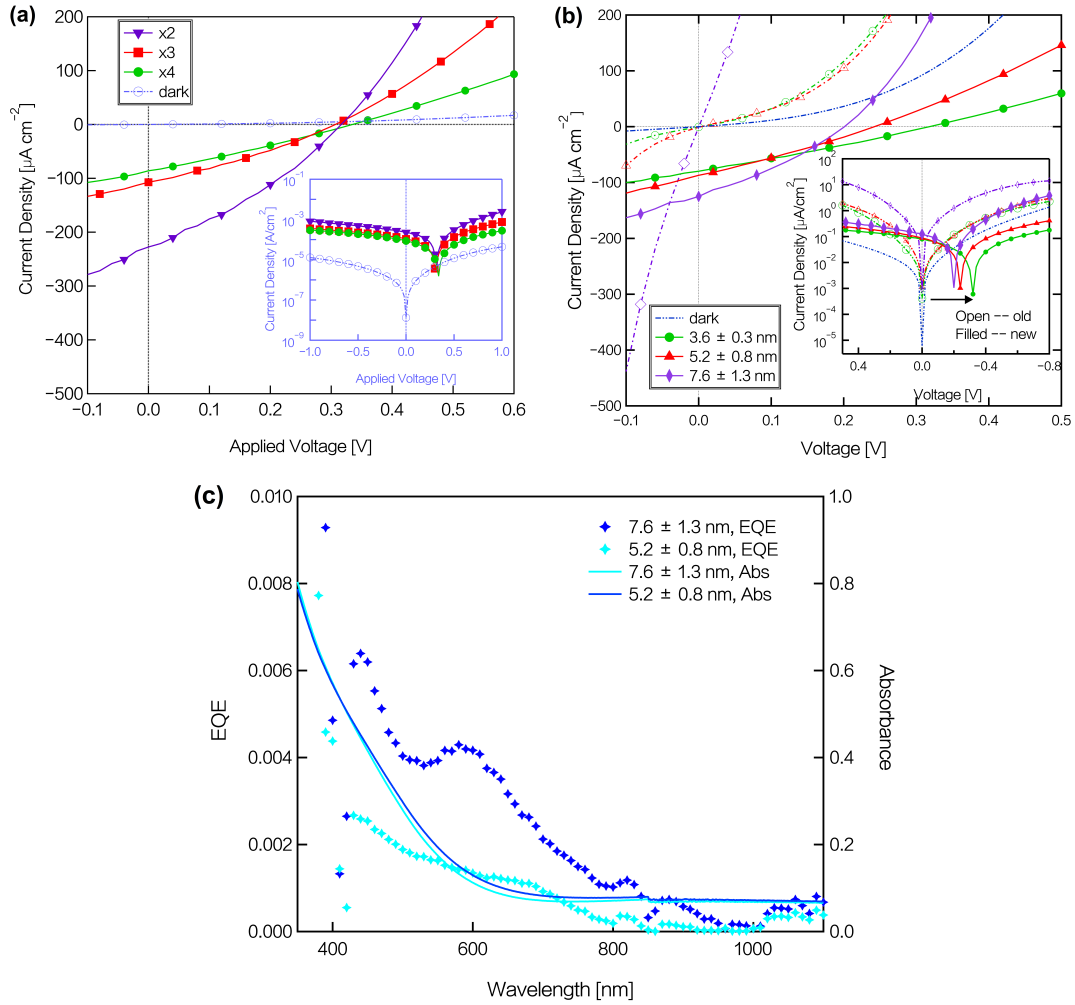


Figure 10.4: Current-voltage curves show thickness and QD size dependencies of the resultant photocurrents. (a) Absorber layer thickness versus performance shows that with as little as one additional spin cycle (~ 150 nm increase in absorber thickness), our currents drop by over half. (b) QD size versus performance indicates that again, as expected, the 7.6 ± 1.3 nm QDs have the highest photocurrents, while the 3.6 ± 0.6 nm QDs have the highest photovoltages. (c) EQE for the 5.2 ± 0.8 nm and 7.6 ± 1.3 nm QDs, along with absorbance spectra of films made with the same sized QD. The EQE spectra has the same general shape of the absorbance spectra, indicating the photocurrents are generated in our Ge QD absorber layer. Integrated photocurrents give an expected short-circuit current of $75 \mu\text{A cm}^{-2}$ for the 7.6 ± 1.3 nm QDs, which is in good agreement with our measured J_{sc} of 79 A cm^{-2} for the same device.

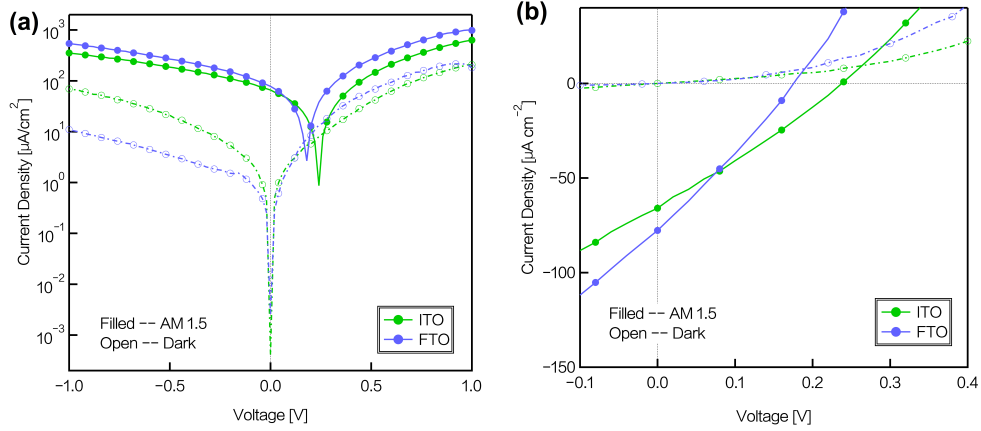


Figure 10.5: (a) Log plot of identical devices fabricated on FTO and ITO. (b) Linear JV curves of the same devices depicted in (a).

as expected, due to a larger percentage of the solar spectrum available for generation. Optical studies of the Ge QDs used in our previous study indicate they become increasingly amorphous as size decreases. We attribute low currents in the 3.6–0.6 nm QDs to a combination of this shift away from crystallinity and decreased spectrum availability.

Figure 10.4c shows the external quantum efficiency (EQE) spectrum for the two largest QDs, 5.2 ± 0.8 and 7.6 ± 1.3 nm. Though the signals are small, we can still gain valuable insight from the shapes of the spectra. Most importantly, the shapes of the spectra are similar to absorbance spectra of the Ge QD films, indicating our currents

r_{QD} [nm]	J_{sc} [$\mu\text{A} \cdot \text{cm}^{-2}$]	V_{oc} [mV]	FF	η [%]
3.6 ± 0.3	-84.2 ± 3.1	335	30.7	.007
5.2 ± 0.8	-83.3 ± 8.6	201	30.5	.005
3.6 ± 0.3	-114 ± 11	174	28.4	.007

Table 10.2: Ge-TiO₂ QDSCs device response as a function of QD size. Values are averages of 6 devices on the chip, fabricated on the same day and illustrative of general trends seen across many devices.

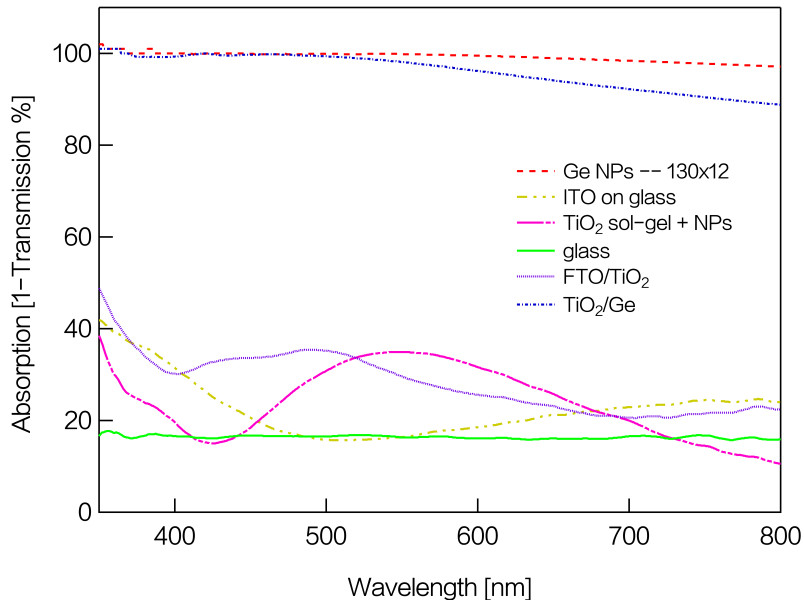


Figure 10.6: Constituent transmission spectra show Ge's contribution to absorption to be much higher than any other layer involved, serving as a second confirmation of photogeneration occurring in the Ge QD absorber layer.

are primarily generated in the Ge absorbing layer. Further confirmation of this can be found by looking at the absorbance of each constituent layer (Figure 10.6); the response from the ITO/TiO₂ layers are negligible, serving as a second confirmation of the Ge QDs photocurrent generating properties.

10.3.2 Intensity-dependent Current-Voltage Experiments

To explain our overall low currents, we employed intensity-dependent JV experiments over a range from 0.5-4 suns. Intensities were determined via the J_{sc} of a calibrated Si photodiode, where the current at 1 sun (100 mW cm^{-2}) is known and we assume a linear response upwards. For these experiments, both the $3.6 \pm 0.6 \text{ nm}$ and

7.6 ± 1.3 nm (smallest and largest) QDs were used, with absorber thicknesses of ~ 200 nm. In Figure 10.7, we see the JV characteristics of devices made with 7.6 ± 1.3 nm (top) and 3.6 ± 0.6 (bottom) QDs, respectively, as a function of increasing intensity from 0.5-4 suns.

For the same devices, Figure 10.8 shows the photovoltaic figures of merit as intensity is increased. We see that both FF and V_{oc} are mostly constant over the range of intensities, while J_{sc} increases linearly as expected. Table 10.3 gives the photovoltaic device parameters of the 7.6 ± 1.3 nm devices in the intensity-dependent study.

Figure 10.9 shows photocurrents versus incident intensity fit to a simple power law,

$$J_{sc} = I^\beta. \quad (10.1)$$

In this scheme, $\beta=1$ corresponds with generation-limited currents, while $\beta=0.75$ indicates formation of a space-charge region which limits photocurrents [82, 83]. We find that for our 3.6 ± 0.6 nm QDs, $\beta = 0.85 \pm 0.03$, while for the 7.6 ± 1.3 nm QDs, $\beta = 0.90 \pm 0.01$. These values are indicative of some SCR-related limiting effect, most likely due to unbalanced transport and extraction. R_s (Table 10.3) are also quite large

Intensity [suns]	J_{sc} [$\mu A \cdot cm^{-2}$]	V_{oc} [mV]	FF	η [%]	R_s [Ωcm^2]	R_{sh} [Ωcm^2]
1	-124	201	30.4	.008	974	3247
2	-227	199	30.7	.013	455	1591
3	-296	196	31.3	.016	324	1234
4	-354	192	31.3	.021	311	1158

Table 10.3: Photovoltaic device parameters of 7.6 ± 1.3 nm QDs as a function of incident light intensity. The series (R_s) and shunt (R_{sh}) resistances were calculated using dV/dJ at $V = V_{oc}$ and $V = -J_{sc}$ for each of the JV curves.

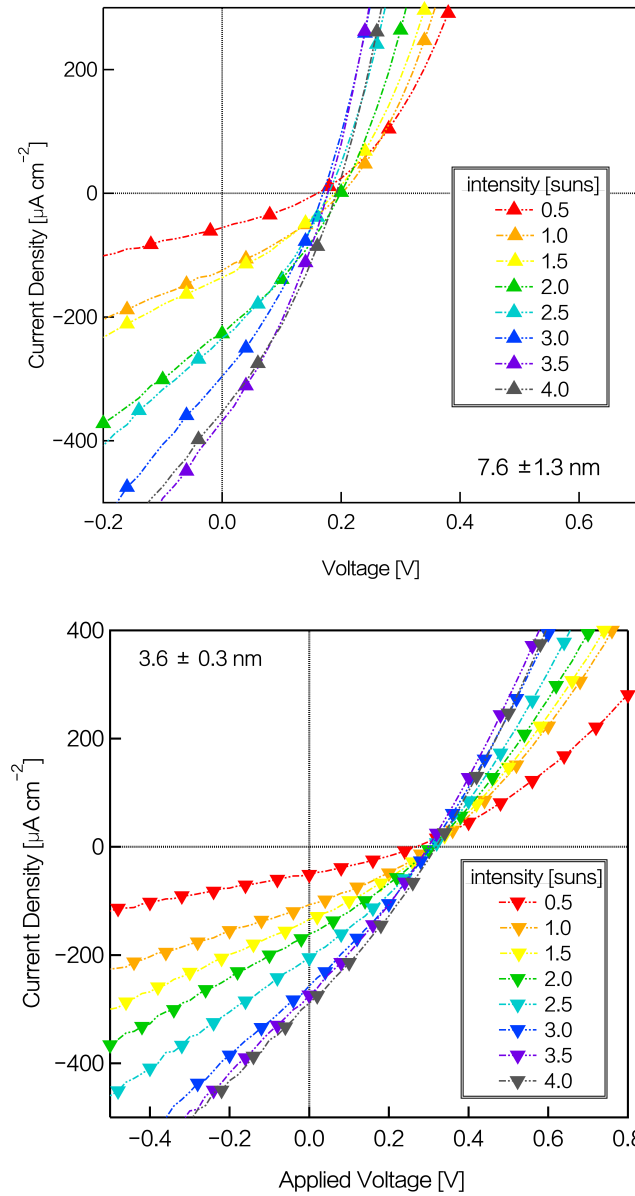


Figure 10.7: JV curves for (top) 7.6 ± 1.3 nm and (bottom) 3.6 ± 0.3 nm QDs with increasing illumination intensity, from 0.5 4 sun equivalent. The curves exhibit saturation, indicating maximum absorption.

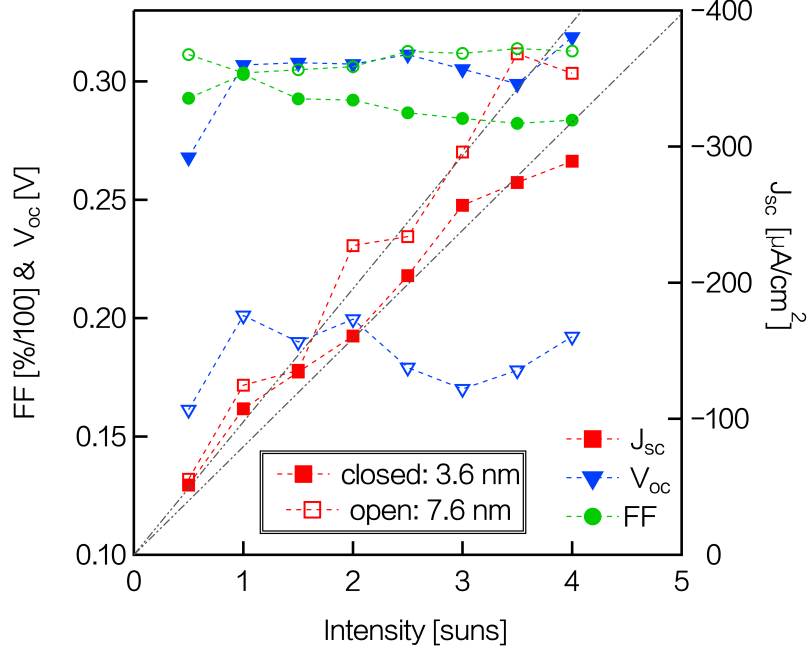


Figure 10.8: Photovoltaic performance figures of merit (FF, J_{sc} and V_{oc}) versus incident illumination intensity for both 3.6 ± 0.6 nm and 7.6 ± 1.3 nm QDs, indicated by closed and open symbols, respectively. The black dashed lines are guidelines through 0A for J_{sc} . FF and V_{oc} are mostly constant as intensities increase, and can be found on the left axis with currents on the right.

in these devices, which has been associated with lower mobilities, and could be another reason for our low currents.

In addition to our intensity-dependent experiments, we attempted to model our devices using the ideal diode model, inclusive of parasitic effects,

$$J = J_0 \exp \left[\frac{q}{(A\kappa_B T)(V - RJ)} \right] + GV + J_L \quad (10.2)$$

where J_0 is the saturation current, A is the ideality factor, q is electron charge. κ_B is Boltzmann constant, T is temperature, R is series resistance, G is shunt conductance, and J_L is current under illumination to our best performing device to determine R , G ,

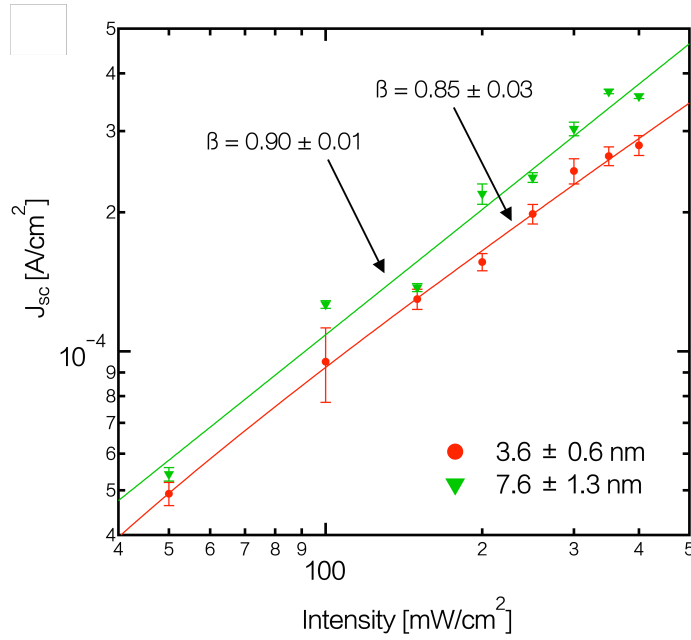


Figure 10.9: J_{sc} versus incident intensity fit to a simple power law, $J_{sc} \propto I^\beta$. Here, for our smallest QDs $\beta = 0.85 \pm 0.03$, while for the largest, $\beta = 0.90 \pm 0.01$. Typically, $\beta = 1$ corresponds with generation-limited currents, while $\beta = 0.75$ indicates formation of a space-charge region which limits photocurrents. Our values are indicative of some SCR-related limiting effects, most likely due to unbalanced transport and extraction.

A, and J_0 [84, 85]. Unfortunately, due to the high parasitic losses in our device, this model is not accurate for determination of R, A, or J_0 . We can, however, obtain a reasonable value for shunt conductance, $G = 0.05 \text{ mS cm}^{-2}$ (Figure 10.10):

Shunt conductance, which is $G = 0.5 \text{ mS cm}^{-2}$ under illumination, corresponding to a shunt resistance, R_{sh} of $\sim 2000 \text{ } \Omega \text{ cm}^2$. Table 10.3 shows $R_{sh} = 3247 \text{ } \Omega \text{ cm}^2$, so we should take this fit value as a lower bound.

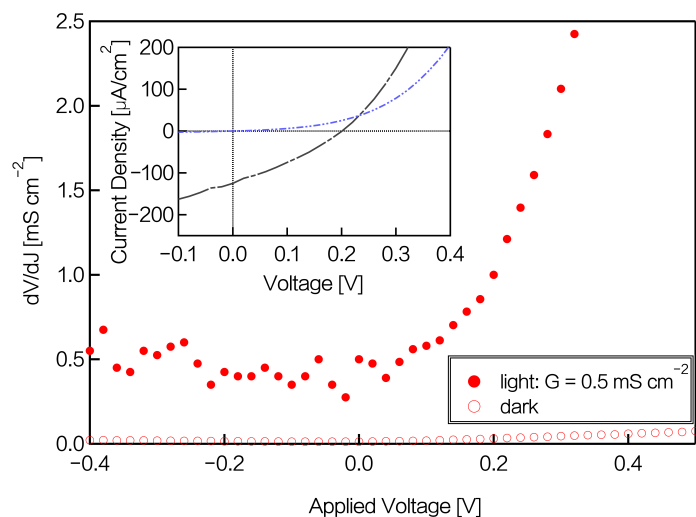


Figure 10.10: Shunt conductance for sample Ge QDSC. Inset: light and dark JV curves of the same device.

10.4 Conclusion

In conclusion, we report on quantum dot $\text{TiO}_2\text{-Ge}$ heterojunction solar cells fabricated via multi-layer spin- and/or dip-coating, with specific interest paid to performance enhancements through optimization of absorber layer thickness and quantum dot size. Our devices are conducting after a simple hydrazine soak and require no costly anneals or other surface treatments, greatly simplifying the fabrication of our Ge QDSCs. We see an increase of over $100 \mu\text{A cm}^{-2}$ in currents for all QD sizes over our previous work. Our devices now exhibit photovoltages and consequently, behave as photovoltaics, with a best device fill factors up to 35%, short-circuit currents of $450 \mu\text{A cm}^{-2}$ and open-circuit voltages of 335 mV, which is close to the maximum expected V_{oc} available given our junction.

Though low, our power conversion efficiency of 0.022% represents an 85% increase over hybrid devices and over 200% increase over previous Ge QDs on Si pi-n devices. Size-dependent performance is congruent with other QDSC systems recently studied. Diode modeling indicates our solar cells have significant parasitic issues. Further investigation with intensity-dependent experiments reveal that our photocurrents are limited by unbalanced transport, leading to the formation of a space charge region and unbalanced extraction. Additionally, there is some trap-assisted recombination, lowering our photovoltages and overall performance. Despite these issues, this work represents clear evidence of the potential for Ge QDs to be used in future photovoltaic devices.

The devices presented above are not optimized for performance, and as such, there is no reason to expect large increases upon optimization. Other suggestions for immediate improvement include better surface passivation, surface treatments for higher electrical conductivity, anneals, improved device design, and potential doping to improve carrier separation and extraction, the latter of these necessitating the largest control over synthesis.

10.4.1 Acknowledgments

The authors would like to thank the MACS lab at NASA Ames for their use of the HR-SEM S4800. We acknowledge support through the NSF Solar program (NSF DMR 1035478).

Part IV

Conclusion

Not only are the majority of our current energy sources causing detriment to our planet's well-being, they are rapidly running out. The argument for a major shift towards clean, renewable energy was made long ago. For the past 40 years, researchers have helped push the field of solar energy conversion to the limit. Now we need to beat the limit. Quantum dots could be the proverbial homerun for photovoltaics due to their tunable optical and electronic properties, lower materials consumption, the simplicity of colloidal fabrication routes, easy integration in multi-junction photovoltaics, and their ability to generate more than one carrier per absorbed photon.

The work presented in this dissertation highlights a few of the potential routes available for increasing solar energy conversion through use of tailored nanomaterials. Specifically, we explore multiple pathways around the Shockley-Queissar limit using quantum dots.

In the first route, $\text{PbS}_x\text{Se}_{1-x}$ QD solar cells are fabricated and characterized; the results indicate that even a small addition of Se ($x=0.9$) into the PbS system is enough to simultaneously provide large photocurrents and photovoltages, resulting in 4.5% PCE. The addition of Se also boosts EQE $> 100\%$ at an earlier threshold than previously reported. This route represents a performance improvement through increases in photocurrent while showcasing Multiple Exciton Generation-like behavior. The second route involves using bandgap grading techniques to increase the photovoltages of PbS QD solar cells. We have achieved 200mV V_{oc} boosts; this method could easily produce even larger performance increases given highly monodisperse nanocrystals with better surface passivation. Additionally, the gradation technique can simply be modified for

use in colloidal QD multi-junction solar cells due to the ease of solution synthesis and deposition techniques. The third route involves changing the canonical PbX QD PV system for Ge; this change offers a future-proof system that is safer, more abundant, and lays the groundwork for Si QD solar cells.

Particularly exciting and novel are the projects done for this third pathway. We present the highest reported photocurrents for all-Ge NC photoconductors with size-dependent characteristics. Additionally, we present the first-reported all-nanocrystalline TiO₂-Ge solar cell, colloidally fabricated and electrically conductive after a simple one-step ligand exchange. Group IV QD materials offer all of the same benefits found in PbX systems with none of the negatives. The field is quite young but has tremendous potential. Ge QD inks could feasibly be the answer to solar energy conversion, however a few issues need to be resolved. On the materials side of things, we need more robust syntheses with better size control, surface passivation, and control over the doping profile. On the theoretical side, we need to achieve deeper understanding of the electronic properties as Ge QDs become confined; this would enable better device design.

The bandgap tunability and ease of fabrication with solution synthesis and colloidal inks mean quick industrial up-scale, and sooner, rather than later, we may begin to reap the benefits of QD solar cells.

Bibliography

- [1] Thomas F. Stocker, Dahe Qin, Gian-Kasper Plattner, Melinda M.B. Tignor, Simon K. Allen, Judith Boschung, Alexandre Nauels, Yu Xia, Vincent Bex, and Pauline M. Midgley. Climate change 2013: The physical science basis. contribution of working group i to the fifth assessment report of the intergovernmental panel on climate change. Technical report, IPCC, September 2013.
- [2] BP. Statistical review of world energy 2013. Technical report, 2013.
- [3] International Energy Agency. 2013 key energy statistics. Technical report, 2013.
- [4] William Shockley and Hans J. Queisser. Detailed balance limit of efficiency of p-n junction solar cells. *Journal of Applied Physics*, 32(3):510–519, 1961.
- [5] Jenny Nelson. *The Physics of Solar Cells*. Imperial College Press, 2009.
- [6] S.M. Sze and K.K. Ng. *Physics of Semiconductor Devices*. Wiley, 2006.
- [7] Al L Efros and Al L Efros. Interband absorption of light in a semiconductor sphere. *Soviet Physics Semiconductors-Ussr*, 16(7):772–775, 1982.

- [8] Arthur J Nozik. Spectroscopy and hot electron relaxation dynamics in semiconductor quantum wells and quantum dots. *Annual Review of Physical Chemistry*, 52(1):193–231, 2001. PMID: 11326064.
- [9] Randy J. Ellingson, Matthew C. Beard, Justin C. Johnson, Pingrong Yu, Olga I. Micic, Arthur J. Nozik, Andrew Shabaev, and Alexander L. Efros. Highly efficient multiple exciton generation in colloidal pbse and pbs quantum dots. *Nano Letters*, 5(5):865–871, 2005.
- [10] Hugh W. Hillhouse and Matthew C. Beard. Solar cells from colloidal nanocrystals: Fundamentals, materials, devices, and economics. *Current Opinion in Colloid Interface Science*, 14(4):245 – 259, 2009.
- [11] Gautham Nair, Scott M. Geyer, Liang-Yi Chang, and Mounqi G. Bawendi. Carrier multiplication yields in pbs and pbse nanocrystals measured by transient photoluminescence. *Phys. Rev. B*, 78:125325, Sep 2008.
- [12] Matthew C. Beard, Aaron G. Midgett, Matt Law, Octavi E. Semonin, Randy J. Ellingson, and Arthur J. Nozik. Variations in the quantum efficiency of multiple exciton generation for a series of chemically treated pbse nanocrystal films. *Nano Letters*, 9(2):836–845, 2009.
- [13] Michiel Aerts, C. S. Suchand Sandeep, Yunan Gao, Tom J. Savenije, Juleon M. Schins, Arjan J. Houtepen, Sachin Kinge, and Laurens D. A. Siebbeles. Free charges

- produced by carrier multiplication in strongly coupled pbse quantum dot films. *Nano Letters*, 11(10):4485–4489, 2011.
- [14] Joseph M. Luther, Matthew C. Beard, Qing Song, Matt Law, Randy J. Ellingson, and Arthur J. Nozik. Multiple exciton generation in films of electronically coupled pbse quantum dots. *Nano Letters*, 7(6):1779–1784, 2014/05/07 2007.
- [15] Octavi E Semonin, Joseph M Luther, Sukgeun Choi, Hsiang-Yu Chen, Jianbo Gao, Arthur J Nozik, and Matthew C Beard. Peak external photocurrent quantum efficiency exceeding 100% via meq in a quantum dot solar cell. *Science*, 334(6062):1530–1533, 2011.
- [16] Matthew C. Beard, Joseph M. Luther, Octavi E. Semonin, and Arthur J. Nozik. Third generation photovoltaics based on multiple exciton generation in quantum confined semiconductors. *Accounts of Chemical Research*, 46(6):1252–1260, 2013.
- [17] Joseph M. Luther, Jianbo Gao, Matthew T. Lloyd, Octavi E. Semonin, Matthew C. Beard, and Arthur J. Nozik. Stability assessment on a 3heterojunction solar cell. *Advanced Materials*, 22(33):3704–3707, 2010.
- [18] Zhijun Ning, Yuan Ren, Sjoerd Hoogland, Oleksandr Voznyy, Larissa Levina, Philipp Stadler, Xinzheng Lan, David Zhitomirsky, and Edward H Sargent. All-inorganic colloidal quantum dot photovoltaics employing solution-phase halide passivation. *Advanced Materials*, 24(47):6295–6299, 2012.
- [19] A. C. Arango, L. R. Johnson, V. N. Bliznyuk, Z. Schlesinger, S. A. Carter, and

- H.-H. Hörhold. Efficient titanium oxide/conjugated polymer photovoltaics for solar energy conversion. *Advanced Materials*, 12(22):1689–1692, 2000.
- [20] Dmitri V. Talapin and Christopher B. Murray. Pbse nanocrystal solids for n- and p-channel thin film field-effect transistors. *Science*, 310(5745):86–89, 2005.
- [21] Michal Soreni-Harari, Nir Yaacobi-Gross, Dov Steiner, Assaf Aharoni, Uri Banin, Oded Millo, and Nir Tessler. Tuning energetic levels in nanocrystal quantum dots through surface manipulations. *Nano letters*, 8(2):678–684, 2008.
- [22] Jacek Jasieniak, Marco Califano, and Scott E Watkins. Size-dependent valence and conduction band-edge energies of semiconductor nanocrystals. *ACS nano*, 5(7):5888–5902, 2011.
- [23] A. J. Nozik, M. C. Beard, J. M. Luther, M. Law, R. J. Ellingson, and J. C. Johnson. Semiconductor quantum dots and quantum dot arrays and applications of multiple exciton generation to third-generation photovoltaic solar cells. *Chemical Reviews*, 110(11):6873–6890, 2010.
- [24] Guangmei Zhai, Carena P Church, Alison J Breeze, Daoli Zhang, Glenn B Alers, and Sue A Carter. Quantum dot pbs_{0.9}se_{0.1}/tio₂ heterojunction solar cells. *Nanotechnology*, 23:405401, 09 2012.
- [25] Frank W. Wise. Lead salt quantum dots: the limit of strong quantum confinement. *Accounts of Chemical Research*, 33(11):773–780, 2000. PMID: 11087314.
- [26] R. D. Schaller and V. I. Klimov. High efficiency carrier multiplication in pbse

- nanocrystals: Implications for solar energy conversion. *Phys. Rev. Lett.*, 92:186601, May 2004.
- [27] Ratan Debnath, Osman Bakr, and Edward H. Sargent. Solution-processed colloidal quantum dot photovoltaics: A perspective. *Energy Environ. Sci.*, 4:4870–4881, 2011.
- [28] Saim Emin, Surya P. Singh, Liyuan Han, Norifusa Satoh, and Ashrafur Islam. Colloidal quantum dot solar cells. *Solar Energy*, 85(6):1264 – 1282, 2011.
- [29] Wanli Ma, Joseph M. Luther, Haimei Zheng, Yue Wu, and A. Paul Alivisatos. Photovoltaic devices employing ternary pbsxse1-x nanocrystals. *Nano Letters*, 9(4):1699–1703, 2009.
- [30] Kui Yu, Jianying Ouyang, Yanguang Zhang, Hsien-Tse Tung, Shuqiong Lin, Robert A. L. Nagelkerke, David Kingston, Xiaohua Wu, Donald M. Leek, Diana Wilkinson, Chunsheng Li, In-Gann Chen, and Ye Tao. Low-temperature noninjection approach to homogeneously-alloyed pbsexs1x colloidal nanocrystals for photovoltaic applications. *ACS Applied Materials Interfaces*, 3(5):1511–1520, 2011.
- [31] Jiang Tang and Edward H Sargent. Infrared colloidal quantum dots for photovoltaics: fundamentals and recent progress. *Adv Mater*, 23(1):12–29, Jan 2011.
- [32] Justin B. Sambur, Thomas Novet, and B. A. Parkinson. Multiple exciton collection in a sensitized photovoltaic system. *Science*, 330(6000):63–66, 2010.

- [33] Guangmei Zhai, Anna Bezryadina, Alison J. Breeze, Daoli Zhang, Glenn B. Alers, and Sue A. Carter. Air stability of tio₂/pbs colloidal nanoparticle solar cells and its impact on power efficiency. *Applied Physics Letters*, 99(6):–, 2011.
- [34] Joseph M. Luther, Matt Law, Matthew C. Beard, Qing Song, Matthew O. Reese, Randy J. Ellingson, and Arthur J. Nozik. Schottky solar cells based on colloidal nanocrystal films. *Nano Letters*, 8(10):3488–3492, 2008. PMID: 18729414.
- [35] Joseph M. Luther, Matt Law, Qing Song, Craig L. Perkins, Matthew C. Beard, and Arthur J. Nozik. Structural, optical, and electrical properties of self-assembled films of pbse nanocrystals treated with 1,2-ethanedithiol. *ACS Nano*, 2(2):271–280, 2008.
- [36] Ludovico Cademartiri, Erica Montanari, Gianluca Calestani, Andrea Migliori, Antonietta Guagliardi, and Geoffrey A. Ozin. Size-dependent extinction coefficients of pbs quantum dots. *Journal of the American Chemical Society*, 128(31):10337–10346, 2006.
- [37] Iwan Moreels, Karel Lambert, David De Muynck, Frank Vanhaecke, Dirk Poelman, José C. Martins, Guy Allan, and Zeger Hens. Composition and size-dependent extinction coefficient of colloidal pbse quantum dots. *Chemistry of Materials*, 19(25):6101–6106, 2007.
- [38] D. Aaron R. Barkhouse, Ratan Debnath, Illan J. Kramer, David Zhitomirsky, Andras G. Pattantyus-Abraham, Larissa Levina, Lioz Etgar, Michael Grätzel, and

- Edward H. Sargent. Depleted bulk heterojunction colloidal quantum dot photovoltaics. *Advanced Materials*, 23(28):3134–3138, 2011.
- [39] MRS Photovoltaic Workshop. *Effect of air exposure on performance of PbS/TiO₂ heterojunction colloidal quantum dot solar cells*, Denver, CO, 2010.
- [40] Tong Ju, Rebekah L. Graham, Guangmei Zhai, Yvonne W. Rodriguez, Alison J. Breeze, Lily Yang, Glenn B. Alers, and Sue A. Carter. High efficiency mesoporous titanium oxide pbs quantum dot solar cells at low temperature. *Applied Physics Letters*, 97(4):043106, 2010.
- [41] Ghada I. Koleilat, Larissa Levina, Harnik Shukla, Stefan H. Myrskog, Sean Hinds, Andras G. Pattantyus-Abraham, and Edward H. Sargent. Efficient, stable infrared photovoltaics based on solution-cast colloidal quantum dots. *ACS Nano*, 2(5):833–840, 2008.
- [42] Kurtis S Leschkies, Timothy J Beatty, Moon Sung Kang, David J Norris, and Eray S Aydil. Solar cells based on junctions between colloidal pbse nanocrystals and thin zno films. *ACS nano*, 3(11):3638–3648, 2009.
- [43] Ratan Debnath, Mark T Greiner, Illan J Kramer, Armin Fischer, Jiang Tang, D Aaron R Barkhouse, Xihua Wang, Larissa Levina, Zheng-Hong Lu, and Edward H Sargent. Depleted-heterojunction colloidal quantum dot photovoltaics employing low-cost electrical contacts. *Applied Physics Letters*, 97:023109, 2010.
- [44] Jianbo Gao, Joseph M Luther, Octavi E Semonin, Randy J Ellingson, Arthur J

- Nozik, and Matthew C Beard. Quantum dot size dependent j- v characteristics in heterojunction zno/pbs quantum dot solar cells. *Nano letters*, 2011.
- [45] Joshua J. Choi, Yee-Fun Lim, Mitk’El B. Santiago-Berrios, Matthew Oh, Byung-Ryool Hyun, Liangfeng Sun, Adam C. Bartnik, Augusta Goedhart, George G. Malliaras, Héctor D. Abruña, Frank W. Wise, and Tobias Hanrath. Pbse nanocrystal excitonic solar cells. *Nano Letters*, 9(11):3749–3755, 2009. PMID: 19719095.
- [46] Yamamoto et al. MRS Spring Meeting.
- [47] Keith W. Johnston, Andras G. Pattantyus-Abraham, Jason P. Clifford, Stefan H. Myrskog, Dean D. MacNeil, Larissa Levina, and Edward H. Sargent. Schottky-quantum dot photovoltaics for efficient infrared power conversion. *Applied Physics Letters*, 92(15):–, 2008.
- [48] Yao Liu, Markelle Gibbs, James Puthussery, Steven Gaik, Rachelle Ihly, Hugh W Hillhouse, and Matt Law. Dependence of carrier mobility on nanocrystal size and ligand length in pbse nanocrystal solids. *Nano letters*, 10(5):1960–1969, 2010.
- [49] Marco Califano, Alberto Franceschetti, and Alex Zunger. Temperature dependence of excitonic radiative decay in cdse quantum dots: the role of surface hole traps. *Nano Letters*, 5(12):2360–2364, 2005. PMID: 16351178.
- [50] Woojun Yoon, Janice E. Boercker, Matthew P. Lumb, Diogenes Placencia, Edward E. Foos, and Joseph G. Tischler. Enhanced open-circuit voltage of pbs nanocrystal quantum dot solar cells. *Sci. Rep.*, 3, 07 2013.

- [51] M. Wolf. Drift fields in photovoltaic solar energy converter cells. *Proceedings of the IEEE*, 51(5):674–693, May 1963.
- [52] Oldwig von Roos. A simple theory of backsurfacefield (bsf) solar cells. *Journal of Applied Physics*, 50(8):5371–5374, 1979.
- [53] P. Peumans and S. R. Forrest. Very-high-efficiency double-heterostructure copper phthalocyanine/c60 photovoltaic cells. *Applied Physics Letters*, 79(1):126–128, 2001.
- [54] Christoph J Brabec, Sean E Shaheen, Christoph Winder, N Serdar Sariciftci, and Patrick Denk. Effect of lif/metal electrodes on the performance of plastic solar cells. *Applied Physics Letters*, 80(7):1288–1290, 2002.
- [55] Byung-Ryool Hyun, Yu-Wu. Zhong, Adam C. Bartnik, Liangfeng Sun, Hector D. Abruña, Frank W. Wise, Jason D. Goodreau, James R. Matthews, Thomas M. Leslie, and Nicholas F. Borrelli. Electron injection from colloidal pbs quantum dots into titanium dioxide nanoparticles. *ACS Nano*, 2(11):2206–2212, 2008.
- [56] Illan J. Kramer, Larissa Levina, Ratan Debnath, David Zhitomirsky, and Edward H. Sargent. Solar cells using quantum funnels. *Nano Letters*, 11(9):3701–3706, 2011.
- [57] Matthew C Beard, Kelly P Knutsen, Pingrong Yu, Joseph M Luther, Qing Song, Wyatt K Metzger, Randy J Ellingson, and Arthur J Nozik. Multiple exciton generation in colloidal silicon nanocrystals. *Nano letters*, 7(8):2506–2512, 2007.

- [58] Victor S. Vavilov. On photo-ionization by fast electrons in germanium and silicon. *Journal of Physics and Chemistry of Solids*, 8(0):223 – 226, 1959.
- [59] C. Bostedt, T. van Buuren, T. M. Willey, N. Franco, L. J. Terminello, C. Heske, and T. Moller. Strong quantum-confinement effects in the conduction band of germanium nanocrystals. *Applied Physics Letters*, 84(20):4056–4058, 2004.
- [60] Marton Voros, Stefan Wippermann, Balint Somogyi, Adam Gali, Dario Rocca, Giulia Galli, and Gergely T. Zimanyi. Germanium nanoparticles with non-diamond core structures for solar energy conversion. *J. Mater. Chem. A*, pages –, 2014.
- [61] Elayaraja Muthuswamy, Andrew S. Iskandar, Marlene M. Amador, and Susan M. Kauzlarich. Facile synthesis of germanium nanoparticles with size control: Microwave versus conventional heating. *Chemistry of Materials*, 25(8):1416–1422, 2013.
- [62] J. P. Wilcoxon, P. P. Provencio, and G. A. Samara. Synthesis and optical properties of colloidal germanium nanocrystals. *Phys. Rev. B*, 64:035417, Jun 2001.
- [63] W.M. Haynes. *CRC Handbook of Chemistry and Physics, 93rd Edition*. CRC Handbook of Chemistry and Physics. Taylor & Francis, 2012.
- [64] Carena P Church, Elayaraja Muthuswamy, Guangmei Zhai, Susan M Kauzlarich, and Sue A Carter. Quantum dot ge/tio 2 heterojunction photoconductor fabrication and performance. *Applied Physics Letters*, 103(22):223506–223506, 2013.
- [65] S.A. Healy and M.A. Green. Efficiency enhancements in crystalline silicon solar

- cells by alloying with germanium. *Solar Energy Materials and Solar Cells*, 28(3):273–284, 1992.
- [66] Jurgen Michel, Jifeng Liu, and Lionel C Kimerling. High-performance ge-on-si photodetectors. *Nature Photonics*, 4(8):527–534, 2010.
- [67] M. C. Hanna and A. J. Nozik. Solar conversion efficiency of photovoltaic and photoelectrolysis cells with carrier multiplication absorbers. *Journal of Applied Physics*, 100(7):074510, 2006.
- [68] J. Shieh, H.L. Chen, T.S. Ko, H.C. Cheng, and T.C. Chu. Nanoparticle-assisted growth of porous germanium thin films. *Advanced Materials*, 16(13):1121–1124, 2004.
- [69] Zachary C Holman, Chin-Yi Liu, and Uwe R Kortshagen. Germanium and silicon nanocrystal thin-film field-effect transistors from solution. *Nano letters*, 10(7):2661–2666, 2010.
- [70] Ding-Jiang Xue, Jian-Jun Wang, Yong-Qing Wang, Sen Xin, Yu-Guo Guo, and Li-Jun Wan. Facile synthesis of germanium nanocrystals and their application in organic-inorganic hybrid photodetectors. *Adv Mater*, 23(32):3704–7, Aug 2011.
- [71] J. van der Heide, N. E. Posthuma, G. Flamand, and J. Poortmans. Development of low-cost thermophotovoltaic cells using germanium substrates. *AIP Conference Proceedings*, 890(1):129–138, 2007.
- [72] Daniel A. Ruddy, Justin C. Johnson, E. Ryan Smith, and Nathan R. Neale. Size

- and bandgap control in the solution-phase synthesis of near-infrared-emitting germanium nanocrystals. *ACS Nano*, 4(12):7459–7466, 2010.
- [73] Zachary C Holman and Uwe R Kortshagen. Nanocrystal inks without ligands: stable colloids of bare germanium nanocrystals. *Nano letters*, 11(5):2133–2136, 2011.
- [74] Zachary C Holman and Uwe R Kortshagen. Absolute absorption cross sections of ligand-free colloidal germanium nanocrystals. *Applied Physics Letters*, 100(13):133108–133108, 2012.
- [75] Daniel A. Ruddy, Peter T. Erslev, Susan E. Habas, Jason A. Seabold, and Nathan R. Neale. Surface chemistry exchange of alloyed germanium nanocrystals: A pathway toward conductive group iv nanocrystal films. *The Journal of Physical Chemistry Letters*, 4(3):416–421, 2013.
- [76] Simon M. Sze and Kwok K. Ng. *Physics of Semiconductor Devices*. WILEY-VCH Verlag, Hoboken, 3rd edition edition, 2006.
- [77] F. Berg Rasmussen, R. Jones, and S. Öberg. Nitrogen in germanium: Identification of the pair defect. *Phys. Rev. B*, 50:4378–4384, Aug 1994.
- [78] Chris G. Van de Walle and J. Neugebauer. Universal alignment of hydrogen levels in semiconductors, insulators and solutions. *Nature*, 423(6940):626–628, 06 2003.
- [79] Baoquan Sun, Guifu Zou, Xiaojuan Shen, and Xiaohong Zhang. Exciton dissociation

- tion and photovoltaic effect in germanium nanocrystals and poly(3-hexylthiophene) composites. *Applied Physics Letters*, 94(23):–, 2009.
- [80] S. Parola, E. Quesnel, V. Muffato, L. Xie, K. Leifer, J. Coignus, and A. Slaoui. Optoelectronic properties of p-i-n heterojunctions based on germanium nanocrystals. *Journal of Applied Physics*, 114(3):–, 2013.
- [81] Elayaraja Muthuswamy, Jing Zhao, Katayoun Tabatabaei, Marlene M. Amador, Michael A. Holmes, Frank E. Osterloh, and Susan M. Kauzlarich. Thiol-capped germanium nanocrystals: Preparation and evidence for quantum size effects. *Chemistry of Materials*, 26(6):2138–2146, 2014.
- [82] Ni Zhao, Tim P. Osedach, Liang-Yi Chang, Scott M. Geyer, Darcy Wanger, Madalena T. Binda, Alexi C. Arango, Mounsi G. Bawendi, and Vladimir Bulovic. Colloidal pbs quantum dot solar cells with high fill factor. *ACS Nano*, 4(7):3743–3752, 2010.
- [83] V. D. Mihailetschi, J. Wildeman, and P. W. M. Blom. Space-charge limited photocurrent. *Phys. Rev. Lett.*, 94:126602, Apr 2005.
- [84] Steven S. Hegedus and William N. Shafarman. Thin-film solar cells: device measurements and analysis. *Progress in Photovoltaics: Research and Applications*, 12(2-3):155–176, 2004.
- [85] J. E. Phillips, R. W. Birkmire, B. E. McCandless, P. V. Meyers, and W. N. Sha-

- farman. Polycrystalline heterojunction solar cells: A device perspective. *physica status solidi (b)*, 194(1):31–39, 1996.
- [86] Al L Efros, M Rosen, M Kuno, M Nirmal, DJ Norris, and M Bawendi. Band-edge exciton in quantum dots of semiconductors with a degenerate valence band: Dark and bright exciton states. *Physical Review B*, 54(7):4843, 1996.
- [87] Heng Yu, Jingbo Li, Richard A. Loomis, Lin-Wang Wang, and William E. Buhro. Two- versus three-dimensional quantum confinement in indium phosphide wires and dots. *Nat Mater*, 2(8):517–520, 08 2003.
- [88] Aurelien Du Pasquier, Daniel D. T. Mastrogiovanni, Lauren A. Klein, Tong Wang, and Eric Garfunkel. Photoinduced charge transfer between poly(3-hexylthiophene) and germanium nanowires. *Applied Physics Letters*, 91(18):–, 2007.
- [89] Chaoyi Yan, Nandan Singh, Hui Cai, Chee Lip Gan, and Pooi See Lee. Network-enhanced photoresponse time of ge nanowire photodetectors. *ACS Applied Materials Interfaces*, 2(7):1794–1797, 2010.
- [90] K. Szendrei, W. Gomulya, M. Yarema, W. Heiss, and M. A. Loi. Pbs nanocrystal solar cells with high efficiency and fill factor. *Applied Physics Letters*, 97(20):–, 2010.

List of Acronyms

μ	electron mobility.
Ag	Silver.
Al	Aluminum.
Au	Gold.
BDT	Benzenedithiol.
Ca	Calcium.
CB	Conduction Band.
CdS	Cadmium Sulfide.
CdSe	Cadmium Selenide.
CSM	Colorado School of the Mines.
Cu	Copper.

DI	Deionized Water.
EDT	Ethanedithiol.
EDX	Energy Dispersive Xray Spectroscopy.
EPR	Electron Paramagnetic Resonance.
EQE	External Quantum Efficiency.
ESR	Electron Spin Resonance.
FTIR	Fourier Transform Infrared Spectroscopy.
FTO	Flourine Tin Oxide.
GCA	Gradual Channel Approximation.
Ge	Germanium.
HOMO	Highest-Occupied Molecular Orbit.
I_d	Drain current.
IQE	Internal Quantum Efficiency.
ITO	Indium Tin Oxide.
J_{sc}	Short-Circuit Current.

JV	Current-Voltage.
LUMO	Lowest-Unoccupied Molecular Orbit.
Mg	Magnesium.
MPA	Mercaptopropionic Acid.
NP	Nanoparticle.
PbS	Lead Sulfide.
PbSe	Lead Selenide.
PL	Photoluminescence.
PV	Photovoltaic.
QD	Quantum Dots.
SEM	Scanning Electron Microscope.
Si	Silicon.
TEM	Transmission Electron Microscope.
TiO ₂	Titanium Dioxide.

TRPL Time-Resolved Photoluminescence.

UCD University of California, Davis.

UV-Vis-NIR Ultraviolet-Visible-Near Infrared.

V_g Gate Current.

V_{oc} Open-Circuit Voltage.

VB Valence Band.

V_{bi} Built-In Voltage.